Development of novel antimalarials
targeting the plasmodial lactate transporter (PfFNT)
through a fluorescence cross-correlation spectroscopy-based
approach and functional assay

Dissertation

zur Erlangung des Doktorgrades

der Mathematisch-Naturwissenschaftlichen Fakultät

der Christian-Albrechts-Universität zu Kiel

vorgelegt von

Iga Jakóbowska

Kiel, 2023

Erster Gutachter: Prof. Dr. Eric Beitz

Zweiter Gutachter: Dr. Stefan Hannus

Tag der mündlichen Prüfung: 11 July 2023

Table of Contents

Table of Contents

Abbreviations

ACF	Autocorrelation function		DMSO	Dimethyl sulfoxide
ACN	Acetonitrile		DNA	Deoxyribonucleic acid
ACT	Artemisinin-based combination therapy		DPBS	Dulbecco's Phosphate Buffered Saline
ADP	Adenosine 5′-diphosphate		DV	Digestive vacuole
Amp	Ampicillin		EC$_{50}$	Half maximal effective concentration
APD	Avalanche photodiode detector		ECL	Enhanced chemiluminescence
APS	Ammonium persulfate		EDTA	Ethylenediaminetetra-acetic acid
ATP	Adenosine 5′-triphosphate			
BCA	Bicinchoninic acid		eGFP	Enhanced green fluorescent protein
CHAPS	3-[(3-Cholamidopropyl)-dimethylammonio]-1-propanesulfonate		EtBr	Ethidium bromide
			FBS	Fetal bovine serum
CHS	Cholesteryl hemisuccinate		FCCS	Fluorescence cross-correlation spectroscopy
CLSM	Confocal laser scanning microscopy		FCS	Fluorescence correlation spectroscopy
CMC	Critical micellar concentration		FNT	Formate-nitrite transporter
CRISPR	Clustered regularly interspaced short palindromic repeats		GFP	Green fluorescent protein
DDM	n-Dodecyl-β-D-maltopyranoside		GLUT1	Glucose transporter 1
DDT	Dichlorodiphenyl-trichloroethane		HBSS	Hank's Balanced Salt Solution
dH$_2$O	Distilled H$_2$O		HEK293	Human embryonic kidney 293 cell line
DHFR	Dihydrofolate reductase		HEPES	4-(2-Hydroxyethyl)-1-piperazineethanesulfonic acid
DHPS	Dihydropteroate synthase			
DIEA/ DIPEA	N,N-Diisopropyl-ethylamine		HPLC	High-performance liquid chromatography
DM	n-Decyl β-maltoside		HRP	Horseradish peroxidase
DMEM	Dulbecco's Modified Eagle Medium		HT	Hexose transporter

Abbreviations

HTS	High-throughput screening		PfFNT	*Plasmodium falciparum* formate-nitrite transporter
IC_{50}	Half maximal inhibitory concentration		PfMDR1	*Plasmodium falciparum* multidrug resistance transporter 1
IRS	Indoor residual spraying		PfPI3K	*Plasmodium falciparum* phosphatidylinositol 3-kinase
ITN	Insecticide-treated mosquito net			
K_D	Dissociation constant		PIC	Protease inhibitor cocktail
K_i	Inhibition constant		PNK	Polynucleotide kinase
k_{obs}	Observed rate constant		PPM	Plasmodial plasma membrane
k_{off}	Dissociation rate constant			
k_{on}	Association rate constant		PVM	Plasmodial vacuolar membrane
LB	Lennox broth		RBCM	Red blood cell membrane
LDAO	Lauryldimethylamine oxide		ROS	Reactive oxygen species
LDH	Lactate dehydrogenase		RT	Room temperature
LMNG	Lauryl maltose neopentyl glycol		SDS	Sodium dodecyl sulfate
MCT	Monocarboxylate transporter		SE	Standard error
			TAE	Tris-acetate-EDTA
MMV	Medicines for Malaria Venture		TBS	Tris buffered saline
NAD	Nicotinamide adenine dinucleotide		TEMED	Tetramethylethylene-diamine
NTP	Nucleoside triphosphate		TFA	Trifluoroacetic acid
ORF	Open reading frame		Tris	Tris(hydroxymethyl)-aminomethane
PAGE	Polyacrylamide gel electrophoresis		Triton X-100	2-[4-(2,4,4-Trimethylpentan-2-yl)phenoxy]ethanol
PBS	Phosphate buffered saline			
PCR	Polymerase chain reaction		Tween-20	Polyoxyethylene (20) sorbitan monolaurate
PEG	Polyethylene glycol		WHO	World Health Organization
Pen Strep	Penicillin/Streptomycin		wt	Wild type
PfCRT	*Plasmodium falciparum* chloroquine resistance transporter			

Abstract

Drug resistance is a significant obstacle in the fight against malaria, prompting the exploration of new treatment approaches and drug targets. One potential target is the recently discovered plasmodial lactate transporter, PfFNT (short for *Plasmodium falciparum* formate-nitrite transporter). Several studies have shown that inhibiting this transporter can cause the accumulation of toxic levels of lactate within the parasite, leading to its death. Two compounds, BH296 and BH267.meta, have been developed to target both the PfFNT wild type (wt) and a relevant mutant, G107S. So far, these compounds have only been tested using a yeast-based functional assay, and biophysical characterization was missing. In this study, fluorescence cross-correlation spectroscopy (FCCS) measurements were performed to determine true K_i-values, as well as k_{on} and k_{off} rate constants for the binding of inhibitors to both the PfFNT wt and G107S mutant. BH296 and BH267.meta gave similar rate constants for binding to PfFNT wt. BH296 was inactive on PfFNT G107S, whereas BH267.meta bound to the mutant protein, albeit with weaker affinity than to PfFNT wt. Once the reliability of FCCS measurements had been confirmed, a compound library of 2,000 inhibitors was screened to identify novel scaffolds that have the potential to inhibit PfFNT. However, in the first round of FCCS screening, no candidate with an inhibitory effect greater than 30% was identified. FCCS only allows the search for new inhibitors that displace the existing inhibitor, i.e., share the same binding pocket. Confocal imaging confirmed that the current PfFNT inhibitors, bind to the intracellular side of the transporter. Targeting intracellular proteins is often challenging because molecules must first traverse the cell membrane to reach the cytosol. To identify an alternative binding site, a functional screening assay with AZD3965 and Metformin was developed in this thesis. Treatment of HEK293 cells expressing PfFNT with the monocarboxylate transporters inhibitor (AZD3965), the oxidative phosphorylation inhibitor (Metformin), and the specific PfFNT inhibitor (BH296) induced cell death as a consequence of NAD^+ depletion. However, in the absence of BH296, cells survived because lactate is transported outside the cell via the PfFNT channel, and NAD^+ required for glycolysis can still be regenerated. Based on this principle, the goal was to screen a library and score compounds that, similar to BH296, block the transport of lactate out of the cell, causing cell death. After testing the library of 22,000 compounds, 7 primary hits were identified that need to be further validated.

Zusammenfassung

Resistenzbildung gegen Medikamente ist ein erhebliches Hindernis im Kampf gegen Malaria, was die Erforschung neuer Behandlungsansätze und Angriffspunkte für Medikamente erforderlich macht. Ein potenzielles Ziel ist der kürzlich entdeckte plasmodiale Laktattransporter PfFNT (kurz für *Plasmodium falciparum* formate-nitrite transporter). Mehrere Studien haben gezeigt, dass die Inhibition dieses Transporters zu einer Akkumulation toxischer Laktatmengen im Parasiten führen kann, was dessen Tod zur Folge hat. Zwei Wirkstoffe, BH296 und BH267.meta, wurden entwickelt, um sowohl den PfFNT-Wildtyp als auch eine relevante Mutante, G107S, zu hemmen. Bisher wurden diese Verbindungen nur mit einem Hefe-basierten funktionellen Assay getestet, doch es fehlte eine biophysikalische Charakterisierung. In dieser Studie wurden Messungen der Fluoreszenz-Kreuzkorrelationsspektroskopie (FCCS) durchgeführt, um die tatsächlichen K_i-Werte sowie die K_{on}- und K_{off}-Ratenkonstanten für die Bindung der Inhibitoren an den PfFNT-Wildtyp und die G107S-Mutante zu bestimmen. BH296 und BH267.meta ergaben ähnliche Geschwindigkeitskonstanten für die Bindung an den PfFNT-Wildtyp. BH296 war auf PfFNT G107S inaktiv, während BH267.meta an das mutierte Protein band, wenn auch mit schwächerer Affinität als an PfFNT-Wildtyp. Nachdem die Zuverlässigkeit der FCCS-Messungen bestätigt worden war, wurde eine Substanzbibliothek mit 2,000 Inhibitoren gescreent, um neuartige Gerüstsubstanzen zu identifizieren, die das Potenzial haben, PfFNT zu hemmen. In der ersten Runde des FCCS-Screenings wurde jedoch kein Kandidat mit einer Hemmwirkung von mehr als 30% identifiziert. FCCS ermöglicht nur die Suche nach neuen Hemmstoffen, die den bestehenden Hemmstoff verdrängen, d. h. die gleiche Bindungstasche teilen. Die konfokale Bildgebung bestätigte, dass die aktuellen PfFNT-Inhibitoren BH296 und BH267.meta an die intrazelluläre Seite des Transporters binden. Um therapeutische Zielstrukturen zu binden, die auf der Membraninnenseite liegen, müssen Moleküle zunächst die Zellmembran durchqueren, was die Entwicklung eines geeigneten Wirkstoffs zusätzlich erschwert. Um eine alternative Bindungsstelle zu identifizieren, wurde in dieser Arbeit ein funktioneller Screeningtest mit AZD3965 und Metformin entwickelt. Die Behandlung von PfFNT exprimierenden HEK293-Zellen, mit dem Inhibitor des Monocarboxylat-Transporters (AZD3965), dem Inhibitor der oxidativen Phosphorylierung (Metformin) und dem spezifischen PfFNT-Inhibitor (BH296) führte zum Tod der Zellen, da die Fähigkeit der Zelle, NAD^+ zu recyceln, dann

vollständig verloren geht. In Abwesenheit von BH296 kam es jedoch nicht zum Zelltod, da Laktat über den PfFNT-Kanal aus der Zelle transportiert wird und das für die Glykolyse benötigte NAD^+ weiterhin regeneriert werden kann. Auf der Grundlage dieses Prinzips wurde eine Bibliothek gescreent, um Verbindungen zu finden, die ähnlich wie BH296 den Transport von Laktat aus der Zelle heraus blockieren und letztendlich den Zelltod verursachen. Nach dem Testen einer Bibliothek von 22,000 Verbindungen ergaben sich 7 Treffer, die weiter validiert werden müssen.

The translation of the abstract into German was kindly provided by Dr. Stefan Hannus.

1 Introduction

1.1 Malaria

Malaria is one of the most common infectious diseases and a major public health problem worldwide, especially in Africa and South Asia (WHO, 2021). Around three billion people in 85 countries are at risk of infection (Ansbro, 2020; WHO, 2021; Wilcke, 2018). Despite global efforts to eradicate the disease, malaria continues to affect roughly 250 million individuals every year, leading to approximately one million deaths (Ansbro, 2020; WHO, 2021). The causative agents of malaria are unicellular, eukaryotic parasites belonging to the genus *Plasmodium*, which are transmitted to humans through the bites of infected female *Anopheles* mosquitoes (Cox, 2010; Laveran, 1881; Ross, 1898).

1.1.1 Epidemiology

1.1.1.1 Areas at risk

Malaria is typically found in tropical and some subtropical regions of Africa, Central and South America, Asia, and Oceania (Figure 1.1), however, the intensity of transmission and risk of infection varies substantially among the malaria-endemic areas (Birnbaum, 2017; Bloland & Williams, 2002; WHO, 2021). Over 90 percent of clinical malaria infections and deaths occur in Sub-Saharan Africa (WHO, 2021).

Figure 1.1 Countries or areas at risk of malaria transmission in 2020 according to the World Health Organization (WHO).

Predisposing factors that contribute to the prevalence of malaria include stagnant water, high temperatures, high humidity, and rainfall, which create ideal conditions for

mosquito breeding (Ali, 2012; Jamieson & Toovey, 2008). In contrast, malaria tends to be less common in highlands (>1,500 m) and arid areas (<1,000 mm rainfall/year), where the climate is unfavorable for mosquito growth (Bloland & Williams, 2002). Moreover, temperatures below 18°C limit transmission because the time necessary for mosquito development rises as temperature drops (Birnbaum, 2017; Coluzzi, 1999; Sachs & Malaney, 2002; Snow et al., 2005). There are about 200 *Plasmodium* species, but only five are known to infect humans: *P. falciparum*, *P. vivax*, *P. ovale*, *P. malariae*, and *P. knowlesi* (Birnbaum, 2017; Dhangadamajhi et al., 2010; WHO, 2021). Among all malaria parasites, *Plasmodium falciparum* is the most dangerous because it has a tendency to progress into severe malaria (Ansbro, 2020; WHO, 2021). The particular virulence of *P. falciparum* is related to the cytoadhesion of infected erythrocytes to host microvasculature (Brazier et al., 2017; Costa et al., 2006; Smith et al., 2013). The various species have different geographical distributions; *P. falciparum* is predominant in Sub-Saharan Africa and South Asia, while *P. vivax* in America and the Western Pacific region (Birnbaum, 2017; Blancke-Soares, 2016; Hanssen et al., 2010; Howes et al., 2016; Price et al., 2007). The remaining three *Plasmodium* species contribute to the worldwide malaria burden to a lesser level. *P. ovale* and *P. malariae* are uncommon, whereas *P. knowlesi* is a zoonotic parasite (transmitted only from apes to humans and not between humans) (Birnbaum, 2017; Dankwa et al., 2016; Greenwood et al., 2008; Jonscher, 2018; Naranjo-Prado, 2020; Singh & Daneshvar, 2013).

1.1.1.2 Malaria transmission

Malaria was thought to be transmitted by bad air (Italian: *mala aria*) in areas of swamps and marshland until the causal agent was discovered (Capanna, 2006; Khosh-Naucke, 2018; Ullrich, 2016). In 1880, Charles Louis Alphonse Laveran recognized a parasitic protozoan in human red blood cells as the real source of malaria (Khosh-Naucke, 2018; Laveran, 1881). After more than a decade, malaria parasites of the genus *Plasmodium* were found to be spread by female *Anopheles* mosquitoes during a blood meal (Khosh-Naucke, 2018; Ross, 1898; Ullrich, 2016; Warrell & Gilles, 2002). Male *Anopheles* mosquitos do not transmit malaria parasites because they solely feed on nectar and other sugar sources (Ullrich, 2016). Females, on the other hand, require sugar for energy as well as blood proteins for egg formation (Lehane, 1991; Ullrich, 2016). The life cycle of *Anopheles* mosquitoes, just like other mosquito species, comprises four phases, namely the egg, larva, pupa, and imago stages (CDC, 2015). The duration of the first three stages,

which are aquatic, is dependent on both the species and the ambient temperature and can range from 7 to 14 days (CDC, 2015; Mala et al., 2016; Warrell & Gilles, 2002). In nature, the males' final adult phase lasts one week, while the females' final adult phase lasts two weeks (CDC, 2015; Ullrich, 2016). *Anopheles* mosquitoes are distinguishable from other genera by their distinctive posture, which is characterized by their bodies being angled at 30 to 45 degrees to the ground (Figure 1.2) (CDC, 2015; Ullrich, 2016).

Figure 1.2 Comparison of Anopheles (left) and Aedes (right) mosquitoes. The figure is reprinted from (Schroeder, 2016).

Although there are around 430 known *Anopheles* species, only 30-40 transmit malaria (i.e., are "vectors") in nature (Birnbaum, 2017; CDC, 2015; Mace et al., 2016). *Anopheles gambiae* is one of the most well-known because of its role in the transmission of *Plasmodium falciparum* (Birnbaum, 2017; Mendes et al., 2008; Sinka et al., 2011). Malaria-transmitting mosquitoes can be found not just in malaria-endemic areas, but even in locations where the disease has been eradicated. As a result, these places are in danger of disease reintroduction (CDC, 2015).

1.1.2 Life cycle of the malaria parasite

The eukaryotic *Plasmodium* parasite has a complicated life cycle that includes developmental stages in both, the vertebrate (human) host and the female *Anopheles* mosquito (Figure 1.3) (Fujioka & Aikawa, 2002; Wilcke, 2018). The life cycle of the *Plasmodium* parasite begins when a female *Anopheles* mosquito injects saliva, containing the sporozoites (infectious, highly motile forms of the malaria parasite), into the humans' bloodstream (Ansbro, 2020; Cox, 2010; Phillips et al., 2017; Smit, 2014; Wilcke, 2018). The human immune system blocks some sporozoites, but the majority of them migrate to the liver and invade hepatocytes (Smit, 2014). This stage is often referred to as the pre-erythrocytic or exo-erythrocytic stage (Ansbro, 2020; Plebanski & Hill, 2000; Shortt & Garnham, 1948; Smit, 2014). In the liver, the sporozoites multiply asexually and grow to create a schizont (a multinucleated asexual form resulting from protozoan reproduction)

(Smit, 2014). The schizont splits into several tiny cells called merozoites, which are released into the bloodstream where they rapidly invade the red blood cells (erythrocytic stage) (Ansbro, 2020; Smit, 2014; Ullrich, 2016). *P. vivax* and *P. ovale* have a stage of dormancy known as hypnozoites, which can persist in the liver for a prolonged period before transforming into schizonts (Birnbaum, 2017; Blancke-Soares, 2016; Smit, 2014). This is frequently associated with the reoccurrence of malaria, sometimes many years after the initial infection (Fujioka & Aikawa, 2002; Krettli & Miller, 2001; Smit, 2014).
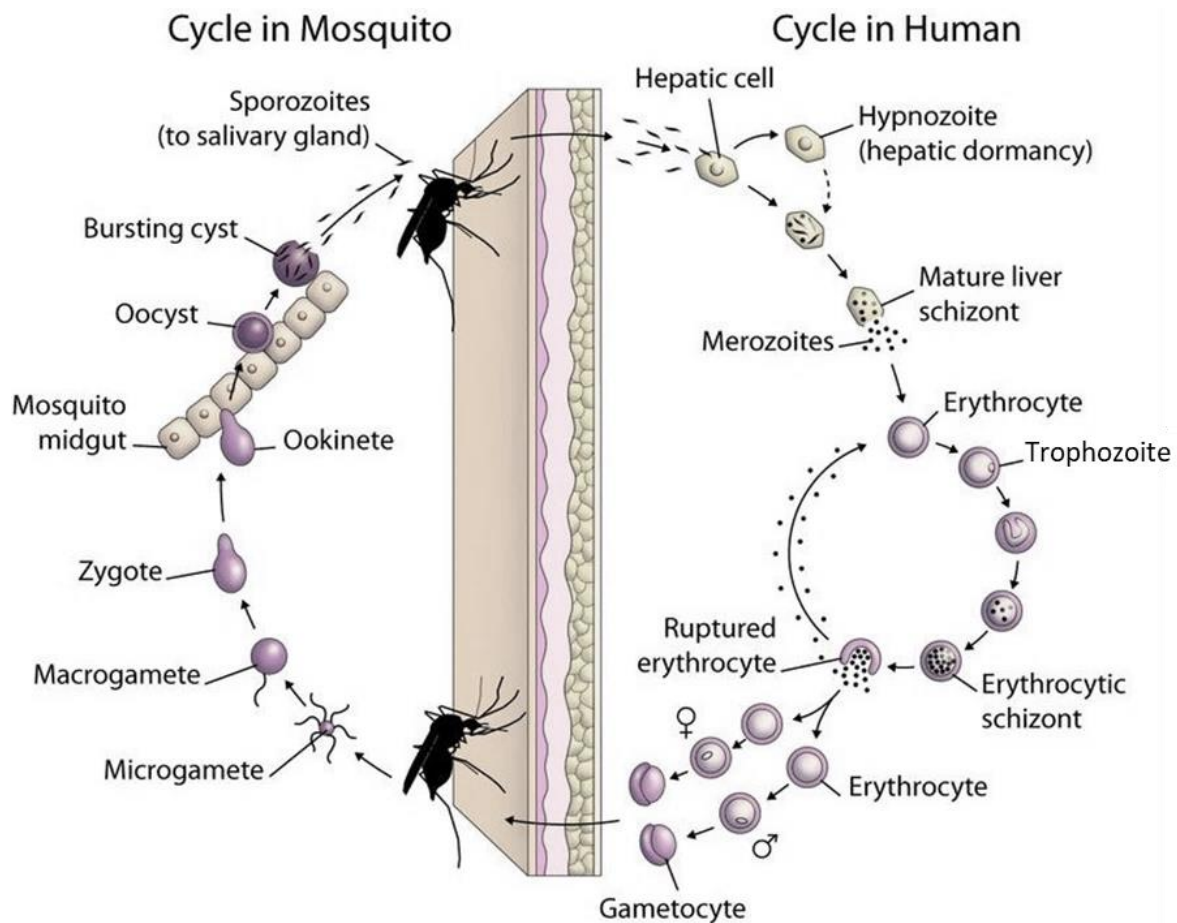
Figure 1.3 Malaria parasite life cycle. The figure is reprinted from (BSPH, n.d.).

Within the red blood cells, the ring stage trophozoites (activated, feeding stage in the life cycle of protozoa) mature into schizonts, which rupture releasing thousands of merozoites that might infect other erythrocytes and cause clinical symptoms (Ashley & White, 2014; CDC, 2015). Some of the infected blood cells leave the cycle of asexual multiplication (Ouattara & Laurens, 2015). Instead of replicating, merozoites start to differentiate into male and female gametocytes (micro-and macrogametes, respectively), indicating the beginning of the sporogonic (sexual) stage (Ansbro, 2020; Wilcke, 2018). When a mosquito bites an infected person, the male and female gametocytes are ingested,

and they fuse in the mosquito midgut to form the zygote (Ansbro, 2020; Ouattara & Laurens, 2015). The zygote transforms into a motile ookinete after which it develops into the so-called oocyst (Jonscher, 2018). Nine to twelve days later, the oocyst eventually bursts, releasing thousands of sporozoites that travel to the mosquito's salivary glands (Ansbro, 2020; CDC, 2015; Ouattara & Laurens, 2015; Smit, 2014). When a mosquito feeds on the blood of a susceptible vertebrate host, the life cycle starts all over again (Bray & Garnham, 1982; Fujioka & Aikawa, 2002; Smit, 2014; Ullrich, 2016).

1.1.3 Clinical manifestation

Plasmodium spp. infection severity varies widely depending on the species and a variety of host characteristics, such as hereditary resistance factors, age, prior exposure, and immune levels (Ansbro, 2020; Bruce-Chwatt, 1985; Miller et al., 2002; Ullrich, 2016). Typically, the symptoms of uncomplicated malaria include headache, acute fever, muscle pain, fatigue, sweating, nausea, and vomiting (Figure 1.4) (Ansbro, 2020; Birnbaum, 2017; Bruce-Chwatt, 1985; Oakley et al., 2011; Smit, 2014).
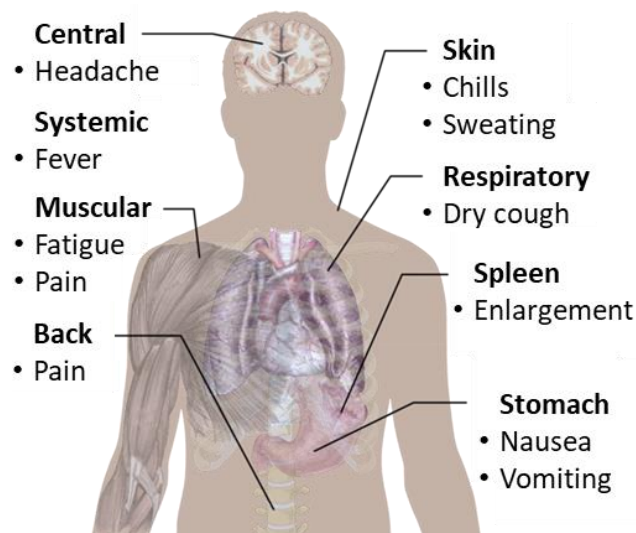
Figure 1.4 Common symptoms and organs affected by malaria. The figure is reprinted from (Fairhurst & Wellems, 2010).

All symptoms of a malaria infection originate from the blood stage of the parasite life cycle, which involves the release of newly formed parasites from erythrocytes (Bartoloni & Zammarchi, 2012; Buffet et al., 2011; Wilcke, 2018). Aside from moderate irritation at the mosquito bite site, there are no clinical symptoms that occur during the exoerythrocytic stage (liver stage), sexual stage (gametocytogenesis), or when sporozoites enter the host bloodstream (Ansbro, 2020; Cowman & Crabb, 2006). The duration of the asymptomatic liver stage and the replication rate in the subsequent

symptomatic blood phase determine the malaria incubation time. In *P. falciparum* the onset of symptoms starts 9-14 days after infection. *P. vivax* and *P. ovale* have a slightly later onset at days 12-18, while the incubation period for *P. malariae* is 18-40 days (Ashley & White, 2014; Birnbaum, 2017). The characteristic reoccurring fevers seen in malaria infections correlate to the *Plasmodium* species' intra-erythrocytic life cycle and are the body's reaction to the bursting of contaminated erythrocytes (Birnbaum, 2017; Bruce-Chwatt, 1985). The intra-erythrocytic life cycle of *P. falciparum*, *P. vivax,* and *P. ovale* infections is 48 hours, which translates to fevers every third day (tertian) (Ansbro, 2020). *P. malariae* has a 72-hour life cycle with fevers every fourth day (quartan), whereas *P. knowlesi* has a 24-hour life cycle with daily fevers (quotidian) (Ansbro, 2020; Bartoloni & Zammarchi, 2012; Birnbaum, 2017; Sharma & Khanduri, 2009). If malaria symptoms are left untreated, especially with *P. falciparum* infection, it can result in severe complications, such as acute anemia, metabolic acidosis, multi-organ failure, hypoglycemia, respiratory distress, coma, cerebral malaria, and eventually death (Greenwood et al., 2008; Jonscher, 2018; Miller et al., 2013; Smit, 2014; Ullrich, 2016). Even though there is evidence of severe *P. vivax* infections, *P. vivax*, *P. ovale*, *P. malariae,* and *P. knowlesi* infections seldom have life-threatening effects on the patient (Birnbaum, 2017; WHO, 2021). In contrast, severe malaria occurs in about 1% of *P. falciparum* malaria infections, with 90% of these cases occurring in children in Sub-Saharan Africa (Blancke-Soares, 2016; Rahimi et al., 2014).

1.1.4 Prevention and treatment

Methods for reducing disease transmission or protecting people in malaria-endemic areas include prophylactic drugs, vaccination, mosquito eradication, and the prevention of mosquito bites.

1.1.4.1 Vector control

In the past, the use of the insecticide DDT (dichlorodiphenyltrichloroethane) was the most effective vector control method in terms of malaria eradication, particularly between 1943 and 1972 (Berry-Cabán, 2011; Blancke-Soares, 2016). Its usage lowered the population at risk of malaria from 77% in 1900 to around 50% in 1975 (Ansbro, 2020; Birnbaum, 2017; Blancke-Soares, 2016; Enayati & Hemingway, 2010). However, the use of DDT was reduced in the 1970s because of arising health issues of exposed people and mosquito resistance (Beard, 2006; Blancke-Soares, 2016; Ullrich, 2016). In humans, the

harmful consequences of direct DDT exposure include developmental defects, reproductive illness, neurological disease, and cancer (Kabasenche & Skinner, 2014). Currently, the most effective vector control techniques are the use of insecticide-treated mosquito nets (ITNs) and indoor residual spraying (IRS) (Binka & Akweongo, 2006; Ullrich, 2016; WHO, 2021). Nevertheless, because of the usage of insecticides, these methods are also susceptible to mosquito resistance (Blancke-Soares, 2016; Turusov et al., 2002). New genetic techniques such as CRISPR/Cas and gene drive technology enable fresh approaches to develop infertile mosquitos that can disrupt mosquito populations after release, or mosquitos that cannot be infected by *Plasmodium* parasites, hence breaking transmission (Blancke-Soares, 2016; Eckhoff et al., 2017; Gantz et al., 2015; Hammond et al., 2016; Jonscher, 2018). The impact of introducing these genetically modified organisms into the ecosystem is, however, a topic of debate in both the scientific and public sectors (Jonscher, 2018; Pennisi, 2015).

1.1.4.2 Antimalarials and drug resistance

Depending on the parasite type and the severity of the sickness, people with malaria can be treated with a variety of medications, see Table 1.1 (Ullrich, 2016). There are many types of antimalarials available on the market which can be classified into four groups according to their chemical structure and mechanism of action: quinine and its derivates, such as chloroquine, mefloquine and lumefantrine; antifolates such as proguanil and pyrimethamine; atovaquone; artemisinin and its derivates, for instance, artesunate and artemether (Arrow et al., 2004; Birnbaum, 2017; Na-Bangchang & Karbwang, 2019; Tse et al., 2019). The first antimalarial compound, quinine, was already discovered in the 17th century (Blancke-Soares, 2016; Foley & Tilley, 1998; Miller et al., 2013). It is believed that British colonialists drank quinine-containing Tonic Water to avoid malaria infections (Ullrich, 2016). To mask its bitter taste, they blended it with gin and created the Gin Tonic (Meyer et al., 2004; Ullrich, 2016). Since 1820 quinine was extracted from the bark of the *Cinchona* tree and subsequently used as the standard treatment for malaria (Achan et al., 2011; Arrow et al., 2004; Blancke-Soares, 2016; Butler et al., 2010; Foley & Tilley, 1998). However, the side effects of quinine are significant and can occur at therapeutic doses or in cases of overdose, including blurred vision, disorientation, skin rashes, tinnitus, vertigo, cardiotoxicity, and nausea (Achan et al., 2011; Ansbro, 2020). In 1934, efforts to produce synthetic quinine resulted in the development of the more affordable, safe and efficient drug chloroquine (Coatney, 1963; Slater, 1993; Trape, 2001). The mechanism of

chloroquine action is so far only partially understood, however, it is believed that the drug (a weak base) is able to diffuse into the acidic (approximately 5.3) digestive vacuole (DV) of the parasite, where it becomes protonated and subsequently trapped within the DV. The digestive vacuole is involved in the enzymatic digestion of the host hemoglobin. During this process, hemoglobin is degraded into amino acids and heme (ferriprotoporphyrin IX), a toxic byproduct that must be converted into hemozoin (Rosenthal, 2005; Wilcke, 2018). Chloroquine is thought to inhibit the polymerization of hemozoin, causing the accumulation of toxic heme, and ultimately the death of the parasite (Birnbaum, 2017; Blasco et al., 2017; Greenwood et al., 2008; Homewood et al., 1972; Jonscher, 2018; Yayon et al., 1984). The parasite most frequently develops resistance to chloroquine-containing antimalarial drugs by simply expelling it from the digestive vacuole, through different point mutations (i.a. K76T) in the gene that encodes the essential DV transporter PfCRT (Birnbaum, 2017; Durand et al., 2001; Fidock et al., 2000; Sidhu et al., 2002; Wellems & Plowe, 2001). In addition, mutations in the multidrug-resistant transporter, PfMDR1, have also been linked to a reduced sensitivity to chloroquine (Ansbro, 2020; Duraisingh & Cowman, 2005; Schlitzer, 2007). Antifolate drugs, including proguanil and pyrimethamine, represent a different class of antimalarials. These drugs hamper folic acid synthesis by inhibiting the parasite's enzymes; dihydrofolate reductase-thymidylate synthase (DHFR) and dihydropteroate synthase (DHPS) (Birnbaum, 2017; Gregson & Plowe, 2005). The parasite relies on the synthesis of folates since they are essential cofactors in amino acid and nucleic acid metabolism (Birnbaum, 2017). Resistance to folate inhibitors is conferred by mutations in the targeted enzyme (Antony & Parija, 2016; Delves et al., 2012; Nzila, 2006). Another antimalarial drug in use is atovaquone, which interferes with the parasite's mitochondrial electron transport chain, leading to the inhibition of cellular respiration (Birnbaum, 2017; Fry & Pudney, 1992). Atovaquone resistance is accomplished by single-point mutations in the gene encoding *cytochrome b* (Antony & Parija, 2016; Birnbaum, 2017). In 1972, the next antimalarial drug artemisinin was isolated from the leaves, stems, and flowers of the *Artemisia annua* (Tu, 2011; Ullrich, 2016). Artemisinin is a fast-acting killing agent with a very short plasma half-life, which decreases the chance of parasite resistance (Ullrich, 2016; White, 2004). Several artemisinin derivatives were synthesized (e.g., artesunate, artemether), and they have replaced artemisinin due to their improved stability and higher efficacy (Birnbaum, 2017). In comparison to quinine, artemisinins

exhibit a high degree of tolerance and minimal side effects (Ansbro, 2020; White, 2008). These compounds are active against asexual erythrocytic stage parasites as well as sexual gametocytes (Adjalley et al., 2011; Skinner et al., 1996), but they have no effect on liver stages (Ansbro, 2020; Meister et al., 2011). The mode of action of artemisinins remains unknown (Birnbaum, 2017; Smit, 2014). Some models suggest that artemisinin and its derivatives become activated in the erythrocyte due to the reductive scission of their endoperoxide bridge by heme (Birnbaum, 2017; Meshnick, 2002; Wang et al., 2015). The activated form of artemisinins generates toxic free radicals or reactive oxygen species (ROS) in the parasite's cytoplasm, resulting in the alkylation of biomolecules (Ansbro, 2020). Consequently, parasite death occurs as a result of oxidative stress and cellular damage (Ansbro, 2020; Cui & Su, 2009; Meshnick, 2002; Straimer et al., 2015; Tilley et al., 2016). There are also other hypotheses regarding the mode of action; one claims that artemisinins inhibit PfATP6 (Eckstein-Ludwig et al., 2003), while another states that the drugs directly inhibit the *Plasmodium* phosphatidylinositol-3-kinase (PfPI3K) (Mbengue et al., 2015; Vaid et al., 2010). The molecular basis of resistance to artemisinins is also unclear. Several molecular markers for resistant strains have been identified of which a C589Y-mutation in the PfKelch13 gene is the most prominent, however, the function of this protein is still unknown (Ariey et al., 2014; Birnbaum, 2017; Jonscher, 2018; Mbengue et al., 2015; Mesén-Ramírez, 2016; Siddiqui et al., 2020). Artemisinin derivates have a fast therapeutic effect and are the most potent malarial drugs available, but they are also quickly removed from circulation, having a half-life of around 1 hour (Ansbro, 2020; Birnbaum, 2017; de Vries & Dien, 1996). The short half-lives of artemisinins are considered to be a significant factor in the occurrence of recrudescences (Ansbro, 2020; Cui & Su, 2009). Recrudescence is the term used to describe the reappearance of a malaria infection at a detectable level after it has remained at an undetectable level (Ansbro, 2020). That is why, artemisinin-based combination therapies (ACTs), which combine a derivate of artemisinin with a slower-acting medication with a longer serum half-life, such as lumefantrine or mefloquine, are currently the first-line therapy for malaria, according to the WHO recommendations (WHO, 2021). The fundamental principle of ACTs involves using the potent artemisinin-based compound to eliminate the majority of parasites within the first few days of treatment, followed by the partner drug, which has a different mode of action and a longer half-life, to clear any remaining parasites (Ansbro, 2020; Eastman & Fidock, 2009; Frey et al., 2010). Nevertheless, due to the overuse of

antimalarial drugs for prophylaxis, inadequate or incomplete treatments of active infections as well as a high level of parasite adaptability at the genetic and metabolic levels, malaria parasites have developed resistance to all currently available drugs, including ACTs (Ansbro, 2020; Hyde, 2007; Naranjo-Prado, 2020; WHO, 2021).

Table 1.1 Antimalarial drugs, targets, mode of action and reported resistances. This table is created based on (Makoah & Pradel, 2013).

Drug	Treatment recommendation	Toxicity grading	Target	Mode of action	Genes involved in resistance
Quinine	Severe malaria	+ + +	Blood stage	Inhibits heme detoxification	*pfnhe*
Chloroquine	*P. vivax* malaria	+	Blood stage	Inhibits heme detoxification	*pfcrt, pfmdr1*
Mefloquine	Uncomplicated malaria, as ACT	+ +	Blood stage	Inhibits heme detoxification	*pfmdr1*
Lumefantrine	Uncomplicated malaria, as ACT in combination with Artemether	+	Blood stage	Inhibits heme detoxification	*pfmdr1*
Antifolates (Proguanil, Pyrimethamine)	Uncomplicated malaria, as ACT	+	Blood stage	Inhibits folate metabolism	*pfdhps, pfdhfr*
Atovaquone	Uncomplicated malaria, as ACT in combination with Proguanil	+	Blood and liver stage	Inhibits mitochondrial electron transport	*cytochrome b*
Artemisinin derivatives (Artesunate, Artemether)	Main component of ACTs, Artesunate – sevre malaria	+	Blood stage and gametocytes	Unclear	*pfkelch13/ pfatpase6*

1.1.4.3 Vaccination

The use of vaccinations is an important control method against infectious illnesses, however, the development of a malaria vaccine has proven to be a challenging task (Birnbaum, 2017). This is related to the parasite's capability to evade the immune system, genetic polymorphisms, antigenic diversity, the parasite's intracellular living style, and its complicated life cycle (Birnbaum, 2017; Crompton et al., 2010; Jonscher, 2018; Sutherland, 2007; Wykes, 2013). On 6 October 2021, the first malaria vaccine, RTS,S/AS01 (also known as Mosquirix®), was approved by the WHO for the prevention of *P. falciparum* malaria in children living in moderate to high transmission areas (Ansbro, 2020; WHO, 2021). The vaccine was developed in the late 1980s by GlaxoSmithKline researchers in collaboration with the Walter Reed Army Institute of Research (WRAIR) (Ansbro, 2020; Laurens, 2020). RTS,S/AS01 is considered as a pre-

erythrocytic vaccine because it targets the circumsporozoite protein (CSP) on the sporozoite surface and *P. falciparum* parasites before they invade liver cells (Birnbaum, 2017; Laurens, 2020; Nadeem et al., 2022). The vaccine, however, is only moderately effective; in a pilot implementation involving more than 800,000 children in Kenya, Malawi, and Ghana, it had an efficacy of just 50% in preventing severe malaria in the first year, and its effectiveness declined substantially over time (Miller, 2022; Piore, 2022). Although this is a significant step forward in malaria vaccine research, Mosquirix® has limited effectiveness, and further work is needed to improve the efficacy and duration of protection (Alonso & O'Brien, 2022; Wilcke, 2018).

1.2 PfFNT as a novel antimalarial drug target

The development of resistance to all currently available antimalarials has prompted a need for new drugs, particularly those with new mechanisms of action (Ansbro, 2020; Hapuarachchi et al., 2017; Rottmann et al., 2010; Wells et al., 2015). The recently discovered plasmodial lactate transporter, PfFNT (abbreviation for *Plasmodium falciparum* formate-nitrite transporter), represents a promising new drug target due to its housekeeping role in lactate efflux during the intra-erythrocytic stage (Holm-Bertelsen et al., 2016; Marchetti et al., 2015; Peng et al., 2021; Wu et al., 2015). Malaria parasites rely entirely on anaerobic glycolysis to meet their energy demands (Figure 1.5) (MacRae et al., 2013; McKee et al., 1946). *Plasmodium* spp. infected erythrocytes consume glucose up to two orders of magnitude faster than uninfected red blood cells, resulting in the production of lactic acid as an anaerobic end product (McKee et al., 1946; Mehta et al., 2005; Rambow, 2015; Wu et al., 2015). Overall, plasmodia generate 2 moles each of ATP, lactate, and protons for every mole of glucose (Wu et al., 2015). Both glucose influx and lactate efflux are required to maintain intracellular homeostasis, and disruption of either biochemical pathway has been proposed as a new mode of action against malaria parasites (Joët et al., 2003; Lyu et al., 2021; Marchetti et al., 2015; Woodrow et al., 1999; Wu et al., 2015). PfFNT, a membrane protein from the formate/nitrite transporter (FNT) family, is responsible for transporting lactate, a metabolic waste product, from inside the parasite to the surrounding extracellular space (Hapuarachchi et al., 2017; Lyu et al., 2021; Marchetti et al., 2015; Wu et al., 2015). Lactate, if not swiftly released, will lead to cell death by acidification of the parasite's cytosol and breakdown of energy metabolism (Elliott et al., 2001; Marchetti et al., 2015; Rambow, 2015; Wu et al., 2015). The formate-nitrite transporters are widely distributed among pathogenic bacteria and eukaryotic

parasites, but they lack human homologs, making them appealing therapeutic targets (Atkovska & Hub, 2017). Their role is to transport small negatively charged molecules such as formate, acetate, and L-lactate as well as nitrite, hydrosulfide, and bicarbonate across biological membranes (Atkovska & Hub, 2017; Lü et al., 2013). The FNTs are distinct in terms of sequence, structure, and mechanism, from the monocarboxylate transporter family (MCT), which is responsible for the lactate export from human cells (Bader & Beitz, 2020; Golldack et al., 2017; Hapuarachchi et al., 2017; Jakobowska et al., 2021; Poole & Halestrap, 1994).
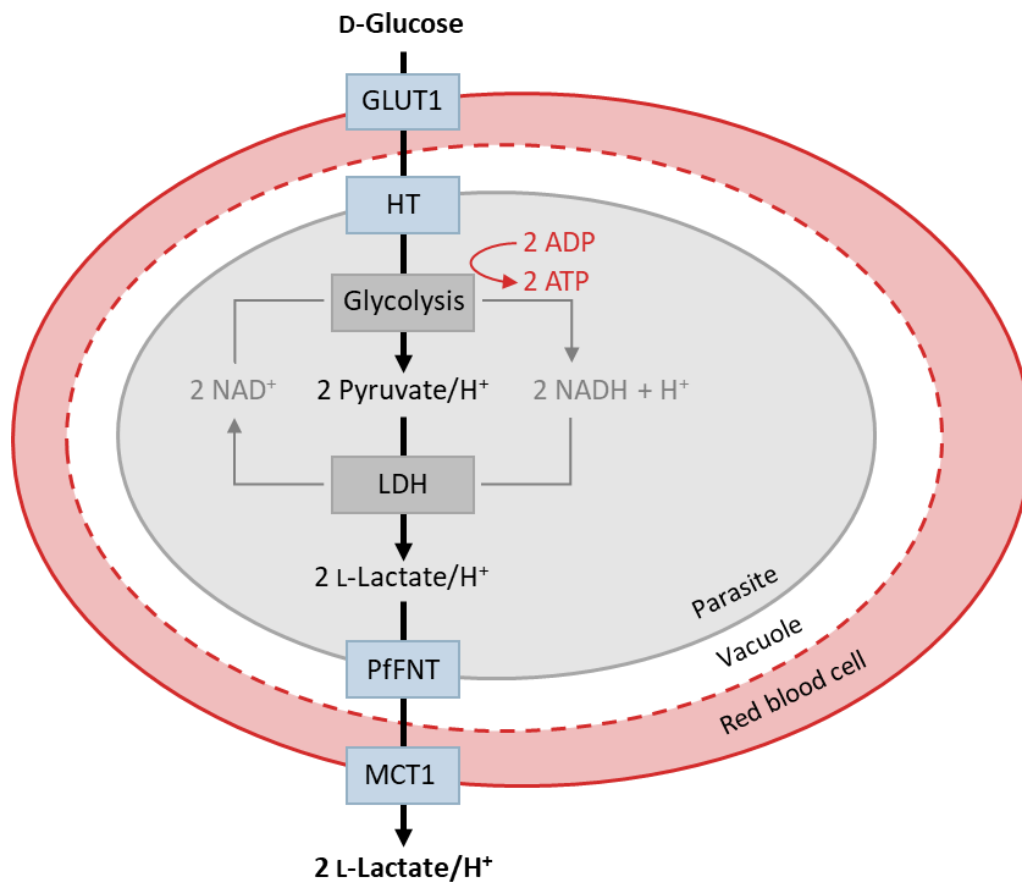
Figure 1.5 Energy flux in malarial parasites. The cytoplasm of the parasite is protected by three membranes: the red blood cell membrane (RBCM) (red line), the plasmodial vacuolar membrane (PVM) (red dotted line), and the plasmodial plasma membrane (PPM) (grey line) (Golldack et al., 2017; Spielmann et al., 2012). D-glucose uptake from the host serum is facilitated by the erythrocyte's glucose transporter, GLUT1 (Kasahara & Hinkle, 1977), followed by the rapid diffusion via hexose transporter, HT (Ortiz et al., 2015; Woodrow et al., 1999; Wu et al., 2015). The plasmodial vacuolar membrane is either fenestrated or has low-selectivity, high-capacity channels and it is freely permeable to low molecular-weight solutes (Desai et al., 1993; Rambow, 2015). Glucose is oxidized to pyruvate during glycolysis, which results in the formation of high-energy molecules adenosine triphosphate (ATP). Subsequently, lactate dehydrogenase (LDH) catalyzes the reduction of pyruvate to lactate (Wu et al., 2015). This large amount of L-lactate must be removed from the parasite due to the increasing osmotic stress and the decreasing pH value (Elliott et al., 2001; Marchetti et al., 2015). Lactate and protons are released via PfFNT, and finally, via the human monocarboxylate transporter MCT1 (Golldack et al., 2017).

1.2.1 Transport mechanism of PfFNT

The representatives of the FNT family form pentamers with a central, lipid-filled pore, however, each protomer functions as a separate transport unit (Figure 1.6) (Hajek et al., 2019; Lyu et al., 2021; Wang et al., 2009). The protomer fold is made up of six transmembrane helices around a symmetrical narrow transport path (Lyu et al., 2021; Nerlich et al., 2021; Peng et al., 2021). Both the N- and C-termini of PfFNT are found on the cytoplasmic side (Czyzewski & Wang, 2012; Waight et al., 2010).

PfFNT homopentamer
Top view
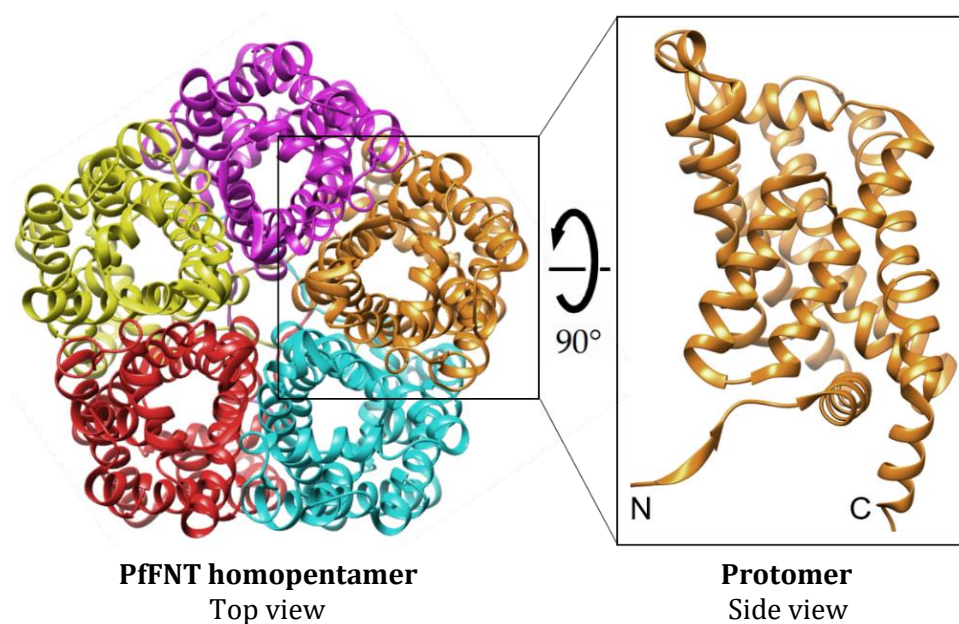
Protomer
Side view

Figure 1.6 PfFNT protein structure. Structure model of pentameric PfFNT (PDB# 7e26) seen from the extracellular side of the parasite (left) and cartoon representation of a PfFNT protomer (right) (Lyu et al., 2021; Nerlich et al., 2021). The figure is reprinted from (Nerlich et al., 2021).

The central channel of each PfFNT protomer contains two lipophilic constriction sites that sandwich a highly conserved neutral histidine residue (Figure 1.7) (Helmstetter et al., 2019; Lyu et al., 2021; Schmidt & Beitz, 2022; Wiechert & Beitz, 2017a, 2017b). The constriction sites are formed by bulky hydrophobic amino acid side chains that are extremely flexible (Lü et al., 2011; Schmidt & Beitz, 2022). These chains can swiftly reorganize themselves to contract and relax the channel, allowing substrate molecules to pass through the plasma membrane (Lü et al., 2011; Lyu et al., 2021; Schmidt & Beitz, 2022). Formate-nitrite transporters function bidirectionally in accordance with the *dielectric slide* mechanism (Figure 1.7) (Helmstetter et al., 2019; Peng et al., 2021; Schmidt & Beitz, 2022; Wiechert & Beitz, 2017a, 2017b). At both ends of the PfFNT transduction pathway, positively charged lysine residues electrostatically attract lactate anions into funnel-like vestibules (Helmstetter et al., 2019; Schmidt & Beitz, 2022;

Wiechert & Beitz, 2017b). As the pK$_a$ of lactic acid is 3.86, it should exist as a lactate anion in the cytoplasm of *P. falciparum*, where the cytoplasmic pH is roughly 7.15 (Kuhn et al., 2007; Lyu et al., 2021; Rambow, 2015). When a weak acid anion enters one of the vestibules, it is exposed to an increasingly lipophilic environment (Helmstetter et al., 2019; Schmidt & Beitz, 2022). This causes a decrease in its acid strength, which ultimately leads to protonation via the bulk water and the formation of neutral lactic acid (Helmstetter et al., 2019; Schmidt & Beitz, 2022; Wiechert & Beitz, 2017a). The neutralized substrate can then easily pass through the lipophilic constriction sites and neutral central histidine region and will eventually dissociate into the anion and proton after leaving the transporter (Helmstetter et al., 2019; Schmidt & Beitz, 2022; Wiechert & Beitz, 2017a).
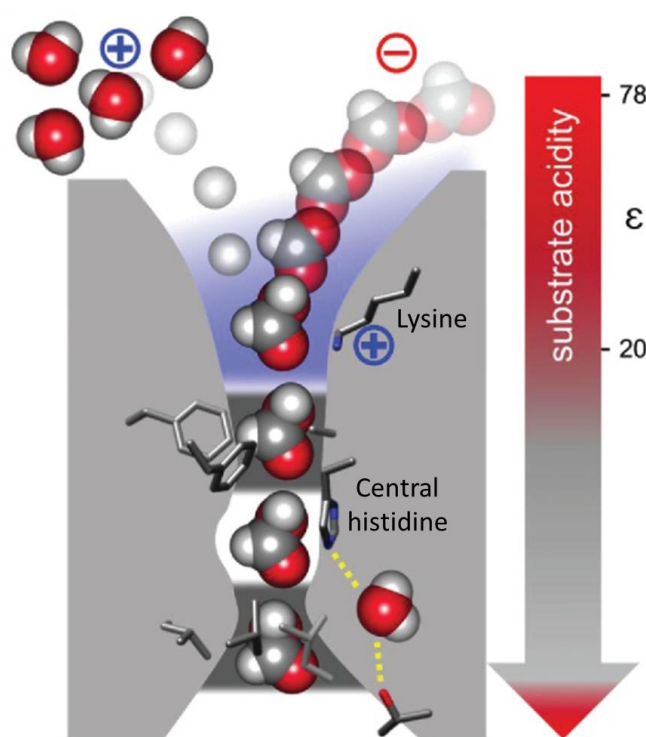
Figure 1.7 Schematic representation of the dielectric slide transport mechanism of FNTs according to (Wiechert & Beitz, 2017a). The substrate anion is electrostatically attracted by the positive charge of the conserved lysine (blue shading) and slides into a hydrophobic vestibule (Helmstetter et al., 2019; Schmidt & Beitz, 2022; Wiechert & Beitz, 2017a). Substrate acidity decreases simultaneously with the lowering dielectricity, ε, facilitating proton transfer from the bulk water (Wiechert & Beitz, 2017a). Once the substrate becomes neutral, it can easily pass through two lipophilic constriction sites (dark gray) (Helmstetter et al., 2019; Schmidt & Beitz, 2022; Wiechert & Beitz, 2017a). The figure is reprinted from (Wiechert & Beitz, 2017a).

1.2.2 Development of a PfFNT inhibitor

Phloretin, furosemide, and cinnamic acid derivatives were known inhibitors of the plasmodial lactate transport even before the discovery of PfFNT (Cranmer et al., 1995;

Elliott et al., 2001). However, their affinity and selectivity are insufficient for therapeutic application (Kanaani & Ginsburg, 1992). Screening of the Malaria Box, collected by the Medicines for Malaria Venture (MMV), led to the discovery of a specific and potent FNT-inhibitor, MMV007839, which kills cultured *P. falciparum* parasites at nanomolar concentrations (Figure 1.8A) (Golldack et al., 2017; Hapuarachchi et al., 2017; Nerlich et al., 2021; Spangenberg et al., 2013). The Malaria Box is a chemical library consisting of 400 drug-like compounds (Nerlich et al., 2021). These compounds were obtained from phenotypic screenings of *P. falciparum* parasite cultures, and effectively target unknown receptors with an $EC_{50} < 4$ µM (Nerlich et al., 2021).
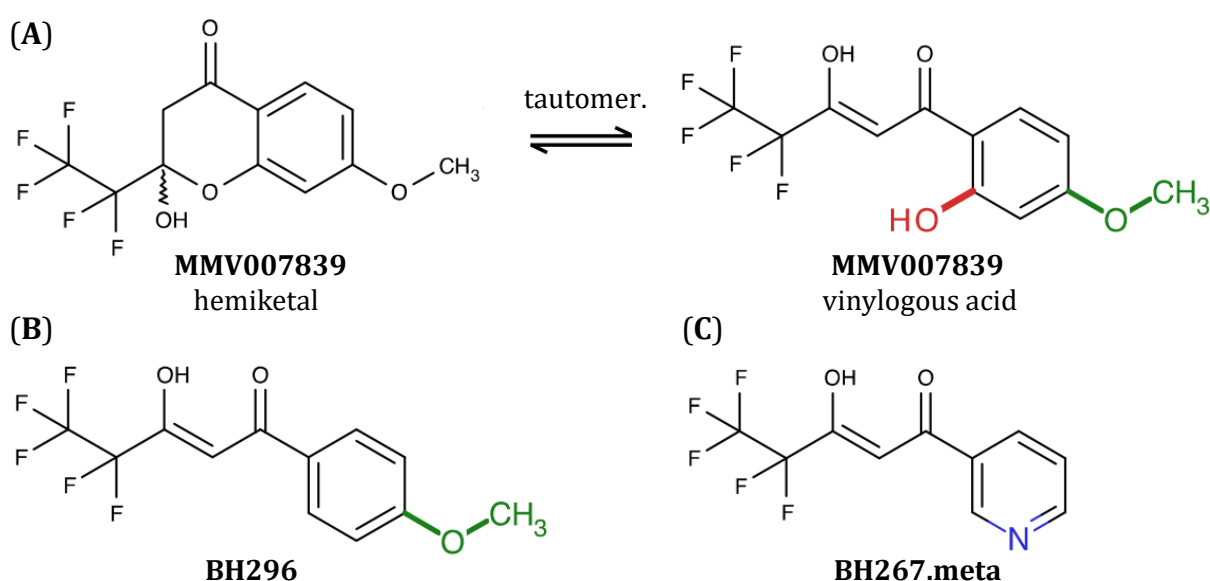
Figure 1.8 Selected PfFNT inhibitors. (**A**) MMV007839 exists in two tautomeric forms: a neutral hemiketal and a vinylogous acid that deprotonates to an anion (Jakobowska et al., 2021; Spangenberg et al., 2013). The active inhibitor form is the vinylogous acid tautomer, as demonstrated by BH296 (**B**), a molecule that is incapable of forming the cyclic hemiketal due to the absence of a phenolic hydroxyl group but is equally potent as MMV007839 (Golldack et al., 2017; Jakobowska et al., 2021; Spangenberg et al., 2013). (**C**) Removal of the hydroxyl and introduction of a hydrogen bond-accepting nitrogen into the aromatic ring yielded the most potent PfFNT inhibitor, BH267.meta (Nerlich et al., 2021; Walloch et al., 2020).

PfFNT was inhibited by MMV007839 with an IC_{50} of 170 nM when expressed and assayed for uptake of radiolabelled L-lactate in *Saccharomyces cerevisiae* yeast (Golldack et al., 2017). Similarly, an EC_{50} of 140 nM was observed with *Plasmodium falciparum* 3D7 parasites *in vitro* (Golldack et al., 2017; Jakobowska et al., 2021). Nevertheless, long-term treatment of cultured parasites with sublethal doses of a screening hit MMV007839 forced a PfFNT Gly107Ser resistance mutation, decreasing inhibitor affinity by two orders of magnitude (IC_{50} 21 µM, EC_{50} 35 µM) (Golldack et al., 2017; Hapuarachchi et al., 2017). The reduced inhibitor sensitivity is probably due to increased steric hindrance

and a clash of the phenyl-hydroxy group of MMV007839 with the serine side chain (Figure 1.9) (Lyu et al., 2021; Peng et al., 2021; Walloch et al., 2020).

PfFNT protomer   **MMV007839 in PfFNT**   **BH267.meta in PfFNT G107S**
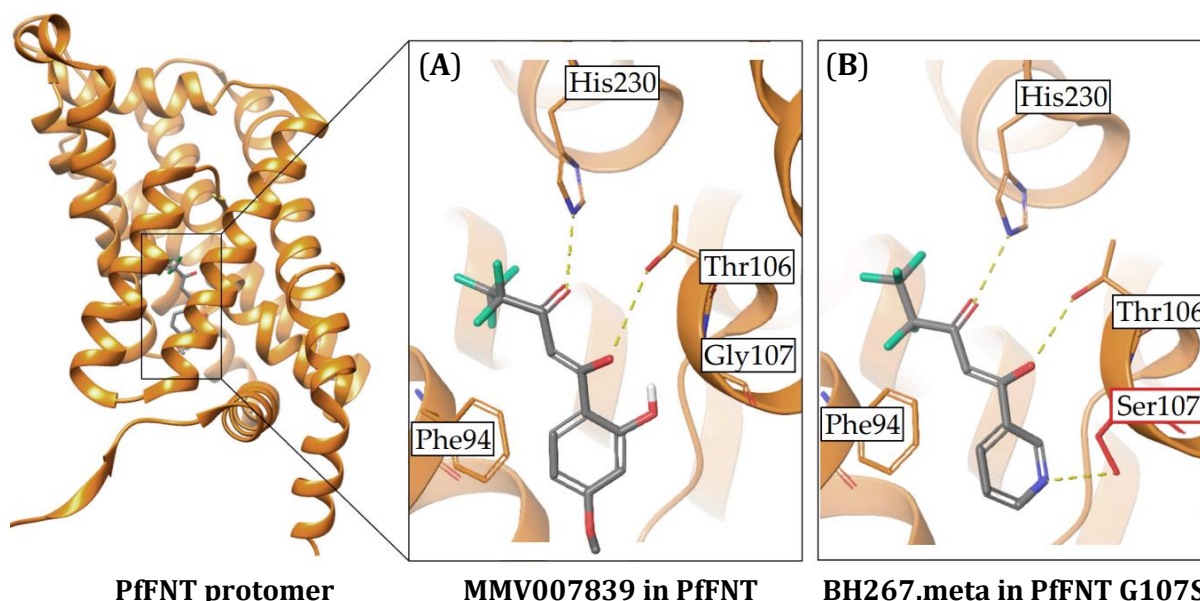
Figure 1.9 Binding mode of the PfFNT inhibitors. By resembling two successive lactate molecules, the linear fluoroalkyl/vinylogous acid moiety acts as a substrate analogue and binds extensively within the PfFNT transport path, thereby blocking the function of the transporter (Golldack et al., 2017; Jakobowska et al., 2021). The inhibitors' binding to PfFNT involves both hydrophilic and hydrophobic interactions (Peng et al., 2021). Three highly conserved polar residues of the central pore, Thr106, Gly107, and His230, form a hydrogen bond network with the vinylogous acid moiety, while the remaining part of the inhibitor contacts the hydrophobic part of the central pore *via* van der Waals interactions (Peng et al., 2021). The figure is reprinted from (Nerlich et al., 2021).

Through conducting structure-activity relationship (SAR) studies, a range of derivatives of MMV007839 have been synthesized and characterized in order to conquer the mutation that causes drug resistance (Golldack et al., 2017; Peng et al., 2021; Walloch et al., 2020). MMV007839 variant, BH296 (Figure 1.8B), lacking the phenolic hydroxyl group, which prevents the formation of a cyclic hemiketal, already improved binding to PfFNT G107S about 10-fold, yet still needed micromolar doses to be effective (Golldack et al., 2017; Spangenberg et al., 2013). A pyridine substitution of the original phenol moiety and removal of the methoxy group resulted in the most effective dual inhibitor, BH267.meta (Figure 1.8C; 1.9), which inhibited both PfFNT wild type (wt) and G107S at nanomolar concentrations (Peng et al., 2021; Walloch et al., 2020). BH267.meta, in addition to having high efficiency in killing cultured *P. falciparum* parasites (EC$_{50}$ 0.29 μM), also avoided the formation of drug resistance even when the parasites were treated with it for a long time (Peng et al., 2021; Walloch et al., 2020). According to a recent study, BH267.meta inhibits a wide range of FNTs, including all five human malaria-causing

agents, furthermore, the compound exhibits very low cytotoxicity toward human cells and minimal off-target activity on the human lactate transporter MCT1 (Nerlich et al., 2021; Walloch et al., 2021).

1.3   Fluorescence correlation spectroscopy (FCS)

Fluorescence correlation spectroscopy (FCS) is a powerful technique for detecting molecular interactions through the analysis of time-dependent intensity fluctuations, that are caused by fluorescently labelled molecules diffusing in and out of a microscopic volume due to their Brownian motion (Elson & Magde, 1974; Schwille & Haustein, 2001; Weidemann et al., 2002; Yu et al., 2021). Molecular parameters such as diffusion coefficients, local concentrations, or interaction of the molecules *in vivo* or *in vitro*, can be accurately measured with FCS (Dittrich et al., 2001; Lippincott-Schwartz et al., 2001; Medina & Schwille, 2002; Schwille, 2001; Yu et al., 2021). FCS was developed in the early 1970s, for the measurement of binding of the fluorescent dye EtBr and DNA (Magde et al., 1972; Yu et al., 2021), but became widely used with the discovery of single-molecule detection capabilities in 1993 (Rigler et al., 1993) and awareness of its enormous potential in biological sciences (Eigen & Rigler, 1994). Compared with other dynamics-orientated approaches, FCS can be carried out in physiological environments, thereby circumventing protein purification, which can be very difficult and take a long time (Lin & Guidotti, 2009; Medina & Schwille, 2002; Pina et al., 2014). Moreover, it is a non-invasive, fast and cost-effective method with high sensitivity, that can be applied to various systems ranging from solutions, and crude cellular extracts, to living cells (Bacia & Schwille, 2007; Muetze et al., 2011).

1.3.1   Basic theory of FCS

Fluctuation analysis is best performed when the system being studied is limited to very small ensembles at the single-molecule level and if the background is well suppressed (Medina & Schwille, 2002). To meet these criteria, a combination of low sample concentrations and extremely tiny measurement volumes must be employed (Chen et al., 2008; Medina & Schwille, 2002). Thus, nanomolar to picomolar sample concentrations are used to obtain clear changes in the fluorescence signal (Chen et al., 2008). When too many entities are measured at the same time, the relative fluctuations become less evident. On the other hand, if the individual fluctuation events are too sparse in time, one measurement can take too long (Lakowicz, 1999). The most popular implementation of

FCS uses a confocal-microscope setup, which allows for achieving a microscopic detection volume of about 10^{-15} L (1 femtoliter) by simply focusing a laser beam down to the resolution limit by an objective with a high numerical aperture (NA > 0.9) (Medina & Schwille, 2002; Rigler et al., 1993). The typical instrumental setup for an FCS experiment (Figure 1.10A) (Weisshart et al., 2004) consists of a laser line with a specific wavelength (ranging mostly from 405-633 nm), which is reflected into a microscope objective by a dichroic mirror and focused into an aqueous solution containing molecules under study that are labelled with a fluorescent dye (Schwille & Haustein, 2001). When the particles cross the focal volume, they are excited and the fluorescence emission is collected back through the same objective and separated from the excitation light by the dichroic mirror. Afterwards, the fluorescence light is focused through a pinhole onto an ultra-sensitive avalanche photodiode detector (APD) (Bacia & Schwille, 2007; Muetze et al., 2011; Yu et al., 2021). The recorded intensity fluctuations (Figure 1.10B) represent the diffusion events of the fluorescence molecules (Schwille & Haustein, 2001; Yu et al., 2021).
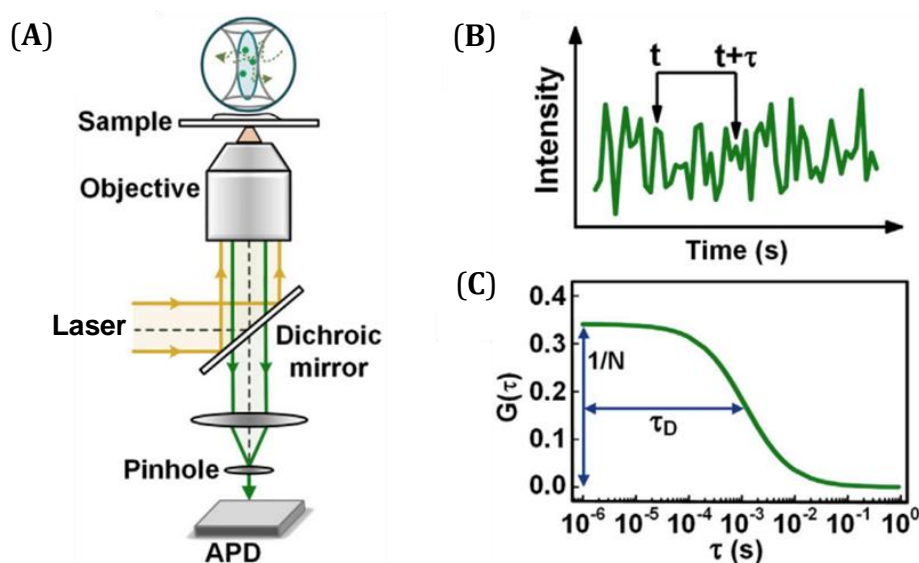
Figure 1.10 Confocal FCS instrumentation and principles. (**A**) Schematic representation of a typical confocal based FCS setup. (**B**) Example of the intensity trace collected during a measurement. (**C**) The autocorrelation curve generated using the intensity trace (Yu et al., 2021). The figure is reprinted from (Yu et al., 2021).

Although obtained raw data already contains all of the information on single-molecule dynamics, they must go through several steps of processing before the parameters of interest can be determined (Muetze et al., 2011). The fluctuations are analyzed by autocorrelation (Figure 1.10C) and adequate fitting algorithms to an appropriate biophysical diffusion model (Medina & Schwille, 2002; Schwille & Haustein, 2001). The

fluorescence intensity autocorrelation function (ACF) in FCS is given by Eq. (1) (Ries & Schwille, 2012; Schwille, 2001).

$$G(\tau) = \frac{\langle \delta F(t)\, \delta F(t + \tau) \rangle}{\langle F(t) \rangle^2} \tag{1}$$

where $F(t)$ is the fluorescence intensity at time t, $\langle F(t) \rangle = (1/T) \int_0^T F(t) dt$ denotes the time average of the signal, $\delta F(t) = F(t) - \langle F(t) \rangle$ is the deviation from the mean intensity and τ is the lag time, i.e., the time difference between two data points.

The autocorrelation curve measures the self-similarity of the signal in time, i.e., the overlap of a signal with itself at various time shifts τ, reflecting the probability that the signal at different times still belongs to the same molecular event (Ries & Schwille, 2012; Schwille, 2001; Yu et al., 2021). As a result, the autocorrelation curve's decay time τ_D (also known as diffusion time) is related to the time the molecules spend in the detection volume (Muetze et al., 2011; Ries & Schwille, 2012). For short lag times, the particles in the focal volume move only short distances and are likely to remain in that volume. Consequently, the signal's self-similarity is strong, and the resulting autocorrelation is high. The longer the lag time, the more likely it is that particles have diffused out of the volume, resulting in reduced self-similarity and autocorrelation decays to zero (Muetze et al., 2011).

The amplitude of the ACF is inversely proportional to the average number of observed molecules N in the detection volume V and hence to the fluorescent particle concentration C in solution, Eq. (2) (Ries & Schwille, 2012; Yu et al., 2021). This is due to the fact that if only a few molecules are present in the measurement volume on average, the relative change in fluorescence when one molecule enters or exits the measurement volume is significant (Yu et al., 2021). On the other hand, when a large number of molecules are already present in a tiny measurement volume, the relative change in recorded fluorescence when one molecule enters or leaves is low. Therefore, the amplitude of the ACF will be higher at low concentrations and vice versa (Gupta et al., 2019).

$$G(0) = \frac{1}{N} = \frac{1}{VC} \tag{2}$$

To extract physically relevant information, such as concentration, diffusion coefficient, and reaction rate constant, the calculated autocorrelation curve is fitted to an appropriate theoretical model. The simplest fitting formula for molecules undergoing free diffusion

through a confocal detection volume is a 3D Gaussian profile, Eq. (3) (Ries et al., 2010; Ries & Schwille, 2012).

$$G(\tau) = \frac{1}{N} \left(1 + \frac{\tau}{\tau_D}\right)^{-1} \left(1 + \frac{\tau}{S^2 \tau_D}\right)^{-1/2} \tag{3}$$

where N is an average number of particles inside the confocal volume, τ is the correlation time, S is the structure parameter, and τ_D is the translational diffusion time of the molecule.

1.3.2 Dual-colour fluorescence cross-correlation spectroscopy (FCCS)

Conventional FCS can only be used to monitor molecular interactions when the binding causes a resolvable difference in diffusion time, compared to individual molecules (Yu et al., 2021). However, even then, if a molecule binds to something else than its designated target, it will not be possible to distinguish this binding from non-specific interactions (Bacia & Schwille, 2007; Medina & Schwille, 2002; Muetze et al., 2011; Yu et al., 2021). Specific molecular interactions can be measured with an extension of FCS, called dual-colour FCS or fluorescence cross-correlation spectroscopy (FCCS) (Bacia & Schwille, 2007; Martinez-Moro et al., 2019; Tiwari et al., 2013).
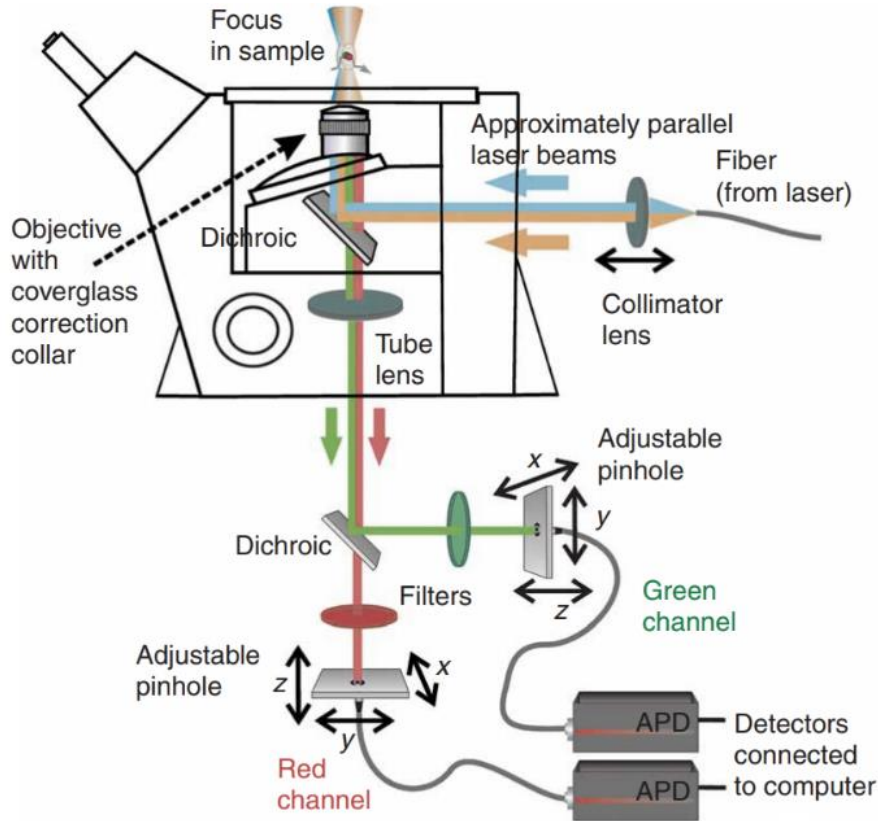
Figure 1.11 Sketch of a typical setup for dual-colour FCCS. The figure is reprinted from (Bacia & Schwille, 2007).

Introduction

The concept of FCCS was introduced by Eigen and Rigler in 1994 (Eigen & Rigler, 1994), and implemented experimentally by Schwille et al. in 1997 (Schwille et al., 1997; Yu et al., 2021). In dual-colour FCS, two species of interest are independently labelled with two spectrally distinct fluorescent probes (Schwille et al., 1997). These fluorophores are excited with two different emission wavelengths, and their emitted fluorescence, typically green and red, is split subsequently by dichroic mirrors and filters into the respective detection channels (Figure 1.11) (Rarbach et al., 2001). The simultaneous detection of two distinct dyes in a two-colour setup permits the capture of both the autocorrelation of each channel's signal and the cross-correlation of the two channels (Schwille et al., 1997). If the differently labelled molecules are not interacting with each other, then each molecule species has its own autocorrelation function. There will be no specific cross-correlation signal since the molecules move independently. However, if particles are bound to each other, they move together through the detection volume in a synchronized way, inducing simultaneous fluctuations of the fluorescence signals in both channels and thus a positive cross-correlation readout (Figure 1.12) (Bacia et al., 2006).
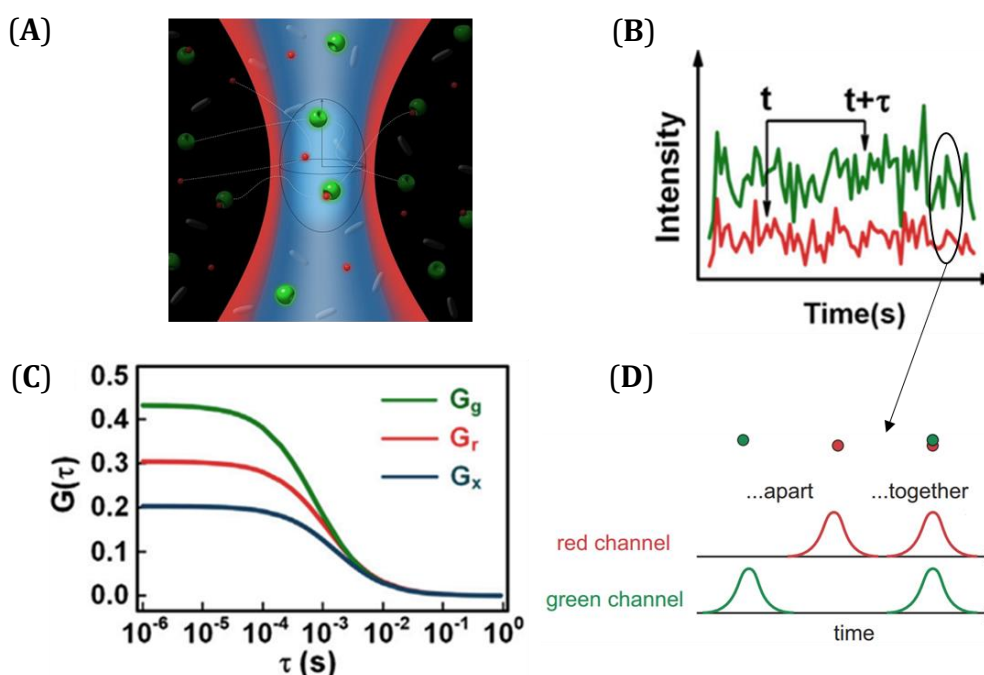
Figure 1.12 Illustration of dual-colour FCCS. (**A**) The detection scheme of FCCS. (**B**) Typical traces of the detected intensity as a function of time. (**C**) Autocorrelation and cross-correlation curves of the red and green intensity traces. (**D**) There will be a correlation between the red and green intensities only if the red and green molecules are bonded to reach other and co-diffuse (Yu et al., 2021). The figure is adapted from (Yu et al., 2021).

The number of diffusing particles carrying both dyes may be used for the analysis of molecular interactions such as binding at nanomolar concentrations (Bacia & Schwille,

2007; Thompson et al., 2002). The amount of binding can be quantified by comparing the amplitudes of the cross-correlation (CCF) with the amplitudes of the autocorrelation curves in the two channels. The cross-correlation function $G_{rg}(\tau)$ is shown in Eq. (4).

$$G_{rg}(\tau) = \frac{\langle \delta F_r(t)\, \delta F_g(t+\tau) \rangle}{\langle F_r(t) \rangle \langle F_g(t) \rangle} \tag{4}$$

defining $F_r(t)$ and $F_g(t)$ as the intensity in the red and green channel, respectively.

For solutions containing two species, the following expression is used to perform a two-component fit, Eq. (5) (Mittag et al., 2018).

$$G(\tau) = \frac{1}{N}\left[(1-y)\left(\frac{1}{1+\frac{\tau}{\tau_{D1}}}\right)\left(\frac{1}{1+\frac{\tau}{S^2\tau_{D1}}}\right)^{\frac{1}{2}} + y\left(\frac{1}{1+\frac{\tau}{\tau_{D2}}}\right)\left(\frac{1}{1+\frac{\tau}{S^2\tau_{D2}}}\right)^{\frac{1}{2}}\right] + 1 \tag{5}$$

where τ_1 and τ_2 describe the diffusion times of the first and second diffusing species and y is the fraction of the second component in the solution.

Despite the capabilities, there are certain challenges while performing FCCS (Kim et al., 2007; Ries et al., 2010). For instance, spectral crosstalk, which occurs when excitation and emission wavelengths of fluorescent dyes are overlapping, frequently results in a false-positive cross-correlation amplitude (Bacia et al., 2012; Földes-Papp, 2005; Lee et al., 2010; Yu et al., 2021). Also, improper focus overlap between two excitation lights and uncorrelated background caused by cell autofluorescence, extracellular environment, or stray lights incorrectly changes the cross-correlation amplitude (Kohl & Schwille, 2005; Schwille et al., 1999). Moreover, photobleaching of slow diffusing molecules at high laser powers is usually unavoidable during the measurements (Eckert et al., 2020; Yu et al., 2021). The photobleaching diminishes fluorescence intensity over time, resulting in a decrease in samples concentration (Eckert et al., 2020; Yu et al., 2021). It is also important to note that when dealing with samples that tend to aggregate, FCCS may not be the most suitable method. This is due to the fact that correlation curves may become poorly reproducible and a few bright aggregates might affect the whole data set (Mittag et al., 2018; Wang et al., 2018; Yu et al., 2021). Furthermore, dual-colour FCS does not apply to weak binding interactions, where too many molecules in the confocal volume would be required to get any detectable bound species (Bacia & Schwille, 2007). The majority of the issues mentioned above, however, may be avoided with proper calibration and sample preparation (Ries & Schwille, 2012).

1.4 Aim of this study

A novel malaria-fighting approach involves blocking lactate export in the parasitic protozoan *Plasmodium falciparum* (Jakobowska et al., 2021; Wu et al., 2015). Recent studies have identified small drug-like molecules that can impede the function of the sole plasmodial lactate transporter, PfFNT, and effectively eliminate parasites in culture (Golldack et al., 2017; Jakobowska et al., 2021; Walloch et al., 2020). Although the current efficiency values of PfFNT inhibitors were calculated using a yeast-based lactate transport assay, this method is inadequate for determining the inhibitor compounds' direct affinity and kinetic binding parameters to PfFNT (Jakobowska et al., 2021). The reason for this is that in order to reach the cytoplasmic transporter binding site, the drugs need to undergo transmembrane diffusion (Jakobowska et al., 2021).

The main objective of this project is to develop an FCCS-based assay to measure the true binding affinities and kinetic parameters of GFP-labelled PfFNT wild type and the G107S mutant to respective fluorescently labelled ligands (BH296, BH267.meta) and to determine equilibrium K_i-values, as well as k_{on} and k_{off} rate constants (Jakobowska et al., 2021). Eventually, a high throughput screening will be performed to find new potential PfFNT inhibitors.

2 Materials and Methods

2.1 Materials

2.1.1 Technical devices

Device	Model	Manufacturer
Agarose gel chamber	Sub Cell GT basic	Bio-Rad, München
Autoclave	Tuttnauer 3870ELV	Biomedis, Gießen
Bacterial incubator	Unitherm 6/12	UniEquip, Martinsried
Blotting device	Mini Trans-Blot® Cell	Bio-Rad, München
Cell culture bench	Hera HPH12	Heraues, Hannover
Cell culture incubator	Hera Cell 240	Heraues, Hannover
Centrifuge	CT15RE	Hitachi Koki, Tokyo
Centrifuge	Biofuge Pico	Heraues, Hannover
Centrifuge	Sigma 4-15	Qiagen, Hilden
Centrifuge	Rotofix 32A	Hettich, Tuttlingen
Centrifuge	Galaxy Mini C1213	VWR, Darmstadt
Centrifuge	Sorvall RC5C Plus	Thermo Fischer, Schwerte
Confocal microscope	Axiovert 200M	Zeiss, Jena
Developer	Curix 60	AGFA-Gevaert, Mortsel
Developer cassette	Hypercassette™	Amersham plc, Amerscham
Electroporator	E. coli Pulser™	Bio-Rad, München
FCCS spectroscope	LSM 510 ConfoCor 2	Zeiss, Jena
FCCS spectroscope	Insight	Evotec, Hamburg
Freeze dryer	Alpha 2-4 LSCbasic	Christ, Osterode am Harz
Freezer -20°C	GSS 3666	Liebherr, Bulle
Freezer -80°C	DW-86L578J	Haier, Qingdao
Freezing container	Mr. Frosty™	Thermo Fischer, Schwerte
Fridge 4°C	KTe 1630-24	Liebherr, Bulle
Gel imager	Syngene™ Ingenius	Syngene, Cambridge
Hemocytometer	Neubauer	Brand, Wertheim

Device	Model	Manufacturer
Homogeniser	Dounce 7 ml	VWR, Darmstadt
HPLC system	1100 Series	Agilent, Santa Clara
Ice machine	AF80	Scotsman, Łódź
Laboratory scale	ALC-80.4	Acculab, Göttingen
Laboratory scale	Vicon	Acculab, Göttingen
Light microscope	AE20	Motic, Hong Kong
Light microscope	Axio Vert.A1	Zeiss, Jena
Liquid dispenser	MANTIS® V3.3 ACC RFID	Formulatrix, Bedford
Liquid dispenser	Bravo 04730-201	Agilent, Santa Clara
Liquid nitrogen tank	Arpege 70	Air Liquide, Düsseldorf
Magnetic stirrer	MR3001	Heidolph, Schwabach
Magnetic stirrer	IKAMAG REO	IKA, Staufen im Breisgau
Microwave	800	Severin, Sudern
Microwave	R-939IN	Sharp, Sakai
Mini-shaker	3D Sunflower	Biosan, Steinfurt
Multichannel pipettes	0,5-10 µl and 50-300 µl	Thermo Fischer, Schwerte
PCR-cycler	Doppio	VWR, Darmstadt
pH-meter	FiveEasy	Mettler Toledo, Columbus
Pipettes	Classics P2, 20, 200, 1000	Gilson, Middleton, USA
Pipettes	ErgoOne P2, 20, 200, 1000	Starlab, Hamburg
Pipettor	accu-jet® pro	VWR, Darmstadt
Plate shaker	MicroMix 5	DPC, Bad Nauheim
Power supply	E802	Consort, Turnhout
Rotator mixer	Combi 1813	Labortechnik Fröbel, Lindau
SDS-PAGE chamber	Mini-PROTEAN Tetra Cell	Bio-Rad, München
Shaking incubator	Innova 4230	New Brunswick, Nürtingen
Sonicator	Sonoplus HD2070	Bandelin, Berlin
Spectrophotometer	Epoch microplate	Agilent, Santa Clara
Spectrophotometer	Biowave II	WPA, Cambridge

Device	Model	Manufacturer
Sterile work bench	2-453-GAND	Köttermann, Uetze
Thermoblock	Thermomixer 5436	Eppendorf, Hamburg
Vacuum concentrator	RVC 2-33 CDplus	Christ, Osterode am Harz
Vacuum pump	PM20405-86	VWR, Darmstadt
Vortexer	Vortex-Genie™ 2	Scientific Industries, Roth
Water bath	1002	UniEquip, Martinsried
Water purification system	Aquintos	Aquintos, Niederrhein

2.1.2 Disposables

Disposables	Specifications	Manufacturer
Aluminium foil	For microplates	VWR, Darmstadt
Assay plates	Costar® 96-well half area	Corning, Kennebunk
Cell culture microplate	96-well	Greiner bio-one, Frickenhausen
Cell culture plates	10/15 cm	Sarstedt, Nümbrecht
Cell culture plates	6/12/24/96-well	Sarstedt, Nümbrecht
Chemiluminescence film		GE Healthcare, Freiburg
Chromatography paper	3MM CHR	GE Healthcare, Freiburg
Conical falcon tubes	15/50 ml	Sarstedt, Nümbrecht
Cryo-pro labels		VWR, Darmstadt
Cryotubes	1.6 ml	Sarstedt, Nümbrecht
Culture tubes	With closures, 14 ml	VWR, Darmstadt
Deep well storage microplate	96-well, 2.2 ml square wells	Neobits, Sunnyvale
Eppendorf tubes	1.5/2/5 ml	VWR, Darmstadt
Erlenmeyer flask	250/1000 ml	VWR, Darmstadt
Glass bottom assay plates	384-well	SWISSCI, Zug
Gloves	Nitrile	Kimtech, Roswell
Inoculating loops		VWR, Darmstadt
Lid for microplates		Greiner bio-one, Frickenhausen

Disposables	Specifications	Manufacturer
Nitrocellulose blotting membrane	Amersham, 0.45 µm	GE Healthcare, Freiburg
Parafilm		Pechiney, Menasha
Pasteur pipettes	1 ml	Brand, Wertheim
PCR reaction tubes	Strips of 8 tubes, 0.2 ml	Brand, Wertheim
Petri dishes	10 cm	Sarstedt, Nümbrecht
Pipette tips	1-10/20-200/100-1000 µl	VWR, Darmstadt
Pipette tips	10, 30, 70 µl	Agilent, Santa Clara
Pipetting reservoirs	50 ml	VWR, Darmstadt
Polypropylene film	For microplates	VWR, Darmstadt
Polypropylene storage microplates	Nunc™, 384-well	Thermo Fischer, Schwerte
Scalpel		Braun, Tuttlingen
Serological pipettes	5/10/25 ml	Sarstedt, Nümbrecht
Syringe	Omnifix 50 ml	Braun, Melsungen
Syringe filter	0.2 µm	VWR, Darmstadt
Transfection cuvettes	0.1 cm	Bio-Rad, München
UV-micro cuvettes	70 µl micro	Brand, Wertheim

2.1.3 Chemicals

Reagent	Manufacturer
3-[(3-cholamidopropyl)dimethylammonio]-1-propanesulfonate (CHAPS)	Anatrace, Maumee
30% Acrylamide/Bis solution	Bio-Rad, München
Acetic acid	Roth, Karlsruhe
Acetonitril ROTISOLV® HPLC (ACN)	Roth, Karlsruhe
Agar-Agar	Carl Roth, Karlsruhe
Agarose	AppliChem, Darmstadt
Ammonium persulfate (APS)	Applichem, Darmstadt
Ampicillin	Roche, Mannheim
Antarctic phosphatase reaction buffer	Biolabs, Frankfurt am Main

Materials and Methods

Reagent	Manufacturer
ATP	Thermo Fischer, Schwerte
AZD3965	Hycultec, Beutelsbach
BioWhittaker® Hank's Balanced Salt Solution without phenol red (HBSS)	Lonza, Walkersville
Bromophenol blue	Applichem, Darmstadt
Cholesteryl hemisuccinate (CHS)	Anatrace, Maumee
cOmplete™ protease inhibitor cocktail, EDTA-free (PIC)	Roche, Mannheim
CutSmart® buffer	Biolabs, Frankfurt am Main
Developer	Agfa, Mortsel
Dimethyl sulfoxide (DMSO)	Carl Roth, Karlsruhe
Disodium phosphate (Na_2HPO_4)	Merck, Darmstadt
Ethanol, absolute	AppliChem, Darmstadt
Ethidium bromide solution 0.025 % (EtBr)	Roth, Karlsruhe
Ethylenediaminetetraacetic acid (EDTA)	Merck, Darmstadt
Glycerol, for analysis, 86-88%	Thermo Fisher, Dreieich
Glycine	Applichem, Darmstadt
HEPES	AppliChem, Darmstadt
Hydrochloric acid (HCl)	Merck, Darmstadt
Isopropanol	Chemsolute, Renningen
KLD reaction buffer	Biolabs, Frankfurt am Main
Lauryl Maltose Neopentyl Glycol (LMNG)	Anatrace, Maumee
LB-medium (Lennox)	Carl Roth, Karlsruhe
MassRuler™ DNA Loading Dye	Thermo Fisher, Rockford
Metformin hydrochloride	MP Biomedicals, Santa Ana
N,N-Diisopropylethylamine (DIEA/DIPEA)	Merck, Darmstadt
Natriumchloride (NaCl)	Chemsolute, Renningen
Natriumhydroxide (NaOH)	AppliChem, Darmstadt
n-Decyl β-maltoside (DM)	Anatrace, Maumee
n-Dodecyl-N,N-Dimethylamine-N-Oxide (LDAO)	Anatrace, Maumee
n-Dodecyl-β-D-maltopyranoside (DDM)	Anatrace, Maumee

Reagent	Manufacturer
Nonfat dried milk powder	AppliChem, Darmstadt
pHrodo™ Red AM Intracellular pH Indicator	Invitrogen, Waltham
Ponceau S	Roth, Karlsruhe
Potassium chloride (KCl)	Merck, Darmstadt
Rapid fixer	Agfa, Mortsel
Sodium dihydrogen phosphate (NaH_2PO_4)	Merck, Darmstadt
Sodium dodecyl sulfate (SDS)	AppliChem, Darmstadt
Syrosingopine	Extrasynthese, Genay
T4 DNA Ligase Buffer	Biolabs, Frankfurt am Main
T4 polynucleotide kinase reaction buffer	Biolabs, Frankfurt am Main
Tetramethylethylenediamine (TEMED)	Roth, Karlsruhe
Trifluoroacetic acid (TFA)	Roth, Karlsruhe
Tris	Carl Roth, Karlsruhe
Tris buffered saline (TBS)	Fisher, Geel
Triton™ X-100	Applichem, Darmstadt
Trypton/pepton from casein	Roth, Karlsruhe
Tween® 20	Roth, Karlsruhe
Water for molecular biology	Merck, Darmstadt
Xylene cyanol	Merck, Darmstadt
Yeast extract	Carl Roth, Karlsruhe
β-Mercaptoethanol	Thermo Fisher, Bleiswijk

2.1.4 Cell culture reagents and supplements

Reagent	Manufacturer
Blasticidin S	AppliChem, Darmstadt
Collagen, type I solution from rat tail	Merck, Darmstadt
Dimethyl sulfoxide for cell culture (DMSO)	AppliChem, Darmstadt
Fetal Bovine Serum (FBS)	Biochrom, Berlin
Gibco® 0.05% Trypsin-EDTA	Thermo Fisher, Bleiswijk
Gibco® Dulbecco's Phosphate Buffered Saline (DPBS)	Thermo Fisher, Bleiswijk

Reagent	Manufacturer
Gibco® Dulbecco's Modified Eagle Medium (DMEM)	Thermo Fisher, Bleiswijk
Gibco® Penicillin (10000 U/ml)/Streptomycin (10000 µg/ml) (Pen Strep)	Thermo Fisher, Bleiswijk
Tetracycline hydrochloride	AppliChem, Darmstadt
Zeocin	Invitrogen, Waltham

2.1.5 Enzymes

2.1.5.1 Polymerases

Polymerase	Manufacturer
Phusion High-Fidelity PCR Master Mix	Thermo Fischer, Schwerte
Q5® Hot Start High-Fidelity 2x Master Mix	Biolabs, Frankfurt am Main

2.1.5.2 Ligases

Ligase	Manufacturer
KLD Enzyme Mix	Biolabs, Frankfurt am Main
T4 DNA ligase	Biolabs, Frankfurt am Main

2.1.5.3 Kinases

Kinase	Manufacturer
T4 Polynucleotide Kinase	Biolabs, Frankfurt am Main

2.1.5.4 Hydrolases

Hydrolase	Manufacturer
Antarctic Phosphatase	Biolabs, Frankfurt am Main

2.1.5.5 Restriction enzymes

Restriction enzyme	Restriction site	Manufacturer
EcoRI	5'...G▾AATTC...3' 3'...CTTAA▴G...5'	Biolabs, Frankfurt am Main
HindIII	5'...A▾AGCTT...3' 3'...TTCGA▴A...5'	Biolabs, Frankfurt am Main

Restriction enzyme	Restriction site	Manufacturer
XhoI	5'...C▾TCGAG...3' 3'...GAGCT▴C...5'	Biolabs, Frankfurt am Main

2.1.6 Antibodies

Type	Antigen	Conjugate	Organism	Dilution	Source
Primary	GFP	Un-conjugated	Mouse	1:2000	Roche, Mannheim
Secondary	Mouse	HRP	Goat	1:10000	Cayman, Ann Arbor

2.1.7 Kits

Kit	Manufacturer
Amersham™ ECL Western Blotting Detection Kit	GE Healthcare, Freiburg
E.Z.N.A.® Plasmid DNA Mini Kit I	Omega Bio-Tek, Norcross
Pierce™ BCA Protein Assay Kit	Thermo Fisher, Rockford
Polyplus jetPRIME® Transfection Kit	Polyplus, Illkirch
Q5® Site-Directed Mutagenesis Kit	Biolabs, Frankfurt am Main
QIAGEN® Plasmid Plus Midi Kit	Qiagen, Hilden
QIAquick® Gel Extraction Kit	Qiagen, Hilden

2.1.8 DNA- and protein-ladders

DNA- or protein-ladder	Manufacturer
GeneRuler™ 1 kb Plus DNA Ladder	Thermo Fisher, Rockford
MassRuler Express Forward DNA Ladder Mix	Thermo Fisher, Rockford
PageRuler™ Prestained Protein Ladder	Thermo Fisher, Rockford

2.1.9 Oligonucleotides

2.1.9.1 Primers for sequencing

Primer name	Sequence (5'→3')
CMVmin	CGCCATCCACGCTGTTTTG
pEGFPN1rev	GTCCAGCTCGACCAGGATG

2.1.9.2 Primers for *in vitro* mutagenesis

Primer name	Sequence (5'→3')
Q5SDM_11/21/2020_F	TTTGTTTACCagtAATACACTAGCGG
Q5SDM_11/21/2020_R	TCCGAACCGGTACAGATG

2.1.9.3 PCR primers

Primer name	Sequence (5'→3')
PfFNT-E1-for	GTCGACGAATTCGCCATGCCTCCCAACAACTCGAAATATG
PfFNT-H3-X1-rev	GCCGCCCTCGAGTCAAAGCTTGTTGCGCAGTTCAATGCTCAG

2.1.10 Media, buffers and solutions

2.1.10.1 Bacterial culture

Media/buffer/solution	Components
1x LB-medium	1% (w/v) NaCl
	0.5% (w/v) Trypton/pepton from casein
	1% (w/v) Yeast extract
	in dH_2O, autoclaved and poured into Petri dishes (~25 ml/100 mm plate)
Ampicillin stock solution	100 mg/ml in 70% Ethanol
Glycerol freezing solution	50% (v/v) Glycerol in 1x LB-medium
LB-agar plate solution	1.5% (w/v) Agar-Agar in 1x LB-medium

2.1.10.2 Molecular biology analyses

Media/buffer/solution	Components
50x TAE buffer	2 M Tris base
	1 M Pure acetic acid
	50 mM EDTA
	pH 8.5
6x Loading buffer	40% (v/v) Glycerol
	2.5% (w/v) Xylene cyanol
	2.5% (w/v) Bromophenol blue

Media/buffer/solution	Components
6x Loading buffer	in dH$_2$O
Agarose gel	1% (w/v) Agarose in 1x TAE

2.1.10.3 Cell biology and biochemical assays

Media/buffer/solution	Components
10x PBS	5.7 g Na$_2$HPO$_4$
	1.25 g NaH$_2$PO$_4$
	15.2 g NaCl
	fill up to 1 l with dH$_2$O, pH 7.4
25x Protease inhibitor cocktail (PIC)	1 Tablet in 2 ml dH$_2$O
Cell lysis buffer	1% (v/v) LMNG
	1x Protease inhibitor cocktail
	in TBS
Complete growth medium	500 ml DMEM
	50 ml FBS
	5 ml Penicillin (10000 U/ml)/ Streptomycin (10000 µg/ml)
Cryo-freezing solution	90% (v/v) FBS
	10% (v/v) DMSO for cell culture
Wash solution	20 mM HEPES in HBSS

2.1.10.4 Protein analyses

Media/buffer/solution	Components
10x SDS-PAGE running buffer	0.025 M Tris base
	0.192 M Glycine
	1% (w/v) SDS
	in dH$_2$O
10x TBS	50 mM Tris-HCl
	150 mM NaCl, pH 7.4
	in dH$_2$O
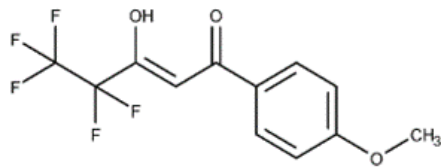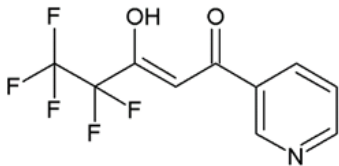
Media/buffer/solution	Components
4x Laemmli buffer	250 mM Tris-HCl
	8% (w/v) SDS
	40% (v/v) Glycerol
	0.02% (w/v) Bromophenol blue
	8% (v/v) ß-mercaptoethanol
Ammonium persulfate (APS)	10% (w/v) APS in dH_2O
Blocking solution	5% (w/v) Milk powder in TBS-T
Ponceau S	0.1 % (w/v) in 5% Acetic acid
Separating gel (for two gels, 10%)	3 ml Separating gel buffer
	4.76 ml dH_2O
	4 ml Bis-acrylamide (30%)
	120 µl SDS (10%)
	120 µl APS (10%)
	12 µl TEMED
Separating gel buffer	1.5 M Tris-HCl, pH 8.8 in dH_2O
Stacking gel (for two gels, 4%)	0.75 ml Stacking gel buffer
	4.33 ml dH_2O
	800 µl Bis-acrylamide (30%)
	60 µl SDS (10%)
	60 µl APS (10%)
	6 µl TEMED
Stacking gel buffer	1 M Tris-HCl, pH 6.8 in dH_2O
Substrate solution for western blot	0.5 ml Luminol/enhancer solution
	0.5 ml Peroxide solution
TBS-T	50 mM Tris-HCl, pH 7
	138 mM NaCl
	2.7 mM KCl
	0.05% (v/v) Tween-20
Towbin transfer buffer	0.025 M Tris base

Media/buffer/solution	Components
	0.192 M Glycine
Towbin transfer buffer	10% (v/v) Isopropanol
	in dH$_2$O

2.1.10.5 HPLC

Media/buffer/solution	Components
Buffer A	dH$_2$O
	0.1% (v/v) TFA
Buffer B	Acetonitrile
	0.1% (v/v) TFA

2.1.11 Inhibitors

Name/provider	Structure
BH296 (Beitz lab, CAU Kiel)	
BH267.meta (Beitz lab, CAU Kiel)	

2.1.12 Fluorescent dyes

Dye name	Manufacturer
DY-647-PEG4	Dyomics, Jena

2.1.13 Computer software

Software	Company
Agilent ChemStation	Agilent, Santa Clara
AxioVision	Zeiss, Jena
CLC Workbench 6	CLC-Bio, Aarhus
FCS+plus Analyze 1.1P	Evotec, Hamburg

Software	Company
FCSPP-Control 20	Evotec, Hamburg
InGenius analysis software	Syngene, Cambridge
LSM 510	Zeiss, Jena
MANTIS 4.3	Formulatrix, Bedford
TIBCO Spotfire	TIBCO, Palo Alto
VWorks	Agilent, Santa Clara
ZEN Black	Zeiss, Jena

2.1.14 Bacterial strains

Name/provider	Description
Bacterial strain *E. coli* DH10B (Biolabs, Frankfurt am Main)	Genotype: Δ(ara-leu) 7697 araD139 fhuA ΔlacX74 galK16 galE15 e14 φ80dlacZ ΔM15 recA1 relA1 endA1 nupG rpsL (StrR) rph spoT1 Δ(mrr-hsdRMS-mcrBC)

2.1.15 Cell lines

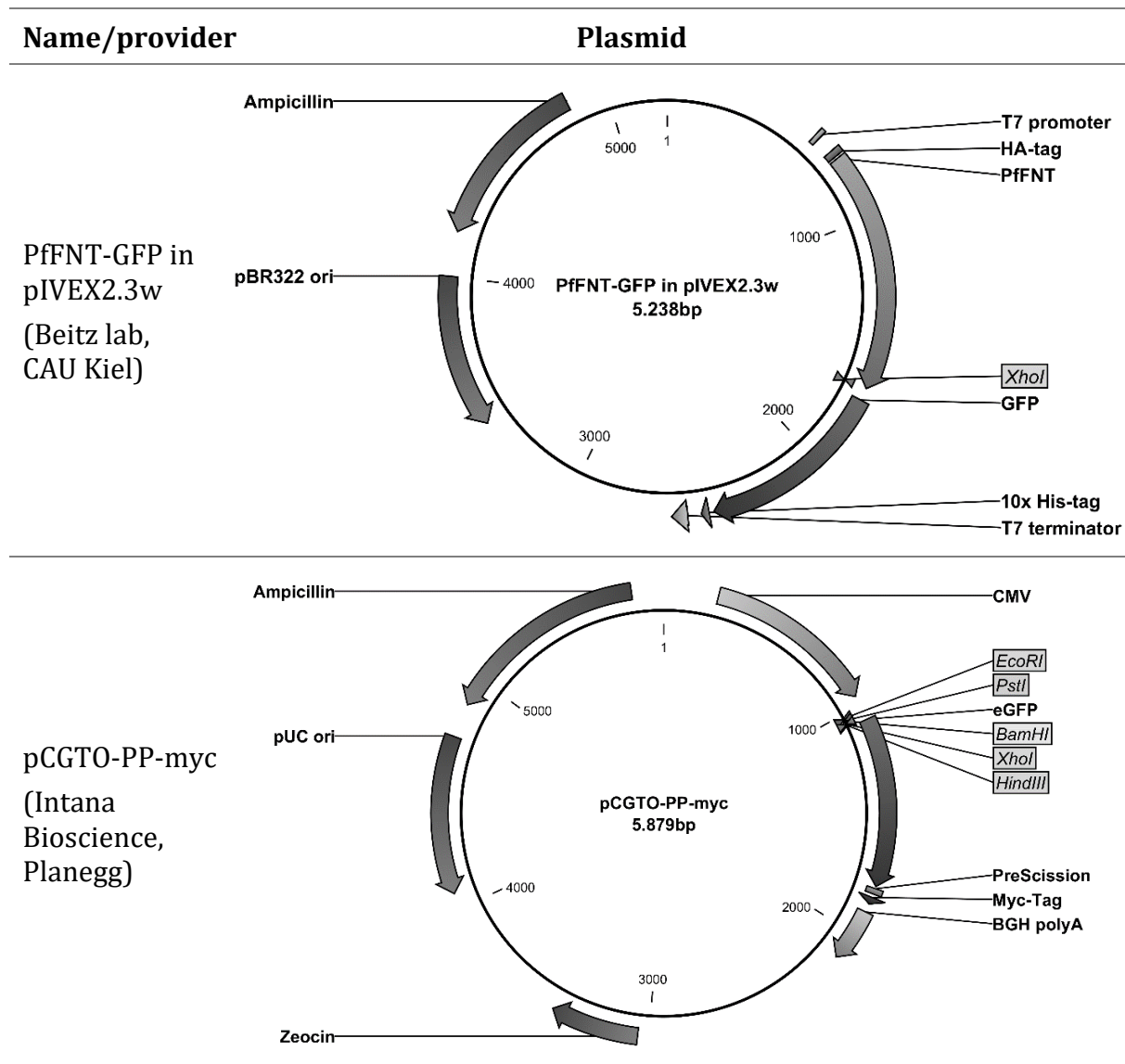| Name/provider	Description
HEK293-T-Rex (Intana Bioscience, Planegg)	Human embryonic kidney cells stably transfected with TET-repressor encoding sequence for tetracycline-regulated expression of the gene of interest

2.1.16 Coding sequences

PfFNT wt (NCBI Gene-ID: 814480)

```
  1 ATGCCACCAA ATAATTCCAA ATATGTTTTA GATCCAGTAA GCATAAAATC TGTTTGTGGA
 61 GGGGAAGAAT CATATATTAG ATGTGTTGAA TATGGGAAAA AAAAAGCGCA TTATAGTAAT
121 TTAAATTTAT TAGCAAAAGC TATATTAGCT GGTATGTTTG TTGGACTTTG TGCACACGCT
181 TCCGGAATAG CAGGAGGGTT GTTTTATTAT CACAAATTAA GAGAAATCGT AGGAGCATCG
241 ATGAGTGTGT TTGTATATGG TTTTACCTTT CCTATAGCTT TTATGTGTAT TATATGTACA
301 GGTTCTGATT TGTTTACGGG TAATACTTTA GCAGTAACCA TGGCATTATA TGAGAAGAAA
361 GTAAAACTAT TGGATTATTT GCGAGTTATG ACTATATCAT TATTCGGAAA TTATGTTGGT
421 GCTGTATCTT TTGCATTTTT TGTTTCTTAT TTATCTGGAG CATTTACTAA TGTTCATGCT
481 GTAGAGAAAA ATCATTTTTT CCAATTTTTA AATGATATAG CTGAAAAAAA GGTTCATCAT
541 ACATTTGTTG AATGTGTGTC ATTAGCTGTG GGCTGTAACA TATTTGTATG TTTGGCAGTA
601 TATTTTGTAT TAACCTTAAA AGATGGTGCA GGTTATGTAT TCAGTGTATT TTTTGCTGTT
661 TATGCTTTCG CTATAGCAGG ATATGAACAT ATTATAGCAA ATATTTATAC ACTAAATATT
721 GCCTTAATGG TTAATACAAA AATTACTGTA TATCAAGCAT ATATAAAAAA TTTATTACCC
781 ACCTTGTTAG GAAATTACAT TGCTGGTGCA ATTGTTTTGG GTTTACCATT GTATTTTATT
841 TATAAAGAGC ATTATTATAA TTTTGAAAGA TCGAAAAGAG ATAACAATGA TGCTCAAATG
901 AAAAGTTTAT CTATAGAATT ACGAAATTGA
```

2.1.17 Expression plasmids

Name/provider	Plasmid

PfFNT-GFP in pIVEX2.3w
(Beitz lab, CAU Kiel)

Ampicillin — T7 promoter — HA-tag — PfFNT
pBR322 ori — PfFNT-GFP in pIVEX2.3w 5.238bp — XhoI — GFP
5000, 1, 1000, 4000, 2000, 3000
10x His-tag — T7 terminator

pCGTO-PP-myc
(Intana Bioscience, Planegg)

Ampicillin — CMV
pUC ori — pCGTO-PP-myc 5.879bp — EcoRI — PstI — eGFP — BamHI — XhoI — HindIII
5000, 1, 1000, 4000, 2000, 3000
Zeocin — PreScission — Myc-Tag — BGH polyA

2.2 Methods

2.2.1 Microbiological methods

2.2.1.1 Preparation of consumables, media and solutions

Heat stable consumables, media, and solutions were autoclaved for 20 minutes at 121°C and 15 psi. To eliminate bacteria and viruses from non-heat stable media and solutions, mechanical filters with a pore size of 0.2 μm were used.

2.2.1.2 Production of electrocompetent *E. coli* cells

20 ml of LB-medium was inoculated with the *E. coli* DH10B starter culture from a glycerol stock and incubated overnight at 37°C with vigorous shaking. 10 ml of this culture was then transferred to an Erlenmeyer flask containing 1 l of LB-medium and incubated at

37°C with vigorous shaking up to an OD_{600} of 0.35–0.4. When the OD_{600} reached 0.35 the cells were immediately placed on ice and chilled for 30 minutes with occasional stirring to ensure even cooling. Next, the cells were harvested by centrifugation at 4000 x g for 15 min at 4°C and the pellet was resuspended in 1 l of ice-cold dH_2O. Then the cells were pelleted again, washed by adding 20 ml of chilled 10% glycerol and centrifuged for 15 min. The washing cycles were repeated three times. After the final centrifugation step, the pellet was resuspended in 3 ml of 10% glycerol by gently swirling and aliquoted (100 µl) into 1.5 ml reaction tubes and stored at -80°C.

2.2.1.3 Electroporation

2 µl of the respective plasmid-DNA was added to 30 µl of electrocompetent Ampicillin-resistant DH10B *E. coli* cells and carefully transferred into a chilled electroporation cuvette without introducing bubbles. The cells were electroporated at 1.8 kV. Next, the cells were transferred into a 1.5 ml tube containing 1 ml of LB-media and incubated for 30 min at 37°C while gently shaking. Then 100 µl of cell suspension was plated on agar plates containing Ampicillin (100 µg/ml) using an inoculating loop under sterile conditions and incubated overnight at 37°C.

2.2.1.4 Transformation of chemically competent *E. coli*

2 µl of the respective plasmid-DNA was added to 25 µl of chemical competent Ampicillin-resistant DH10B *E. coli* cells. After incubating on ice for 30 min, cells were heat-shocked in a water bath at 42°C for 40 s and rapidly cooled down on the ice for 5 min. Subsequently, 500 µl of pre-heated (37°C) LB-medium was added and the cells were incubated for 30 min at 37°C while gently shaking. Then 100 µl of cell suspension was plated on agar plates containing Ampicillin (100 µg/ml) using an inoculating loop under sterile conditions and incubated overnight at 37°C.

2.2.1.5 Culture and storage of transformed *E. coli*

After transformation of the respective plasmid into *E. coli* cells, one single clone was picked and transferred to either 5 ml (Miniprep) or 50 ml (Midiprep) of LB-medium containing 5 µl or 50 µl Ampicillin (stock: 1 mg/ml). The bacteria culture was incubated on a shaker at 37°C overnight. For long-term preservation glycerol stocks were made by mixing an aliquot (500 µl) of bacteria suspension-cultured overnight in LB-medium with 500 µl of 87% glycerol in a 1.5 ml reaction tube and stored at -80°C.

2.2.2 Molecular biological methods

2.2.2.1 Isolation of plasmid-DNA from an overnight culture

DNA isolation was performed from 5 ml *E. coli* overnight cultures using the E.Z.N.A.® Plasmid DNA Mini Kit I (Omega Bio-Tek, Norcross) or for high amounts of plasmid from 50 ml *E. coli* overnight cultures using the QIAGEN® Plasmid Plus Midi Kit (Qiagen, Hilden) following manufacturer's protocol. These preparations are based on the principle of alkaline cell lysis followed by DNA binding to a silica membrane under physiological conditions. In brief, bacterial overnight cultures were harvested by centrifuging at 10000 x g for 1 min (Midiprep 4000 x g for 15 min). Pelleted bacteria were resuspended in suspension buffer and lysed with lysis buffer for 5 min at room temperature. Next, the samples were incubated with a neutralization buffer and centrifuged for 10 min at 13000 x g. The cleared supernatant was transferred into filter columns and centrifuged for 1 min at 13000 x g. After two washing steps, the elution was performed in small volumes of either 30 µl Elution Buffer for Minipreps or 200 µl for Midipreps. The isolated plasmid DNA was stored at 4°C for a short time or at -20°C for permanent storage.

2.2.2.2 Determination of DNA concentration

DNA concentration was determined using an Epoch microplate reader (Agilent, Santa Clara) or a Biowave II spectrophotometer (WPA, Cambridge). The maximum peak of absorption DNA, 260 nm (A260), was measured. An optical density (OD) of 1 at 260 nm corresponds to a concentration of 50 µg/ml for doubled-stranded DNA.

2.2.2.3 Amplification of DNA using polymerase chain reaction (PCR)

Polymerase chain reaction (PCR) was used to amplify specific DNA fragments. PCR relies on a thermostable DNA-polymerase together with dNTPs (Phusion High-Fidelity PCR Master Mix, Thermo Fischer, Schwerte) and requires a pair of oligonucleotides (primers), which flanks both sites of the DNA region of interest. The DNA is amplified through consecutive cycles of different temperatures. During the denaturation phase (98°C), the double-strand DNA template is separated into single-strand DNA. Next, the temperature is lowered to approximately 5°C below the melting temperature of the primers to promote primer binding to the template. Optimal annealing temperatures were identified with the NEB TM Calculator Software (http://tmcalculator.neb.com). To decrease off-target priming and hence to increase the specificity of PCR reaction touchdown PCR was used, i.e., a cycling program where the annealing temperature is gradually reduced (e.g.,

1-2°C/every second cycle). Finally, during the extension phase, the DNA-polymerase synthesizes the complementary DNA strand in a direction 5'→3' at the optimal temperature for its performance, 72°C. Elongation times were adjusted according to the expected size of the PCR product. The mentioned cycle is repeated usually between 25 and 35 times, resulting in exponential amplification of the amplicon. To check the purity and the correct size of the generated amplicons agarose gel electrophoresis was employed.

Reaction components per PCR

Reagent	Volume
2x Phusion High-Fidelity PCR Master Mix	25 µl
Forward Primer (10 µM)	1 µl
Reverse Primer (10 µM)	1 µl
Template DNA (1-200 ng/µl)	1 µl
dH$_2$O	up to 50 µl

PCR cycling steps

PCR step	Temperature	Time	Cycles
Initial denaturation	98°C	1 min	1
Denaturation	98°C	5 s	
Annealing	70→60°C	30 s	30
Elongation	72°C	2 min	
Final elongation	72°C	5 min	1
Final hold	12°C	∞	-

2.2.2.4 Site-directed mutagenesis

The G107S point mutation was introduced in the plasmid by site-directed mutagenesis using the Q5® Site-Directed Mutagenesis Kit (Biolabs, Frankfurt am Main) after the manufacturer's protocol. Briefly, plasmid DNA encoding the protein of interest was used as a template for plasmid amplification. For site-specific base substitutions, the forward oligonucleotide primer contained respective nucleotide exchanges. The reverse oligonucleotide primer was designed to complementary bind sequences flanking the mutation region. The primers were designed using the NEBaseChanger (https://nebasechanger.neb.com). After the cycler reaction, DpnI treatment was

performed to digest the parental plasmid. Therefore, 1 µl of DpnI enzyme was directly added to each reaction mix and incubated for 10 min at 37°C. Subsequently, competent *E. coli* cells were transformed with the mutated plasmid DNA.

Reaction components per PCR

Reagent	Volume
Q5® Hot Start High-Fidelity 2x Master Mix	12.5 µl
Forward Primer (10 µM)	1.25 µl
Reverse Primer (10 µM)	1.25 µl
Template DNA (1-25 ng/µl)	1 µl
dH$_2$O	up to 25 µl

PCR cycling steps

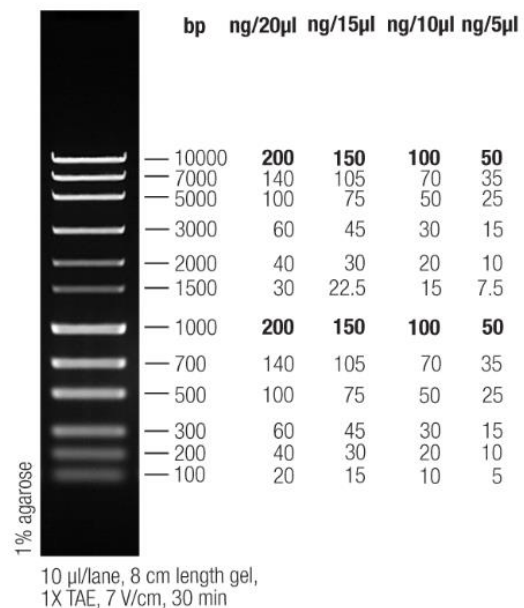| PCR step	Temperature	Time	Cycles
Initial denaturation	98°C	30 s	1
Denaturation	98°C	10 s	
Annealing	62°C	30 s	25
Elongation	72°C	3 min 30 s	
Final elongation	72°C	2 min	1
Final hold	12°C	∞	-

2.2.2.5 Agarose gel electrophoresis

The size of the DNA fragments was determined by agarose gel electrophoresis. DNA molecules are negatively charged due to their phosphate backbone and can thus be separated in an electric field as they are forced to move towards the anode according to their size. The gels were prepared by dissolving 1% (w/v) agarose powder in 50 ml TAE buffer (1x) in a microwave and adding DNA-intercalating ethidium bromide to a final concentration of 1 µg/ml (Wilcke, 2018). Afterwards, the solution was cooled down, transferred to a gel tray and a comb was inserted to generate pockets for DNA loading. Once the gel was hardened, the comb was removed and the gel was placed into an electrophoresis chamber, which was filled with 1x TAE buffer. Then, the samples were mixed with the appropriate amount of the 6x loading dye, loaded into the pockets and the electrophoresis was performed at 100 V for 30 min. As a marker, the GeneRuler™ 1 kb Plus DNA Ladder or the MassRuler Express Forward DNA Ladder Mix was loaded in

parallel with the samples. Afterwards, the separated DNA fragments were visualized by exciting ethidium bromide fluorescence ($\lambda = 302$ nm) using a UV transilluminator and the images were captured with a digital camera.
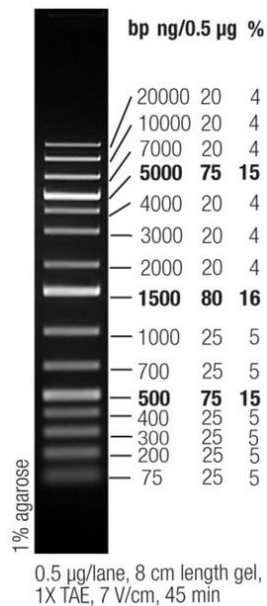
bp	ng/0.5 µg	%
20000	20	4
10000	20	4
7000	20	4
5000	75	15
4000	20	4
3000	20	4
2000	20	4
1500	80	16
1000	25	5
700	25	5
500	75	15
400	25	5
300	25	5
200	25	5
75	25	5

1% agarose
0.5 µg/lane, 8 cm length gel,
1X TAE, 7 V/cm, 45 min

GeneRuler™ 1 kb Plus DNA Ladder
(Thermo Fisher, Rockford)

bp	ng/20µl	ng/15µl	ng/10µl	ng/5µl
10000	200	150	100	50
7000	140	105	70	35
5000	100	75	50	25
3000	60	45	30	15
2000	40	30	20	10
1500	30	22.5	15	7.5
1000	200	150	100	50
700	140	105	70	35
500	100	75	50	25
300	60	45	30	15
200	40	30	20	10
100	20	15	10	5

1% agarose
10 µl/lane, 8 cm length gel,
1X TAE, 7 V/cm, 30 min

MassRuler Express Forward DNA Ladder Mix
(Thermo Fisher, Rockford)

2.2.2.6 Purification of DNA fragments

The extraction and purification of DNA fragments from agarose gels were performed using the QIAquick® Gel Extraction Kit from Qiagen according to the manufacturer's instructions. In short, the DNA fragments were excised from the agarose gel using a scalpel and dissolved in QG buffer which provides optimal pH and salt concentration for binding of DNA to a silica membrane. The samples were loaded onto the QIAquick® spin column and centrifuged. After two washing steps, the purified DNA fragments were finally eluted using 30 µl of elution buffer and stored at -20°C.

2.2.2.7 Restriction digest

The synthesized PCR products and the vectors were digested, using suitable restriction enzymes, to generate sticky ends for successful posterior ligation. Approximately 1 µg of plasmid DNA/purified PCR product was digested in compatible, commercial buffer using 2–10 U of restriction enzymes. For the vector pCGTO-PP-myc, the enzymes EcoRI and HindIII were used. The digests were incubated for 2 hours at 37°C and afterwards purified using the QIAquick® Gel Extraction Kit. The results of restriction digestion were evaluated by gel electrophoresis and UV illumination. Eventually, digest products were isolated from agarose gel slices and purified for further applications.

DNA digestion

Reagent	Volume
Template DNA (1 µg)	30 µl
10x CutSmart® buffer	5 µl
Restriction Enzyme I: EcoRI-HF	2 µl
Restriction Enzyme II: HindIII-HF	2 µl
dH$_2$O	up to 50 µl

2.2.2.8 Ligation of DNA fragments

2.2.2.8.1 Dephosphorylation of vectors

To increase the cloning efficiency and minimize vector recirculation, the 5'-phosphate ends of linearized vector pCGTO-PP-myc were enzymatically removed by the action of Antarctic Phosphatase. Dephosphorylation was performed with 1 µg vector DNA mixed with 2 µl Antarctic Phosphatase Reaction Buffer (10x) and 2 µl Antarctic Phosphatase in a total reaction volume of 20 µl at 37°C for 30 min. Afterwards, the enzyme was heat-inactivated at 80°C for 5 min. Finally, the vectors were purified using the QIAquick® Gel Extraction Kit and stored at -20°C.

Dephosphorylation of 5´-ends of DNA using Antarctic Phosphatase

Reagent	Volume
Template DNA (1 µg)	15 µl
10x Antarctic Phosphatase Buffer	2 µl
Antarctic Phosphatase	2 µl
dH$_2$O	up to 20 µl

2.2.2.8.2 Phosphorylation of DNA fragments

Phosphorylation with T4 PNK

Reagent	Volume
Template DNA (300 pmol)	30 µl
10x T4 PNK Reaction Buffer	5 µl
ATP (10 mM)	5 µl
T4 PNK	1 µl
dH$_2$O	up to 50 µl

The inserts were phosphorylated using T4 Polynucleotide Kinase (PNK) to allow the ligation of DNA fragments into the dephosphorylated vectors. The reaction was set up by using 300 pmol insert DNA mixed with 5 µl 10x T4 PNK Reaction Buffer, 5 µl ATP (10 mM) and 1 µl T4 PNK in a total volume of 50 µl. Then, samples were incubated at 37°C for 30 min followed by 65°C for 20 min. Finally, the PCR fragments were purified using the QIAquick® Gel Extraction Kit and stored at -20°C.

2.2.2.8.3 Ligation of inserts into vectors

The ligation of phosphorylated PCR fragments into dephosphorylated vectors was performed using T4 DNA-Ligase. To achieve a high ligation efficacy, the amount of insert and vector for the reaction was determined using the NEBioCalculator (http://nebiocalculator.neb.com/#!/ligation). A ligation using a molar ratio of 1:3 vector to insert yielded the greatest results (Wilcke, 2018). The reaction was incubated for 30 minutes at room temperature (RT) before being transformed into competent cells.

Ligation with T4 DNA Ligase

Reagent	Volume
10x T4 DNA Ligase Buffer	1 µl
Vector DNA	3.3 µl
Insert DNA	0.4 µl
T4 DNA Ligase	1 µl
dH$_2$O	up to 10 µl

2.2.2.9 Colony-PCR

Reaction components per colony-PCR

Reagent	Volume
2x Phusion High-Fidelity PCR Master Mix	10 µl
Forward Primer (10 µM)	1 µl
Reverse Primer (10 µM)	1 µl
Bacterial colony	1
dH$_2$O	up to 20 µl

After cloning, colony-PCR was employed to screen transformed bacteria for the presence of the proper insert DNA. Therefore, primers binding the new insert and the vector DNA

were employed, resulting in a PCR product being created only when the plasmid carrying the new insert was present within a colony. Individual *E. coli* transformants were picked with sterile pipet tips and added directly to the PCR reaction. The plasmid DNA was released from the cell during this initial heating step, allowing it to serve as a template for the amplification reaction. PCR amplicon and the size of the PCR product were determined by agarose gel electrophoresis.

Colony-PCR cycling steps

PCR step	Temperature	Time	Cycles
Initial denaturation	98°C	1 min	1
Denaturation	98°C	5 s	
Annealing	70→60°C	30 s	30
Elongation	72°C	2 min	
Final elongation	72°C	5 min	1
Final hold	12°C	∞	-

2.2.2.10 DNA-Sequencing

Purified plasmids were submitted for Sanger sequencing to ensure proper integration of the PCR fragment into the vector and to rule out insert mutations. Sequencing was performed by Eurofins Genomics (Ebersberg, Germany). Each sample was diluted to 75 ng/µl in a total volume of 15 µl including 10 µM specific primers. Eventually, common sequencing primers (CMVmin, pEGFPN1rev) that bind the vector in front of the insert offered by the company were used.

2.2.3 Cell culture methods

2.2.3.1 Subculture of adherent mammalian cell lines

As described in (Antoine et al., 2016; Jakobowska et al., 2021), the human embryonic kidney HEK293 cells were cultured in round 10 or 15 cm cell culture dishes in 10 or 15 ml of pre-warmed Dulbecco's Modified Eagle Medium (DMEM) with high glucose, supplemented with 10% (v/v) fetal bovine serum (FBS), 100 units/ml of penicillin and 100 µg/ml of streptomycin (Pen Strep). In order to achieve tetracycline-regulated expression of the gene of interest, the cell line was stably transfected with a TET-repressor encoding sequence sourced from the pcDNA™6/TR vector (Invitrogen, Waltham). To ensure the presence of the TET repressor, the cells were cultivated in a

medium supplemented with 5 μg/ml of blasticidin. The cells were cultured in a humidified incubator at 37°C and 5% CO_2 until they reached 80% confluency on each cell culture plate. The handling of the cells was performed in sterile conditions under a laminar flow clean bench. Cells were subcultured by removing the medium, washing with 10 ml DPBS and incubating them with 1 or 1.5 ml of 0.05% trypsin-EDTA at 37°C and 5% CO_2 for approximately 3 min until the cells were detached. Next, the cells were resuspended in a small volume of fresh serum-containing medium to inactivate the trypsin and seeded at an adequate cell density (Jakobowska et al., 2021).

2.2.3.2 Cell quantification

The Neubauer improved hemocytometer cell counting chamber was used to quantify the number of living cells. The adherent cells were brought into suspension using trypsin/EDTA and resuspended in a volume of fresh medium at least equivalent to the volume of trypsin. The chamber was filled (approx. 10 μl) with cell suspension and the total cell number was calculated under a light microscope using x20 magnification as follows. First, the cells in each of the four corner quarters were counted, and then the mean of the cell number was calculated by dividing the counted cells by the four quarters. One corner quarter represents the area of 1 mm^2 and the height of 0.1 mm. Thus, the cell number of one quarter represents 0.1 μl cell suspension. Finally, the mean was multiplied by 10^4 to estimate the number of cells per ml.

2.2.3.3 Cryopreservation and storage of cell lines

Cells were frozen to reduce loss due to contamination, minimize the genetic change in continuous cell lines, and avoid ageing and transformation in finite cell lines. First of all, cells were gently detached from the dishes using trypsin, centrifuged at 200 x g for 5 minutes at room temperature and the resulting cell pellet was resuspended in 90% (v/v) FBS and 10% (v/v) DMSO. Then the cells were transferred to an ice-cold cryotube and frozen stepwise: first, incubated on ice for a few minutes, then put inside a passive freezer Mr. Frosty™, filled with isopropyl alcohol, decreasing the temperature approximately 1°C per minute, and placed at -80°C. After 24–72 hours the cells were transferred to liquid nitrogen and stored at -190°C. For thawing of cells, 10 ml of pre-warmed medium (DMEM/10% FBS) was prepared in a 10 cm cell culture dish. Then, cells were thawed by incubating the cryotube for a short period in a 37°C water bath. Afterwards, the cells were seeded in a 10 cm dish.

2.2.3.4 Transfection of mammalian cells

The introduction of nucleic acids into eukaryotic cells is the so-called transfection (Chong et al., 2021; Fus-Kujawa et al., 2021; Kim & Eberwine, 2010). Transfection solves the problem of inserting negatively charged molecules (like DNA's phosphate backbones) into negatively charged cells. Transfection reagents are positively charged and attract negatively charged DNA, resulting in the formation of a positively charged polymer that can interact with the negatively charged cell membrane, allowing the polymer to enter the cell. The mammalian expression vector pCGTO, which is derived from pcDNA3.1 (Invitrogen, Waltham), was used to clone the full-length PfFNT DNA from *Plasmodium falciparum* 3D7 with a C-terminal GFP fusion. To generate cell lines stably expressing PfFNT-eGFP wt and G107S, the plasmid DNA was transfected into TET-inducible T-REx™-293 cells using jetPrime® transfection reagent from Polyplus according to the manufacturer's instructions. Protein expression was induced by the addition of 1 µg/ml tetracycline 20 h prior to cell harvest. Cells were selected with an antibiotic zeocin at a concentration of 100 µg/ml over several weeks to obtain monoclonal cell lines. Resistant cell lines were analyzed for high expression levels of the fusion protein using live-cell imaging and FCS. One clone with high PfFNT-eGFP expression was selected for the production of screening lysate.

Transfection components

Construct	Conc. [µg/µl]	Plate size	Number of cells seeded	DNA amount [µg]	DNA [µl]	Vol. of diluent [µl]	Jet-prime
pCGTO-PP-myc PfFNT wt	1.599	15 cm	4.5×10^6	8	5.0	483.0	12
pCGTO-PP-myc PfFNT wt	1.599	10 cm	2×10^6	4	2.5	241.5	6
pCGTO-PP-myc PfFNT wt	1.599	96 (4 wells)	1×10^5	0.5	0.3	48.7	1
pCGTO-PP-myc PfFNT G107S	1.509	15 cm	4.5×10^6	8	5.3	482.7	12
pCGTO-PP-myc PfFNT G107S	1.509	10 cm	2×10^6	4	2.6	241.4	6
pCGTO-PP-myc PfFNT G107S	1.509	96 (4 wells)	1×10^5	0.5	0.3	48.7	1

2.2.3.5 Lysate preparation

As described in (Antoine et al., 2016; Jakobowska et al., 2021), PfFNT-eGFP membrane preps were obtained by collecting cell pellets (approximately 2×10^7 cells per dish) of 15 cm dishes. During the harvest, the cells were washed twice with PBS, pelleted for 5 min at 1100 x g and then frozen at -80°C. Thawed cell pellets were resuspended in TBS supplemented with protease inhibitor cocktail (TBS-PIC) and broken by sonication on ice with 10 cycles (15 s sonication at 35 W; 15 s pause) using an ultrasonic homogenizer SONOPULS HD 2070. After that, the cell debris was separated by centrifugation for 5 minutes at 1100 x g at 4°C, and then the membranes were obtained from the cleared lysate by performing subsequent centrifugation at 21,000 x g. Supernatants were discarded and the resulting cell pellets were lysed using a Dounce homogenizer (tight pestle), aliquoted in 500 µl samples and frozen at -80°C. For FCS/FCCS measurement, membrane preps were solubilized in either 1% (w/v) LMNG in TBS-PIC or alternative detergents (DDM, DM, CHAPS, CHS, LDAO) when performing tests to identify the optimal solubilization conditions. After being incubated for one hour at 4°C on an end-over-end rotator, the samples were centrifuged for one hour at 21,000 x g at 4°C to remove the insolubilized membrane material. Supernatants containing the extracted proteins were transferred to new reaction tubes and stored at -80°C (Antoine et al., 2016; Jakobowska et al., 2021).

2.2.4 Protein biochemical methods

2.2.4.1 Western blot

2.2.4.1.1 SDS-Polyacrylamide electrophoresis (SDS-Page)

Composition of reagents used for preparing SDS gels

Separating gel (10% acrylamide)		Stacking gel (4% acrylamide)	
Component	Volume	Component	Volume
dH$_2$O	4.76 ml	dH$_2$O	4.33 ml
1.5 M Tris/HCl pH 8.8	3 ml	1 M Tris/HCl pH 6.8	0.75 ml
Bis-Acrylamide (30%)	4 ml	Bis-Acrylamide (30%)	0.8 ml
SDS (10%)	120 µl	SDS (10%)	60 µl
APS (10%)	120 µl	APS (10%)	60 µl
TEMED	12 µl	TEMED	6 µl

Proteins were size-separated using discontinuous sodium dodecyl sulfate–polyacrylamide gel electrophoresis (SDS-PAGE). The separation of proteins within the polyacrylamide gels, according to their molecular weight, occurs *via* voltage application. Because all peptides have a negative charge as a result of the SDS treatment, smaller molecules may migrate faster to the anode and therefore are separated from the bigger, i.e., longer protein chains. SDS gels were prepared in-house between two glass plates in a gel caster. First, a separation (resolving) gel (10% acrylamide) was cast into the mold and the gel solution was covered with 1 ml of 50% (v/v) isopropanol to prevent drying out. After polymerization (30 min at RT), the alcohol was removed and the stacking gel was cast onto the separation gel (4% acrylamide). Before polymerization, a comb with 12 wells was inserted to generate sample pockets. After 30 min polymerizing at room temperature, the comb was removed, and gels were used either directly or wrapped in wet paper towels and stored at 4°C. For denaturation, samples of the frozen lysates were mixed with 4x Laemmli buffer and incubated for 30 min at 37°C. The reducing agent dithiothreitol (DTT), contained in the buffer, leads to the reduction of disulfide bonds so that the proteins are present in an unfolded conformation. The separation was carried out in an agarose gel chamber filled with 1x SDS running buffer. The prepared samples (20 µl) were loaded together with a PageRuler™ Prestained Protein Ladder (10 µl) into the gel pockets and 80 V were applied till the samples had run through the stacking gel (approx. 15 min). At this point the voltage was increased to 120 V. Then the proteins were finally size-separated by migration in an electric field (60−90 min) and afterwards the gels were submitted to Western blot analysis.

PageRuler™ Prestained Protein Ladder
(Thermo Fisher, Rockford)
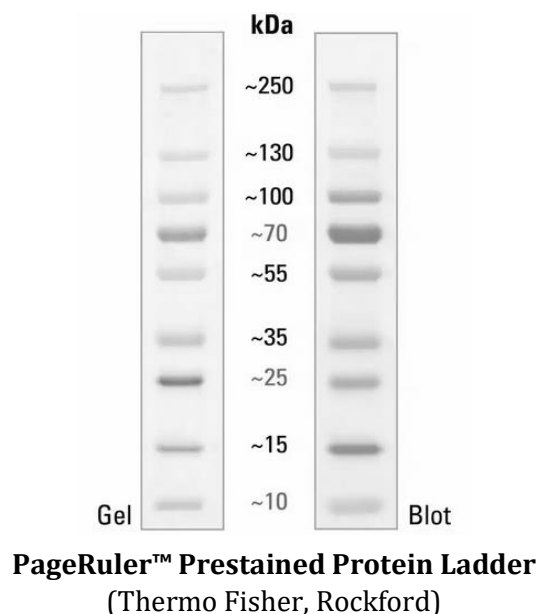
2.2.4.1.2 Ponceau S staining

The gels were usually reversibly stained with Ponceau S to visualize protein bands. Ponceau S is a negatively charged, red-coloured stain which binds to the positively charged functional groups of the protein (amino groups) and non-polar regions of proteins. For staining, gels were incubated for 5 min at RT in 0.1% (w/v) Ponceau S in 5% acetic acid. Afterwards, the gels were destained by repeated washing with H_2O until the background was reduced and the protein bands were clearly visible.

2.2.4.1.3 Western blot and development

For the specific detection of target proteins, the negatively charged proteins that were separated by SDS-PAGE were transferred to a nitrocellulose membrane by the wet transfer method. For this reason, the polyacrylamide gel was layered on a nitrocellulose membrane and sandwiched between 2 Whatman™ filter papers and 2 sponges which had been soaked in a transfer buffer solution. The blotting process was accomplished in a tank blotting chamber filled with blotting buffer, with the nitrocellulose facing the anode and the polyacrylamide gel facing the cathode. The transfer was run for 60 min at 250 mA. For an immune detection after protein transfer, the membrane was blocked by rolling for 1 h at RT in TBS containing 0.1% (v/v) Tween20 (TBS-T) and 5% (w/v) fat-free milk powder. After blocking, the membrane was probed with primary antibody for 1 h at RT under shaking, rinsed three times with 10−15 ml of TBS-T (5 min per rinse) and finally incubated with a horseradish peroxidase (HRP)-conjugated secondary antibody (1 h, RT, under shaking). All antibodies were diluted in 3% (w/v) milk powder in TBS-T (anti-GFP antibody, 1: 2000; goat anti-mouse, 1:10000). Next, the membranes were washed again with TBS-T (5 to 6 times, changing every 5 min) and coated with 1 ml of commercially available Amersham™ ECL Western blotting substrate (1:1). The luminescence was finally detected using the developing machine Curix 60. Exposition times were adjusted between 30 seconds and 15 minutes, dependent on the signal intensity.

2.2.4.2 Determination of protein concentration

The protein concentration determination was performed using the Pierce™ BCA Protein Assay Kit according to the manufacturer's instructions. The BCA assay primarily relies on two reactions. First, the reduction of Cu^{2+} ions from the copper (II) sulfate to Cu^{1+} by proteins in an alkaline medium (biuret reaction). The amount of Cu^{2+} reduced is proportional to the amount of protein present in the solution. Second, the chelation of

Cu[1+] by two molecules of bicinchoninic acid (BCA) that results in forming a purple-coloured complex that strongly absorbs light at a wavelength of 562 nm. By measuring the absorption spectra and comparing them to protein solutions with known concentrations, it is possible to determine how much protein is present in a solution. In short, the protein-containing samples were diluted and incubated with the Bio-Rad reagent for 30 minutes at 37°C. The absorbance of samples against the blank value (solubilization buffer instead of protein sample) was measured at 562 nm using a Biowave II spectrophotometer. The quantification of protein amount was based on a calibration curve of BSA standard solutions ranging from 0 to 2.0 mg/ml.

2.2.5 Synthesis of BH296 and BH267.meta with a 3-aminopropoxy linker

The description of the synthesis is taken from the publication (Jakobowska et al., 2021). "The compounds BH296 (4,4,5,5,5-pentafluoro-3-hydroxy-1-(4-hydroxyphenyl)pent-2-en-1-one) and BH267.meta carrying a hydroxyl moiety at the pyridine (4,4,5,5,5-pentafluoro-3-hydroxy-1-(6-hydroxypyridin-3-yl)pent-2-en-1-one) for attachment of the 3-aminopropoxy linker were synthesized by Björn Henke (Christian-Albrechts-University of Kiel, Germany) as described before by a Claisen-type condensation in anhydrous THF using lithium hydride as a base (Golldack et al., 2017; Walloch et al., 2020). Generally, for structure analysis and purity assessment (>95% of all compounds), mass spectrometry (LC-MS; Bruker Amazon SL) and nuclear magnetic resonance (Bruker Avance III 300) were employed. A total of 1.13 g (4 mmol) of BH296 and 2.61 g (8 mmol) of cesium carbonate were suspended in 10 ml of N, N-dimethylformamide, stirred for 30 min at room temperature upon addition of 3-(Boc-amino)propyl bromide dissolved in 5 ml of N,N-dimethylformamide. The reaction was kept stirring for 16 h, before it was filtered, 1 ml of concentrated acidic acid was added to the filtrate, and the solvent was evaporated off. Silica gel chromatography with cyclohexane/ethyl acetate (8:2) as the mobile phase yielded 77% of the desired product ($C_{19}H_{22}F_5NO_5$; 439.38 g mol^{-1}).

^{1}H-NMR (300 MHz, 25°C, [d$_6$]-DMSO):
δ/ppm = 1.38 (s, 9H, O-C(CH$_3$)$_3$); 1.83–1.90 (m, 2H, -CH$_2$); 3.07–3.12 (m, 2H, -CH$_2$); 4.10–4.13 (t, ^{3}J = 6.3 Hz, 2H, -CH$_2$); 6.92–6.95 (m, 1H); 7.00 (s, 1H); 7.10 (d, ^{3}J = 9.0 Hz, 2H); 8.16 (d, ^{3}J = 9.0 Hz, 2H).

The protective Boc group was removed by dissolving 1.36 g of product in 4 ml of dichloromethane, dropwise addition of 4 ml of trifluoro acetic acid, and stirring at room

temperature for 5 h. The solvent was evaporated off, yielding 95% of the product ($C_{18}H_{21}F_5N_2O_5$; 440.37g mol^{-1}).

^{1}H-NMR (300 MHz, 25°C, [d$_6$]-DMSO):

δ/ppm = 1.37 (s, 9H, O-C(CH$_3$)$_3$); 1.75–1.81 (m, 2H, -CH$_2$); 2.94–2.99 (m, 2H, -CH$_2$); 3.96–3.99 (t, ^{3}J = 7.0 Hz, 2H, -CH$_2$); 6.52 (d, ^{3}J = 9.8 Hz 1H); 6.93 (t, ^{3}J = 6.9 Hz 1H); 6.98 (s, 1H); 7.99 (dd, 1H); 8.98 (d, ^{3}J = 2.5 Hz 1H).

BH267.meta carrying a 3-aminopropoxy linker was synthesized using the same procedure, starting from 0.3 g of 4,4,5,5,5-pentafluoro-3-hydroxy-1-(6-hydroxypyridin-3-yl)pent-2-en-1-one to yield 64% of the Boc-protected product ($C_{18}H_{21}F_5N_2O_5$; 440.37g mol^{-1}).

^{1}H-NMR (300 MHz, 25°C, [d$_6$]-DMSO):

δ/ppm = 1.37 (s, 9H, O-C(CH$_3$)$_3$); 1.75–1.81 (m, 2H, -CH$_2$); 2.94–2.99 (m, 2H, -CH$_2$); 3.96-3.99 (t, ^{3}J = 7.0 Hz, 2H, -CH$_2$); 6.52 (d, ^{3}J = 9.8 Hz 1H); 6.93 (t, ^{3}J = 6.9 Hz 1H); 6.98 (s, 1H); 7.99 (dd, 1H); 8.98 (d, ^{3}J = 2.5 Hz 1H).

Removal of the Boc group by trifluoro acetic acid treatment yielded 87% of BH267.meta carrying a 3-aminopropoxy linker ($C_{16}H_{15}F_8NO_5$; 454.27 g mol^{-1}).

^{1}H-NMR (300 MHz, 25°C, [d$_6$]-DMSO):

δ/ppm = 1.95–2.03 (m, 2H, -CH$_2$); 2.78–2.86 (m, 2H, -CH$_2$); 4.07 (t, ^{3}J = 6.9 Hz, 2H, -CH$_2$); 6.55 (d, ^{3}J = 9.7 Hz 1H); 6.95 (s, 1H); 7.84 (s,3H, -NH$_3$); 8.03 (dd, 1H) ; 8.98 (d, ^{3}J = 2.5 Hz 1H)" (Jakobowska et al., 2021).

2.2.5.1 Fluorescent labelling of the tracer molecules

As described in (Jakobowska et al., 2021), the compounds, BH296 and BH267.meta, were resuspended in DMSO to a final concentration of 50 nM. Then, 4 µl (200 nmol) of these compounds were dissolved in 95.3 µl of DMSO + 0.7 µl of DIPEA and labelled *via* the amino group to DY647-Peg4 (0.2 mg, 200 nmol) utilizing a reactive NHS ester group and generating a chemically stable amide bond. For labelling, the reaction mixture was incubated in the dark at room temperature for 2 h. The unconjugated dye was separated from the labelled protein on a reversed-phase high-performance liquid chromatography (HPLC) using an ACN/H$_2$O gradient from 20% to 80% ACN (BH296) or 40% to 60% ACN (BH267.meta). Then, the labelled compounds were lyophilized, dissolved in DMSO, and stored at -20°C (Antoine et al., 2016). The detection wavelength was set at 223 nm as proteins absorb UV light at this wavelength due to the presence of double bonds within

amino acid carbonyl groups (Lewis et al., 2010). The signal at the reference wavelength of 360 nm was employed as an internal reference to adjust the spectrum of the test sample based on the displacement effect between solvent and solute molecules in a solution (Jakobowska et al., 2021).

2.2.6 Live-cell imaging

Cells were seeded in 96-well plates with clear bottom, grown in complete medium and transfected. For imaging, the medium was replaced with 0.05% Triton X-100 in PBS and labelled ligands. For competition experiments, unlabelled competitors were first incubated with labelled ligands for 5 min at room temperature before the mix was added to cells (Antoine et al., 2016). The confocal laser scanning microscopy was performed on a Zeiss LSM 510 confocal microscope connected to an Axiovert 200M equipped with a C-Apochromat 40×/1.2 W water immersion objective (Antoine et al., 2016; Jakobowska et al., 2021). A 633 nm helium-neon laser was used to excite the red fluorophore (DY647), whereas a 488 nm argon-ion laser was used to excite the green fluorophore (GFP) (Antoine et al., 2016; Jakobowska et al., 2021). The concentration of the labelled interactors was calculated from the knowledge of the particle numbers in the detection volume, derived from the amplitudes of the autocorrelation functions and the spatial expansion of the two detection volumes with reference to the manufacturer's specifications. According to the information from Zeiss (Jena, Germany), with ideal focusing and pinhole opening on 1 Airy unit, 1 particle in the 488 nm channel corresponds to a concentration of 4 nM and in the 633 nm channel to 2 nM.

2.2.7 FCCS measurements

FCCS measurements were performed in lysate samples of a volume of 20 or 30 µl in 384-well glass-bottom plates using an Evotec Insight plate reader equipped with a U-Apo300 40x water immersion lens, NA 1.15 (Jakobowska et al., 2021). The system uses a 633-nm helium-neon laser for the excitation of DY647 dye and the 488-nm laser line of an argon-ion laser to excite the enhanced GFP (Antoine et al., 2016; Jakobowska et al., 2021). The measurements were executed at the equilibrium of the interaction which was obtained after 60 min incubation at room temperature. Fluorescence fluctuations were recorded for 8 s with 12 repetitions and afterwards, the fitting of the autocorrelation functions and data analysis were carried out using the Evotec FCS+ plus software package (Antoine et al., 2016; Jakobowska et al., 2021).

2.2.7.1 Titration experiments

To analyze the binding of a labelled molecule by autocorrelation it is necessary to determine the diffusion time of the unbound labelled ligand in a reference measurement. For this purpose, autocorrelation curves of cellular lysate containing the protein of interest-GFP and of compound-DY647 were recorded and fitted to the 1-component-model. Subsequently, the labelled compound was added to lysate expressing the GFP-fusion of the target of interest. Lysates were diluted to approximate particle numbers between 0.5 and 2, which correspond to concentrations between 5 nM and 20 nM and aliquots of 20 µl were distributed into the wells of the 384-well microtiter plate. The labelled compound was added with the highest concentration into the first well and serial dilution steps were performed to cover a concentration range between 200 nM and 1 nM. Measurements were carried out and resulting cross-correlating particle numbers were plotted against the concentration of the labelled ligand. The fitting of autocorrelation and cross-correlation functions were performed by applying a 1-component fit for the green channel and a 2-component fit for the red channel (fixing "free" diffusion time to 139 µs). The dissociation constant (K_D value) was calculated using a two-state single-site binding model (Antoine et al., 2016; Jakobowska et al., 2021).

$$C = \frac{R_T L_F}{K_D + L_F}$$

where C is concentration of receptor-fluorescent probe complexes calculated from the number of cross-correlating particles, R_T is concentration of total active receptor and L_F is concentration of free labelled fluorescent probe derived from autocorrelation function for DY647 signal (Antoine et al., 2016).

2.2.7.2 Competition experiments

Competition studies, in which the labelled ligand is displaced from its target by the competitor, were conducted to measure the affinities of unlabelled molecules. In the first step of competition experiments, a labelled compound is added to lysate expressing the GFP-fusion of the target of interest. Therefore, the lysate was diluted to approximate particle numbers between 0.5 and 2 (corresponding to concentrations between 5 nM and 20 nM) and mixed with labelled compound at the optimal concentration as determined in titration experiments. The lysates premixed with compound-DY647 were distributed in 30 µl volumes into 384-well glass bottom plate cavities. Next, a titration series of 12 dilutions for the unlabelled competitor was prepared and added to each well. After

incubation for 1 h, while shaking at room temperature, the measurements were carried out and fitted to an appropriate model. The *IC50* values were determined by plotting the concentration from the dual-labelled complex against the concentration of the competitor titrated over a concentration range from 10 µM to 10 pM. From the resulting *IC50* values, the K_i values were acquired by application of the Cheng-Prusoff equation (Antoine et al., 2016; Cheng & Prusoff, 1973; Jakobowska et al., 2021).

$$K_i = \frac{IC_{50}}{1 + \frac{[L]}{K_D}}$$

where $[L]$ is the concentration of labelled ligand, K_i is the inhibition constant, defined as the equilibrium concentration of competitive inhibitor that would occupy 50% of receptor sites if no competing labelled ligand was present, IC_{50} is the concentration at which the competitive inhibitor displaces 50% of the specifically bound labelled ligand, and K_D is the affinity constant, defined as the equilibrium concentration of labelled ligand that occupies 50% of receptor sites in the absence of competition (Cheng & Prusoff, 1973).

2.2.7.3 Kinetics measurements

Compounds with equal affinities but varying kinetics respond differently in physiological environments, hence rate constants are just as essential to investigate as affinities. Rate constants describe the dynamics by which molecular interactions form and complexes fall apart. To assess the rate constants, time-resolved measurements were carried out at different concentrations of labelled ligand (Antoine et al., 2016). During the kinetics monitoring using FCCS, single measurements were taken for 5-20 seconds depending on the rate of complex formation, over a period of 5-15 minutes (Antoine et al., 2016). Then, the resulting measurement curves were fitted to a function, from which it was possible to retrieve the k_{obs} values. Rate constants (k_{on} and k_{off}) were obtained from the plot of the k_{obs} values against the concentration of total labelled ligand (L_T) by applying a linear equation (Antoine et al., 2016; Hoare, 2004):

$$k_{obs} = L_T k_{on} + k_{off}$$

The k_{obs} values resulted in a straight line, the slope of which is the k_{on} value and the y-intercept the k_{off} value (Antoine et al., 2016; Jakobowska et al., 2021).

2.2.7.4 Screening

Hits from compound inhibitor libraries were identified using a biophysical affinity-based screening method. Biophysical assays search for compounds that displace a labelled

tracer molecule from a molecular target by competition. The assay has been developed by expressing a selected GFP-fusion target protein and lysing cells. When the DY647-labelled compound was added to the lysate at nanomolar concentrations, it bound to the target protein, forming a dual labelled complex. In the case of finding a positive hit, the interaction with the labelled compound was competed, and the loss of the FCCS signal indicated a displacement of the tracer from the target.

2.2.8 Intracellular pH detection

Intracellular pH was determined with pHrodo™ Red AM, a novel fluorogenic probe, according to the manufacturer's instructions (Benjamin et al., 2018). pHrodo™ Red AM is weakly fluorescent at neutral pH but increasingly fluorescent as the pH drops. HEK293 cells grown in DMEM (FBS 10%) were seeded in 96-well plates (100,000 cells/ml). After 24 hours cells were treated with drugs: 10 µM Syrosingopine/0.1 µM AZD3965 (MCT1 and MCT4 inhibitor) and 10 µM BH296 (PfFNT inhibitor) for 3 hours at 37°C. After drug treatment, cells were rinsed with HBSS, HEPES 20 mM and stained with pHrodo™ Red AM dye for 30 minutes (Benjamin et al., 2018). After washing with HBSS, HEPES 20 mM, cell fluorescence was measured (560/585 Ex/Em) (Benjamin et al., 2018).

2.2.9 Live-death assay

HEK293 cells grown in DMEM (FBS 10%) were seeded in 96-well plates (1000 cells/well) in a volume of 100 µl and treated with 10 µM Syrosingopine/0.1 µM AZD3965, 4 mM Metformin. During the screening of potential PfFNT inhibitors, test compounds were also added. The cells were subsequently exposed to the medications for 5 days at 37°C in a humidified incubator with 5% CO_2, and images were acquired using a Zeiss Axio Vert.A1 light microscope (10x magnification) at 0 h, 24 h, 48 h, and 120 h to assess cell survival.

3 Results

Part of the results presented here are published:

3.1 Preparation of fluorescent probes and their characterization by live-cell imaging

3.1.1 Cloning and protein expression of PfFNT in HEK293 cells

To generate a HEK293 cell line that stably expresses *Plasmodium falciparum* formate-nitrite transporter (PfFNT), the open reading frame (ORF) was extracted from pIVEX2.3 by double digestion with the restriction enzymes EcoRI, HindIII and subcloned into a pCGTO-PP-myc inducible expression vector containing C-terminal eGFP (see section 2.2.2) (Figure 3.1). By using enhanced GFP as a fluorescent tag, it was guaranteed that there was a minimal spectral overlap with fluorescence emission from the labelled probes (Antoine et al., 2016). The GFP was positioned at the C-terminus of the protein to avoid masking of the signal sequence at the N-terminus, which can lead to incorrect localization (Palmer & Freeman, 2004).
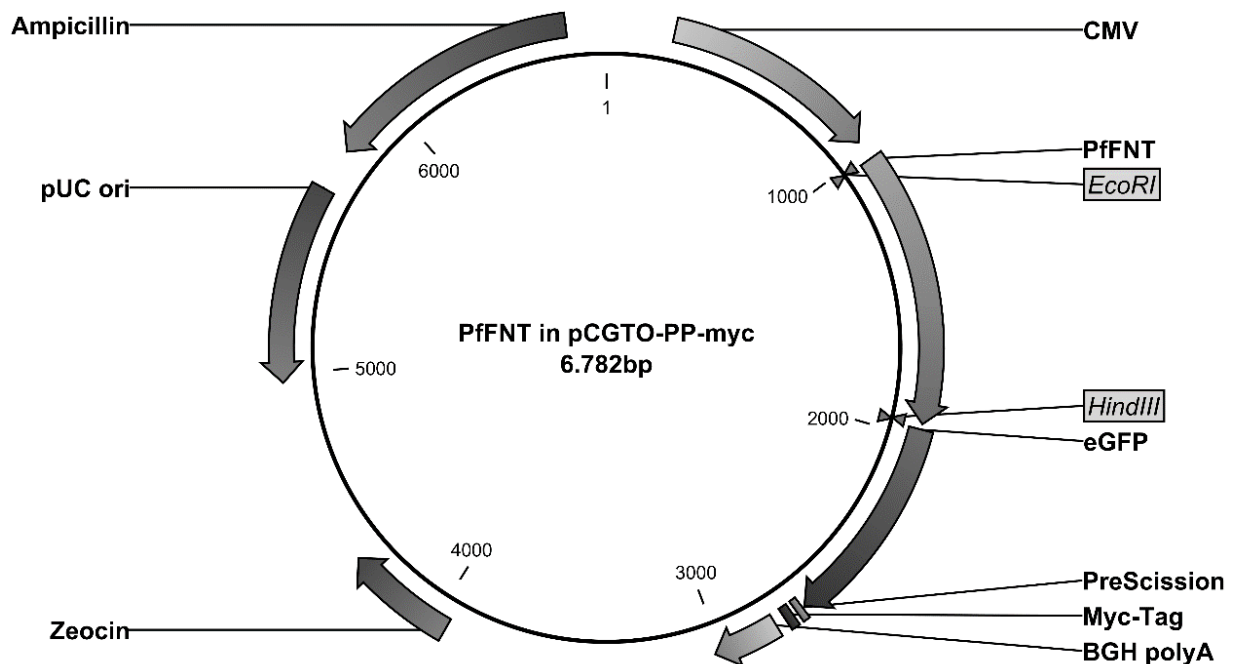
Figure 3.1 PfFNT-pCGTO-PP-myc eGFP fusion plasmid. Components of the vector: an origin of replication (pUC ori), a selectable marker (Ampicillin), a multicloning site (EcoRI, HindIII), a promoter region (CMV), a gene for eGFP-tag, and a PfFNT gene.

The successful uptake of the fusion plasmids, when checked for inserts with colony PCR, is illustrated in Figure 3.2A. To confirm the correct insert integration, control digestion was performed, showing a DNA fragment of the desired size - 936 bp (3.2B). Moreover, the correct sequence was confirmed by sequencing. The expression level and localization of PfFNT were examined by immunoblotting and confocal microscopy after induction of protein expression with tetracycline (Figures 3.3 and 3.4). Previous studies have shown that PfFNT localization in the plasma membrane correlates well with a proper folding, translocation, and activity (Antoine et al., 2016; Marchetti et al., 2015; Wu et al., 2015). Thus, clones with an appropriate expression at the cellular membrane of HEK293 cells were selected for clonal selection and expanded. The correct functionality of expressed PfFNT-eGFP fusions was checked by observation of their internalization upon agonist binding (as described in chapter 3.1.3).
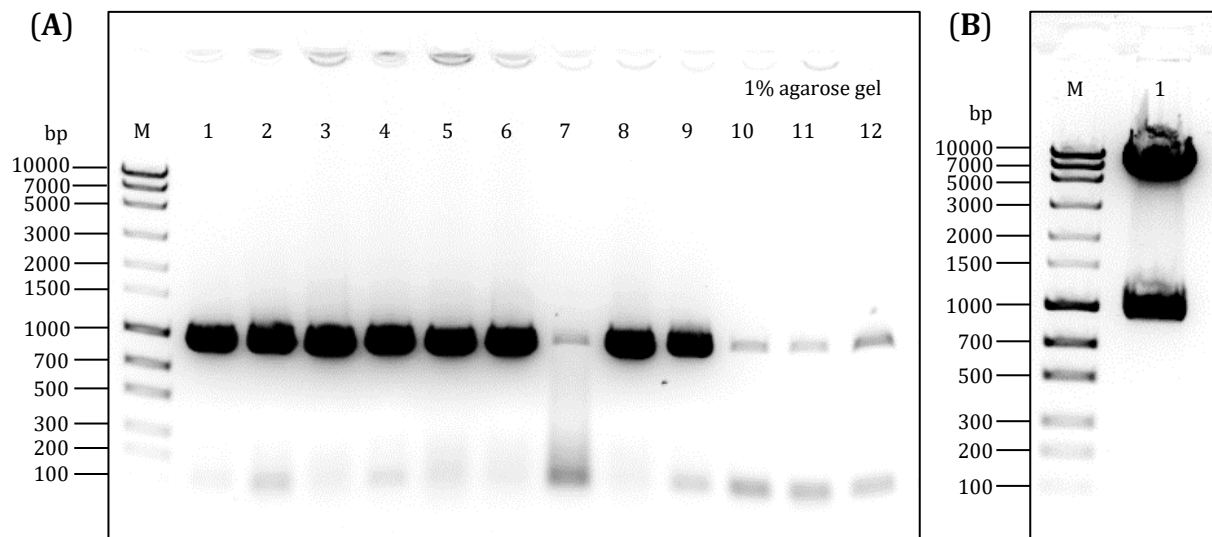
Figure 3.2 Documentation of the individual cloning steps illustrated by the corresponding agarose gels. MassRuler Express Forward DNA Ladder Mix was used as a size marker (M). (**A**) Colony PCR for PfFNT-pCGTO-PP-myc. All colonies (1-12) showed an amplification of the desired 963 bp DNA fragment. (**B**) Control digestion of Midiprep from clone #1. As a result of the successful double digestion of the plasmid with the restriction enzymes EcoRI and HindIII two bands can be observed. Of interest is the band at about 1000 bp as it corresponds to the mass of the DNA coding for PfFNT (936 bp).

To demonstrate the production of the PfFNT in HEK293 cells, the lysates were collected 16 hours after induction with tetracycline and analyzed by Western blotting using an antibody directed against eGFP-tag, as described in more detail in chapter 2.2.4.1. The calculated PfFNT size including eGFP is 61 kDa (PfFNT 34 kDa and GFP 27 kDa). The protein size on the Western blot consistently appeared smaller than theoretically calculated, see Figure 3.4. It has been previously shown that membrane protein migration

in SDS-PAGE gels does not precisely correlate with the predicted molecular weight due to the incomplete denaturation with SDS in the hydrophobic regions, especially in the transmembrane spans (Rath et al., 2009). Moreover, a similar effect for PfFNT was observed by Prof. Beitz and co-workers. Therefore, it is likely that the prominent band of 50 kDa corresponds to full-length PfFNT protein fused to eGFP. In addition to the monomer, bands of SDS-resistant oligomers (dimer – 60 kDa and pentamer – above 250 kDa) are visible, indicating correct protein folding.
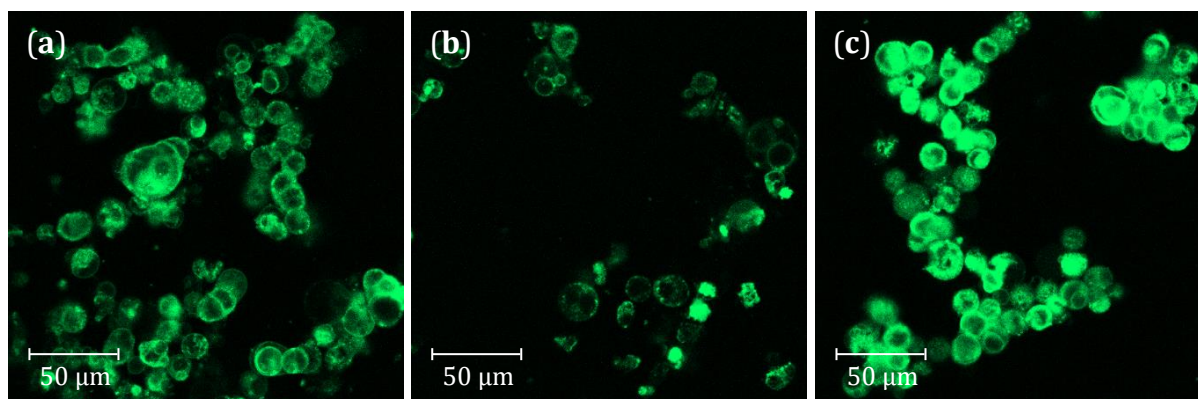
Figure 3.3 Monoclonal cell selection. Fluorescence microscopic images of three isolated monoclonal cell subpopulations of the PfFNT-GFP fusion protein. The clone on the left has been recognized as the best-performing and was selected for further propagation. The majority of the GFP signal was detected in the plasma membrane, with only a minor population of the receptor fusions localized in internal cellular compartments such as the endoplasmic reticulum, Golgi apparatus, and endosomes (Antoine et al., 2016; Jakobowska et al., 2021; Marchetti et al., 2015; Wu et al., 2015).
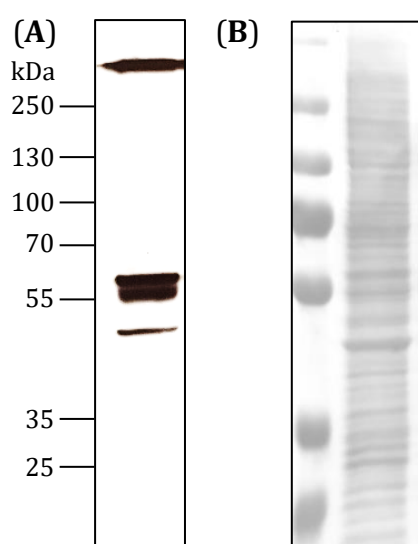
Figure 3.4 Western blot of PfFNT-GFP obtained from HEK293 cells. The incubation prior to SDS-PAGE was carried out at 37°C for 30 min. 30 µg of total protein was applied per lane. (**A**) The bands of the monomer (50 kDa), dimer (60 kDa) and pentamer (above 250 kDa) can be seen. A monoclonal anti-GPF antibody was used as the primary antibody. Exposure time: 30 seconds. (**B**) Quality control of membrane transfer by Ponceau staining.

3.1.2   Synthesis of DY647-labelled BH296 and BH267.meta

To generate probes for imaging and spectroscopy, PfFNT inhibitors (BH296 and BH267.meta) were functionalized with a 3-aminopropoxy moiety and labelled with the far-red fluorophore DY647. With an emission in the spectral range above 650 nm, the fluorescence of DY647 shows only a minimal spectral overlap with the emission of the eGFP (Antoine et al., 2016; Southwick et al., 1990). Compounds were fused with the dye *via* a flexible, hydrophilic polyethylene glycol (PEG) linker to avoid any impact of the fluorophore on drug-target interactions. Moreover, because of its hydrophilicity, the PEG spacer should promote the solubility of the compounds and minimize hydrophobic interactions with membranes and proteins (Glauner et al., 2010).
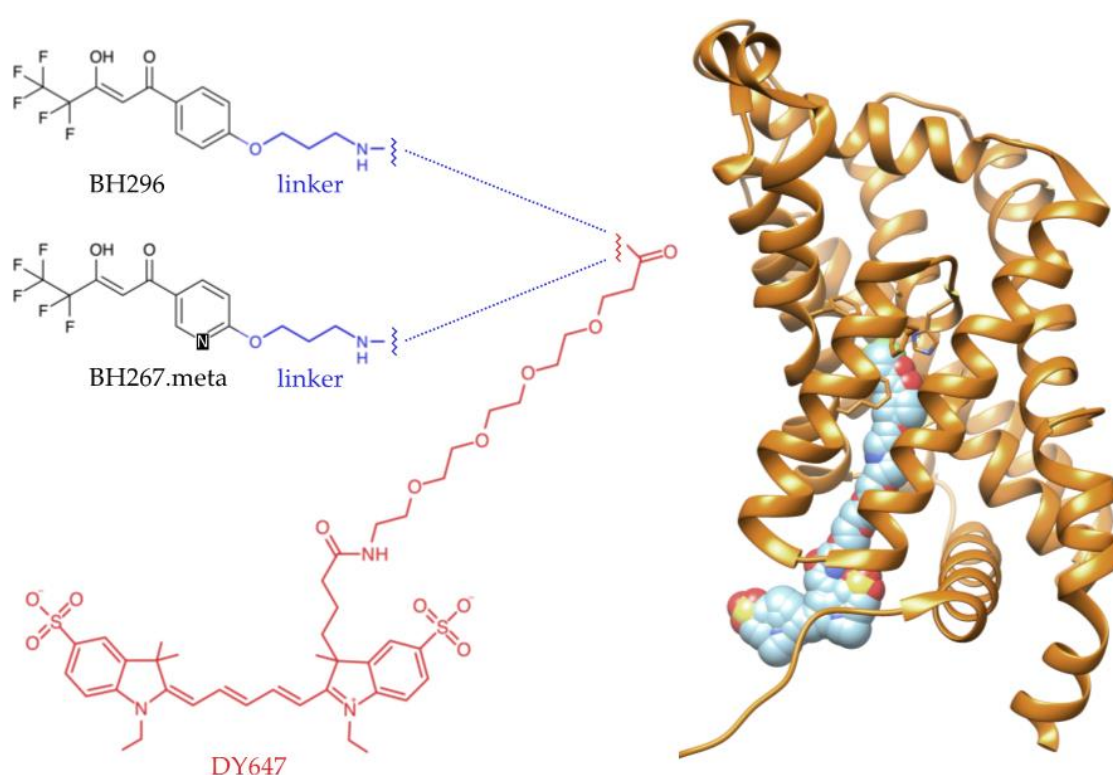
Figure 3.5 Inhibitors of PfFNT (BH296, BH267.meta) fused with a fluorescence label (DY647) *via* a 3-aminopropoxy linker. The presence of a 4x ethylene glycol unit in the label is responsible for preventing the fluorescent moiety from colliding with the protein target (Jakobowska et al., 2021). A model of PfFNT (PDB# 6vqr) with a bound inhibitor carrying the label is displayed in the right panel (Jakobowska et al., 2021). The figure is reprinted from (Jakobowska et al., 2021).

The unbound dye was separated from the labelled protein on a reversed-phase high-performance liquid chromatography (HPLC), using a mobile phase which was composed of 80% of deionized water and 20% of acetonitrile (BH296), or 60% of deionized water and 40% of acetonitrile (BH267.meta), see Chapter 2.2.5.1 for additional information. In the first step, an analytical run was performed only for the compounds in order to identify

their elution peak. The total run time was 12.30 min and peaks occurred at 8.30 min for BH296 and 6.45 min for BH267.meta. The differences in retention times were caused by the varied ACN/H$_2$O gradients used, but also by the presence of a polar pyridine in the structure of BH267.meta (Scriven & Murugan, 2005).
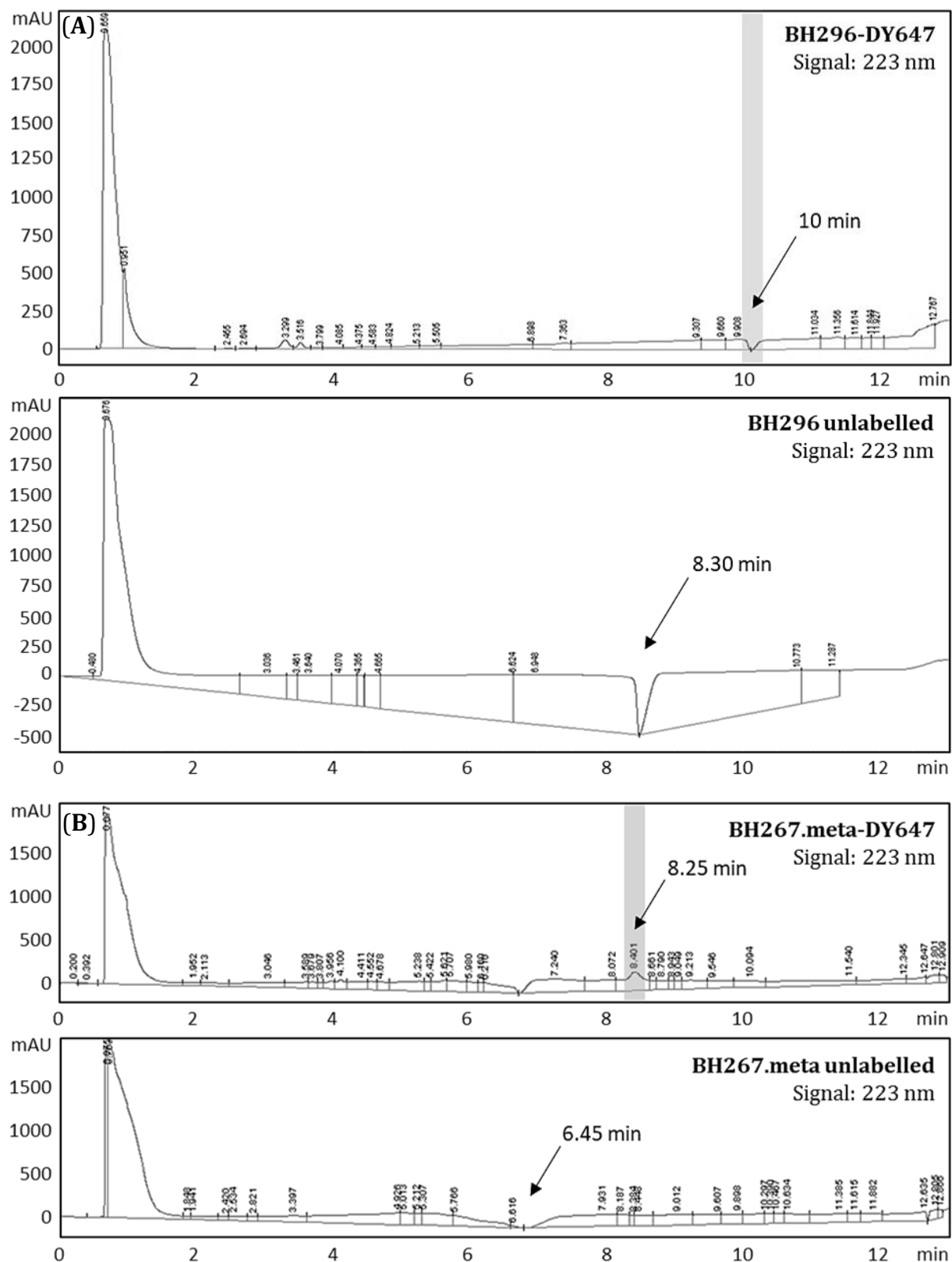
Figure 3.6 HPLC chromatogram. Fractions collected during separation are marked in grey. The retention time of unbound BH296 and BH297.meta is 8.30 min and 6.45 min, respectively. The retention time for BH296-DY647 is around 10 min and for BH267.meta-DY647 8.25 min. The initial high-intensity peak is a solvent peak. Small peaks occurring at 3-5 minutes are representing the free dye. Conditions: wavelength = 223 nm, temperature 25±2°C, mobile phase (**A**) ACN/H$_2$O 20:80; v/v, (**B**) ACN/H$_2$O 40:60; v/v, flow rate 1 ml/min.

Next, the samples containing mixtures of inhibitor-dye were injected into a column, yielding multiple elution peaks, one coming from the labelled peptide and others from the free dye. Inhibitor-containing fractions conjugated to DY647 were collected, lyophilized, dissolved in DMSO, and subjected to functional tests (as described in the next chapter). The output of an HPLC run is presented as a chromatogram, see Figure 3.6. The number of absorbance units (AU) is shown on the Y-axis while the time of the run is shown on the X-axis. It may be surprising that the peaks obtained during an HPLC run have a negative shape. However, negative peaks with refractive index detection (RID) are relatively common as a difference in reading is measured (Agilent Technologies, 2004). The main reason for the occurrence of the negative peaks in a chromatogram is that the refractive index of the solute is less than that of the mobile phase.

3.1.3   Intracellular binding of BH296-DY647 to PfFNT-GFP

The results described in this chapter have been published as (Jakobowska et al., 2021). To examine the binding capability of ligands to PfFNT, cultured HEK293 cells stably expressing PfFNT-GFP were treated with BH296-DY647 at a concentration of 50 nM. Confocal laser scanning microscopy (CLSM) was utilized to test for co-localization of the compound with the target at the plasma membrane. However, even after a 1-hour incubation, no binding of labelled BH296 could be seen (Figure 3.7A). As the compound was unable to access the cytoplasmic domain of the transporter, the next step was to find a way to permeabilize the plasma membrane while preserving cell viability during the incubation period. In order to facilitate the diffusion of BH296-DY647 into the cell, Triton X-100 at a final concentration of 0.05% was used, as previously described (Koley & Bard, 2010). After 30 seconds of incubation in the presence of Triton X-100, membrane localization of BH296-DY647 was clearly visible, and the intensity of staining increased within 5 minutes (Figure 3.7B, C). Strong overlap between the GFP and DY-647 signals at the plasma membrane revealed that both, the receptor and the fluorescent probe are functional (Antoine et al., 2016). A prolonged incubation (> 5 min) was hindered by incipient cell disintegration and membrane blebbing attributed to the harmful effect of

detergents on cellular viability. Thus, incubation with fluorescent tracers is feasible only for a short time frame, and capturing interactions of inhibitors with slower rates through imaging approach is challenging.
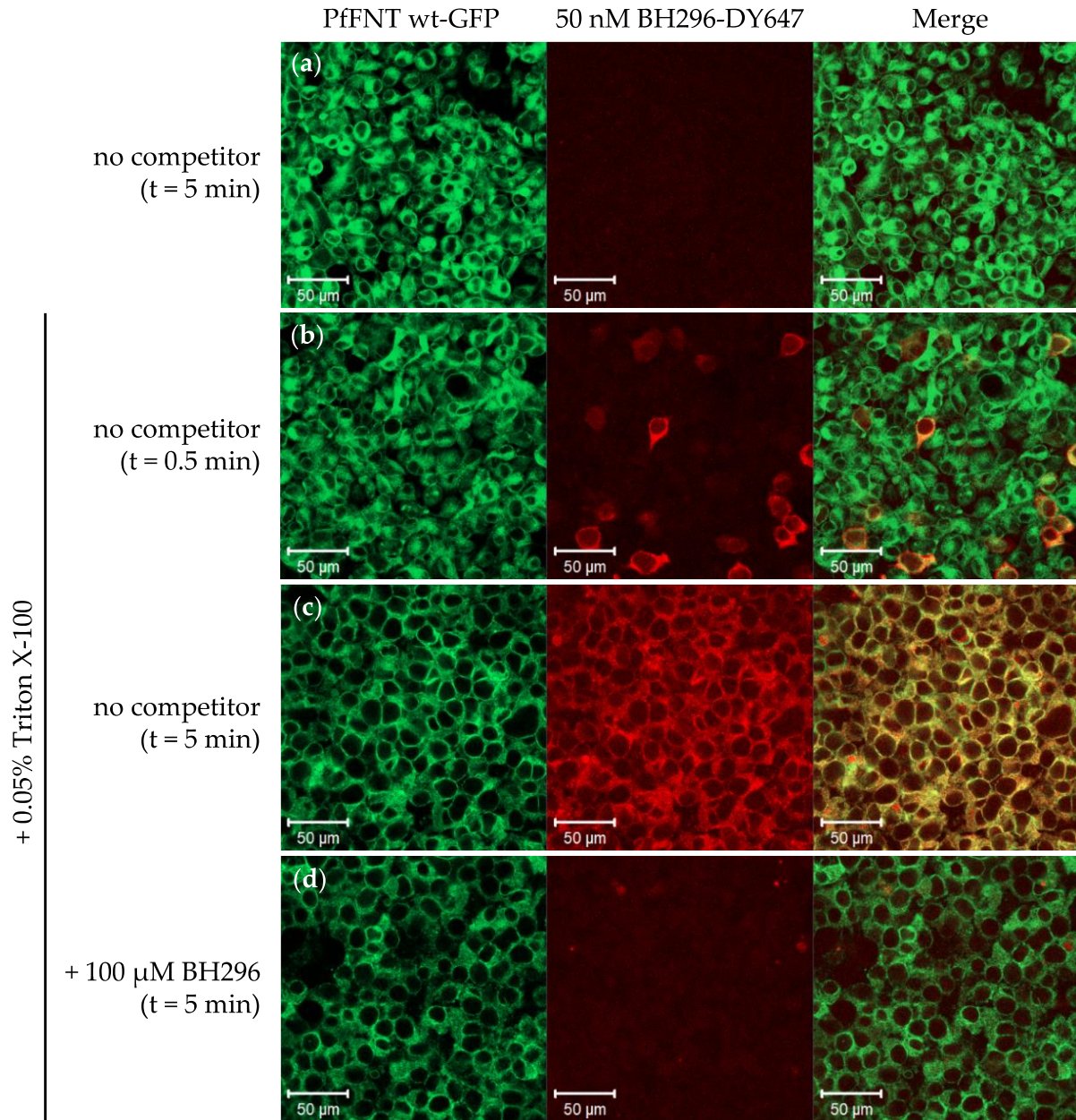

Figure 3.7 Live cell imaging of PfFNT-GFP stably expressed in human embryonic kidney 293 cells and binding of BH296-DY647. The left panels display images of PfFNT-GFP fusions (in green), while the middle panels show BH296-DY647 (in red). (**A**) When Triton X-100 (nonionic surfactant) was absent, there was no co-localization observed between PfFNT-GFP and BH296-DY647. However, after membrane permeabilization by treating cells with 0.05% Triton X-100, co-localization was evident. After 30 seconds of incubation (**B**, merged images, co-localization in yellow, right panels), membrane localization of BH296-DY647 was clearly visible and increased over time (**C**, incubation time 5 minutes). (**D**) Pre-incubation with 100 μM of unlabelled BH296 prevented binding of the labelled tracer, indicating that co-localization is mediated by interaction with PfFNT-GFP (Jakobowska et al., 2021). The figure is reprinted from (Jakobowska et al., 2021).

Next, the interaction of labelled BH296 with its unlabelled parental compound was tested to determine the specificity of binding. As shown in Figure 3.7D, pre-incubation of cells with an excess of 100 µM of BH296 completely abolished the binding of the labelled inhibitor. The cell surface staining with the fluorescent probes was highly target-specific, and it was entirely suppressed in the presence of a receptor-specific competitor. To further verify the specificity of the binding, BH296-DY647 was added to the monocarboxylate transporter hsMCT4, which is a human functional homologue of PfFNT but both proteins show no similarity on basis of their primary sequence or transport mechanism (Wu et al., 2015). Analogous to PfFNT, hsMCT4 was expressed as GFP fusion in HEK293 cells, but co-incubation with BH296-DY647 did not show any co-localization on the plasma membrane, confirming the selectivity of the ligand (Figure 3.8). Taken together, these findings demonstrate that BH296 binds specifically and irreversibly to the cytoplasmic domain of PfFNT in living cells, GFP-fused PfFNT and BH296-DY647 are functional and hence can be applied in FCCS (Jakobowska et al., 2021).
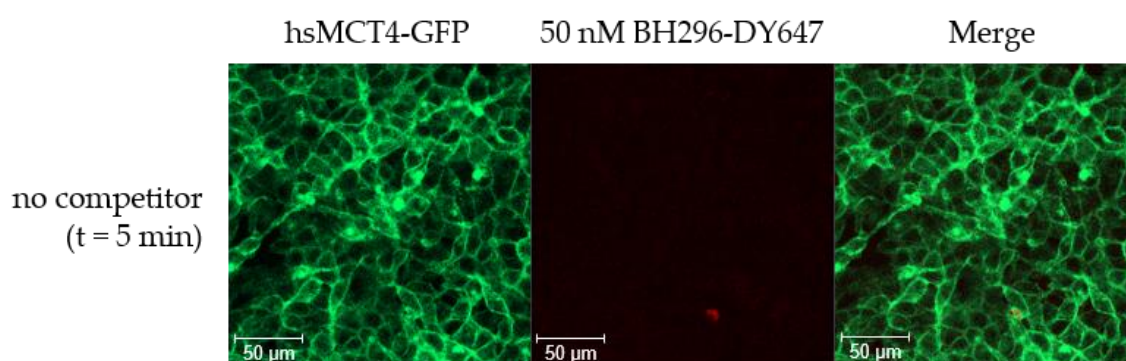
Figure 3.8 Specificity of BH296-DY647 for PfFNT. Live cell imaging of hsMCT4-GFP stably expressed in HEK293 (left) cells and co-incubation with BH296-DY647 (middle). No co-localization was observed (right) (Jakobowska et al., 2021). The figure is reprinted from (Jakobowska et al., 2021).

3.1.4 PfFNT Gly107Ser resistance mutation

Parasites treated with sub-lethal concentrations of BH296 developed a PfFNT Gly107Ser resistance mutation, which drastically reduced the inhibitor's affinity, but the introduction of a scaffold nitrogen atom (BH267.meta) restored the effectiveness of the inhibitor (Jakobowska et al., 2021; Walloch et al., 2020). The G107S mutation site is positioned at the cytoplasmic entrance of PfFNT and narrows the transport path, preventing BH296 binding by the sterical hindrance of the compound's phenyl moiety (Jakobowska et al., 2021). In order to restore binding to the mutant PfFNT G107S, BH296 was modified by introducing a nitrogen atom in the *meta*-position of its aromatic ring,

thus creating a hydrogen bond acceptor site for the serine hydroxyl of the resistance mutation (Jakobowska et al., 2021; Peng et al., 2021; Walloch et al., 2020). The interaction of BH267.meta was analyzed through cellular imaging (Chapter 3.1.5). For this purpose, DY647-labelled BH267.meta was generated (see Chapter 3.1.2), and PfFNT G107S-GFP was expressed in HEK293 cells. G107S mutation was introduced using site-directed mutagenesis, as described in the Chapter 2.2.2.4. Sequencing analysis confirmed the codon exchange at position 321 (GGT-to-AGT) (Figure 3.9).
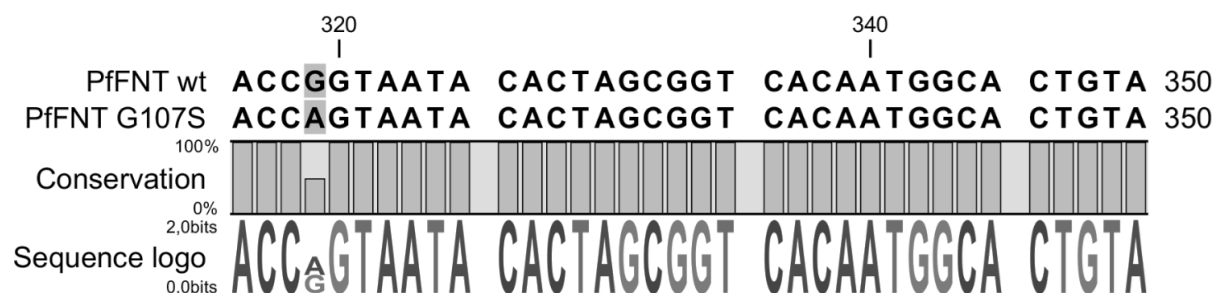
Figure 3.9 Sequence alignment using CLC Workbench.

As before, the expression of PfFNT G107S-GFP (61 kDa) was evaluated with SDS-PAGE and Western blotting, yielding the same bands as for PfFNT wild type (Figure 3.10). Confocal laser scanning microscopy revealed efficient targeting and incorporation of PfFNT G107S-GFP into the plasma membrane of HEK293 cells (Figure 3.11) (Jakobowska et al., 2021). The expression levels and localization of cells expressing wild type and mutant PfFNT-GFP were comparable (Jakobowska et al., 2021).
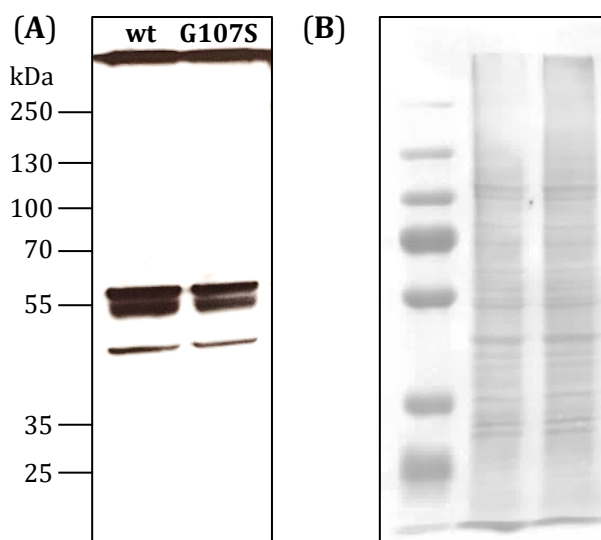
Figure 3.10 Expression of the PfFNT G107S-GFP fusion construct. (**A**) Western blot showing the expression of PfFNT G107S fused with GFP and (**B**) Ponceau staining. 30 μg of total protein were loaded per lane. Protein was detected using an anti-GFP antibody. Exposure time: 30 s. PfFNT wild type was blotted as a control.
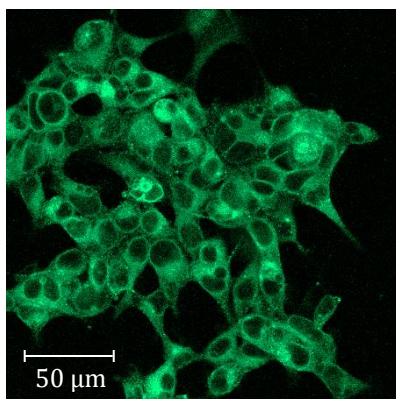
Figure 3.11 Confocal microscopy of monoclonal PfFNT G107S carrying C-terminal green fluorescent protein stably expressed in human embryonic kidney 293 cells. The fluorescence microscopic image of an isolated monoclonal cell subpopulation of the PfFNT G107S-GFP fusion protein. The PfFNT mutant showed an effective expression at the cellular membrane. The expression levels and localization of cells expressing wild type and mutant PfFNT-GFP are similar, for comparison see Figure 3.3 (Jakobowska et al., 2021).

3.1.5 Intracellular binding of BH267.meta-DY647 to PfFNT G107S-GFP

The results described in this chapter have been published as (Jakobowska et al., 2021). To determine if ligands can bind to the PfFNT mutant, human embryonic kidney 293 cells stably expressing PfFNT G107S-GFP were incubated with BH296-DY647 or BH267.meta-DY647 after treatment with 0.05% Triton X-100. As expected, at 50 nM BH296 did not localize to membranes with PfFNT G107S, which is consistent with the inhibitor's inactivity against PfFNT G107S (Figure 3.12A) (Golldack et al., 2017; Nerlich et al., 2021; Walloch et al., 2020). However, under the same conditions, BH267.meta-DY647 showed a clear membrane stain (Figure 3.12B). Nevertheless, a direct comparison demonstrated that the intensity of staining was lower than observed with BH296-DY647 on cells expressing PfFNT wild type, see Figure 3.7C. The interaction could be competed with unlabelled BH267.meta but not with BH296 (Figures 3.12C and 3.12D). Additionally, BH267.meta also binds effectively to PfFNT wild type, and as compared to mutant PfFNT, the observed signal intensity of labelled BH267.meta-DY647 appears to be higher (Figure 3.12E). Conclusions about whether differences in signal intensity are caused by differing affinities, target protein expression levels, or cellular localization cannot be drawn from imaging-based experiments and require the use of biophysical analytical methods. However, the observation confirms previous findings that show the activity of BH267.meta on PfFNT G107S (Nerlich et al., 2021; Walloch et al., 2020). The results also prove that PfFNT G107S-GFP and BH267.meta-DY647 are functional and can be further used in FCCS experiments (Jakobowska et al., 2021).
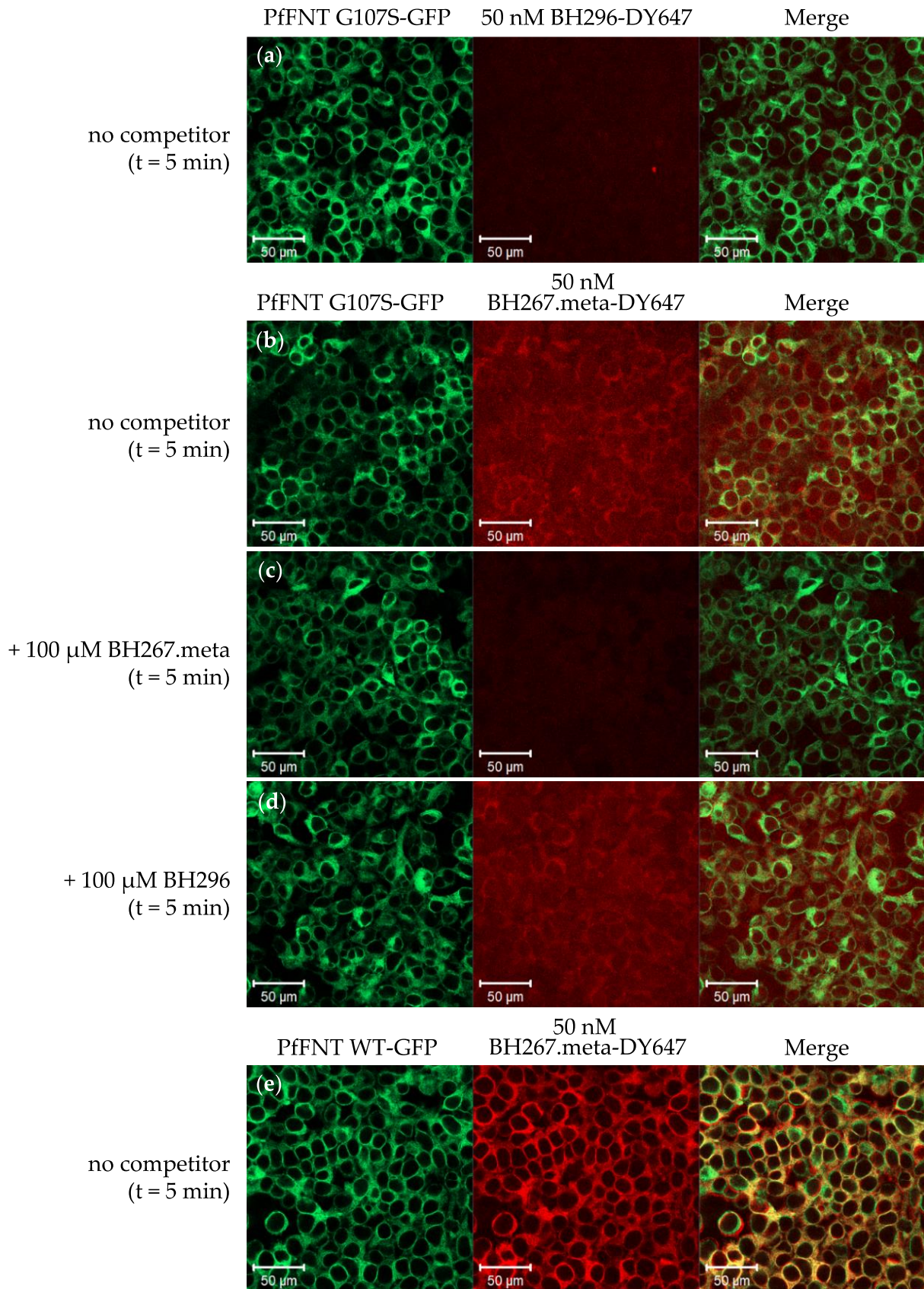
Figure 3.12 Live cell imaging of mutant PfFNT G107S-GFP stably expressed in HEK293 cells and binding of labelled ligands BH296-DY647 and BH267.meta-DY647. The membrane-bound G107S mutant of PfFNT-GFP co-localizes with BH267.meta-DY647 (**B**), but not BH296-DY647 (**A**), and competition with 100 μM BH267.meta prevents membrane localization (**C**). The

intensity of fluorescence indicates that the interaction between BH267.meta-DY647 and the G107S mutant is weaker than that between BH296-DY647 and wild type PfFNT-GFP, as shown in Figures 3.7B and C. (**D**) The interaction cannot compete with BH296. (**E**) BH267.meta-DY647 localizes with PfFNT wild type. The incomplete overlap between both channels in Figure E is not significant for the experiment's conclusion as it is caused by an offset between the channels (Jakobowska et al., 2021). The figure is reprinted from (Jakobowska et al., 2021).

3.2 Affinity determination of drug-target interaction using FCCS

Many approaches of characterizing the interaction of inhibitors with their targets rely on purified proteins and interacting components, although many proteins unfold their full activity only in the presence of binding partners and cofactors (Jakobowska et al., 2021). Confocal microscopy is extremely useful for studying the subcellular distribution of molecules (Pygall et al., 2007). This method, however, offers limited insight into the possible association of compounds with homogeneously distributed intracellular structures. Moreover, information on concentrations is very difficult to obtain. Therefore, FCS and FCCS are the methods of choice for the investigation of the interaction of small compounds with subcellular structures at low concentrations.

3.2.1 Solubilization of PfFNT in a functional form

After showing the specific binding, next it was set out to determine the affinities and rate constants using the single molecule sensitive FCCS technology. Although FCCS allows for the direct detection and real-time monitoring of intermolecular interactions in crude cell lysates, to facilitate subsequent analysis it should be carried out with monodisperse solutions containing soluble or solubilized targets (Antoine et al., 2016). Hydrophobic integral membrane proteins, such as PfFNT, can be solubilized with detergents to create solutions containing native proteins (Antoine et al., 2016; Grisshammer, 2009). In this study, the generated earlier HEK293 cell lines that stably express PfFNT-GFP or PfFNT G107S-GFP as well as the BH296 and BH267.meta compounds carrying red fluorescent DY647 were used. In order to achieve the best solubilization, a variety of detergents were tested at concentrations ranging from 0.25% to 1%, with the goal of maximizing solubilization efficiency while avoiding denaturing effects on the target protein. Additionally, the concentrations were chosen to remain below the critical micellar concentration (CMC), because detergent micelles have the propensity to incorporate hydrophobic small molecule compounds, rendering them inaccessible for interaction with the target protein and delaying their diffusion speed, giving the misleading impression that they are part of the bound fraction (Jakobowska et al., 2021). During the

investigation, various detergents including LMNG (1%), DDM (1%, 0.5%, 0.25%), DM (1%), CHAPS (1%) and LDAO (1%, 0.5%) were assessed for their effectiveness in solubilizing the membrane. A detergent mixture of CHAPS, DDM, and CHS was also examined (Jakobowska et al., 2021).
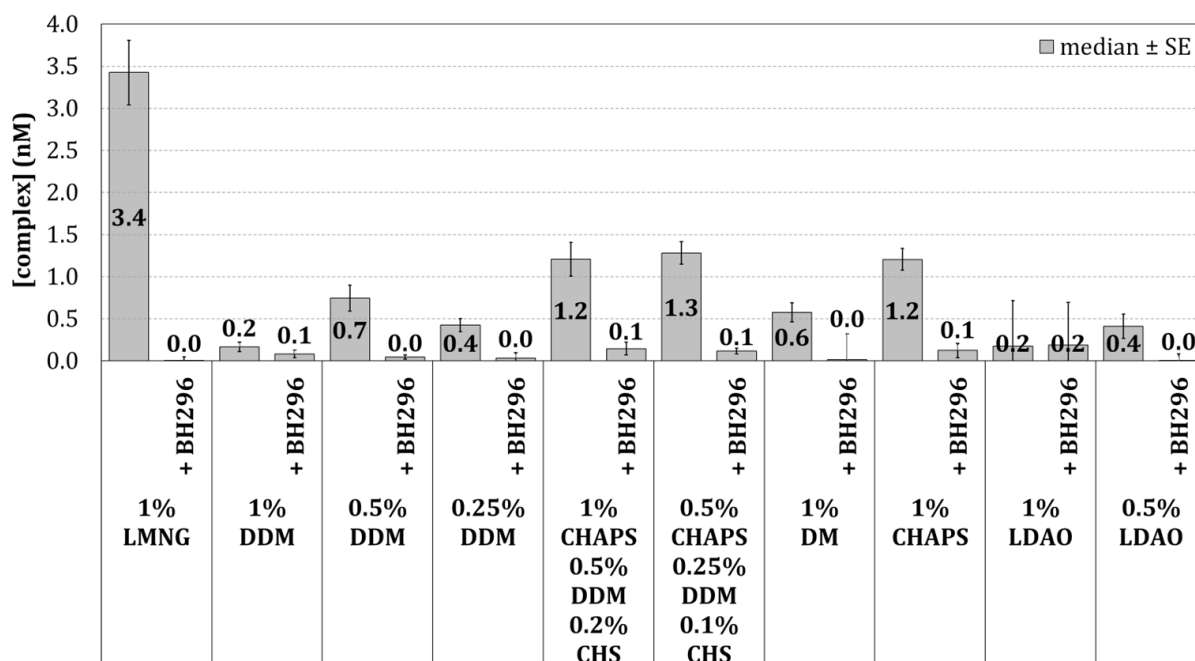

Figure 3.13 FCCS analysis of cells lysed with different detergents. Membranes from HEK293 cells expressing PfFNT-GFP were extracted and solubilized using a variety of detergents as explained in the Materials and Methods section. Solubilized receptors were incubated with 50 nM BH296-DY647 in absence or presence of 10 μM unlabelled BH296 for 1 h at room temperature, and receptor-ligand complexes were then detected by FCCS. The bars represent the number of receptor-ligand complexes (mean ± SE from three independent experiments).

FCCS analysis showed high complex formations (> 1.2 nM) for samples treated with 1% LMNG, 1% CHAPS, as well as a detergent mixture – 0.5% CHAPS, 0.25% DDM, 0.1% CHS (Figure 3.13). Samples lysed with DDM, DM and LDAO showed less complex formation (< 0.7 nM) indicating that these detergents were less effective in solubilizing, or denatured the protein to a degree that prevented compound binding. Analyzing sample trace lines of FCS measurements for the presence of aggregates, displayed as high peaks, revealed that samples solubilized with 1% LMNG were free of aggregates, whereas in samples lysed with 1% CHAPS and the detergent mixture some aggregates were detected (Figure 3.14). Aggregates may lead to an erroneous rise in the amount of complex formed. For optimization of detergent concentration, 1%, 0.5% and 0.25% LMNG was investigated (Figure 3.15). After testing different conditions, it was found that LMNG at 1% concentration resulted in the highest level of complex formation between PfFNT and the

fluorescent inhibitor probe, as measured by FCCS. These conditions were then used in further experiments (Jakobowska et al., 2021).
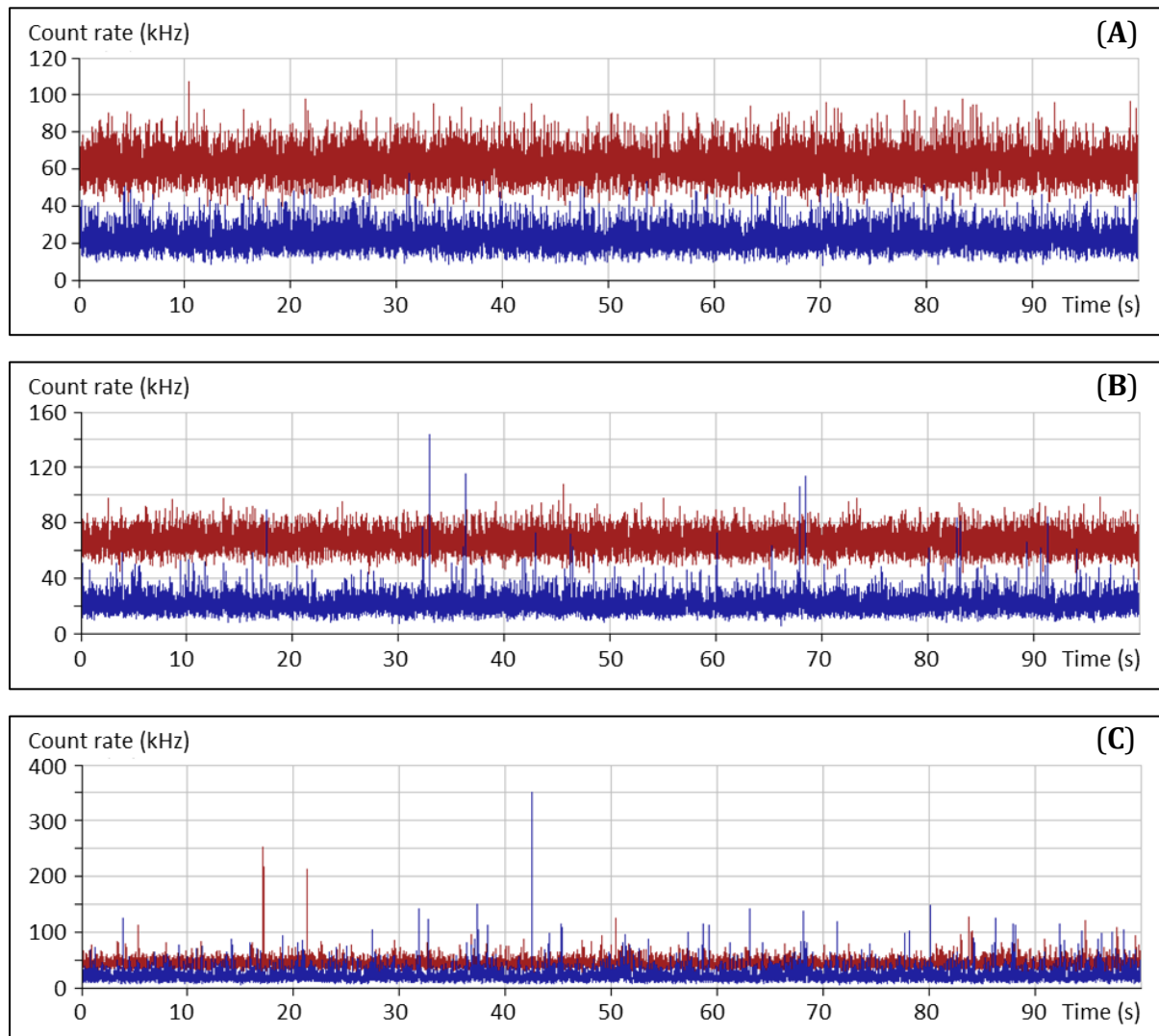

Figure 3.14 FCS trace lines tracing fluorescence fluctuations and detecting aggregates during measurement. Red line, trace line for BH296-DY647; blue line, trace line for PfFNT-GFP. Samples lysed with (**A**) 1% LMNG, (**B**) detergent mixture - 0.5% CHAPS, 0.25% DDM, 0.1% CHS, (**C**) 1% CHAPS.

Next, solubilized membranes from human embryonic kidney 293 cells expressing PfFNT were analyzed for expression levels *via* GFP fluorescence intensity as well as diffusion times. The preparation and solubilization of the membrane resulted in a concentration of 10 nM of PfFNT protein (for more details see Chapter 2.2.3.5). The autocorrelation functions of the GFP-fusion proteins could be fitted by a 1-component diffusion model with diffusion times between 350 and 400 µs, which is in good agreement with protein-sized particles and indicates homogeneously monodisperse proteins (Figure 3.16) (Jakobowska et al., 2021).
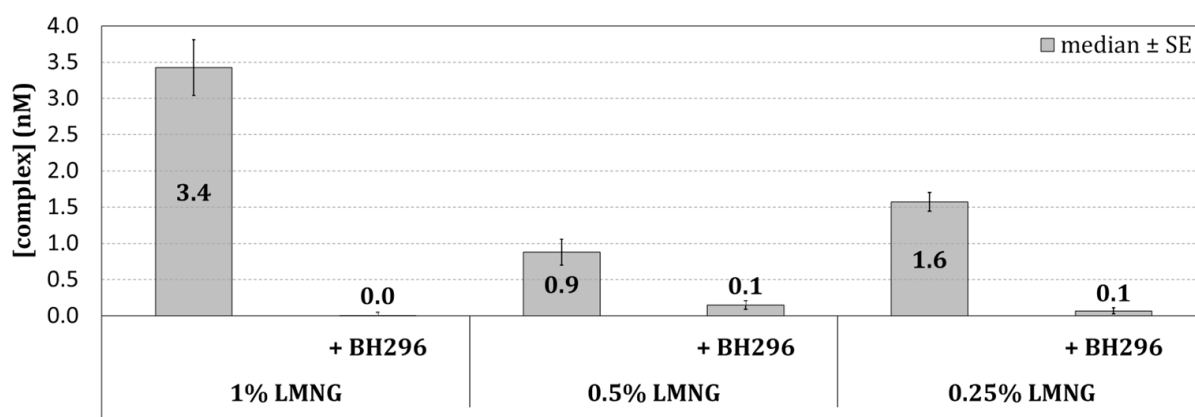
Figure 3.15 FCCS analysis of samples lysed with different LMNG concentrations. Membranes from HEK293 cells expressing PfFNT-GFP were extracted and solubilized using 1%, 0.5% and 0.25% LMNG. Solubilized receptors were incubated with 50 nM BH296-DY647 in absence or presence of 10 µM unlabelled BH296. The bars represent the number of receptor-ligand complexes (mean ± SE from three independent experiments).
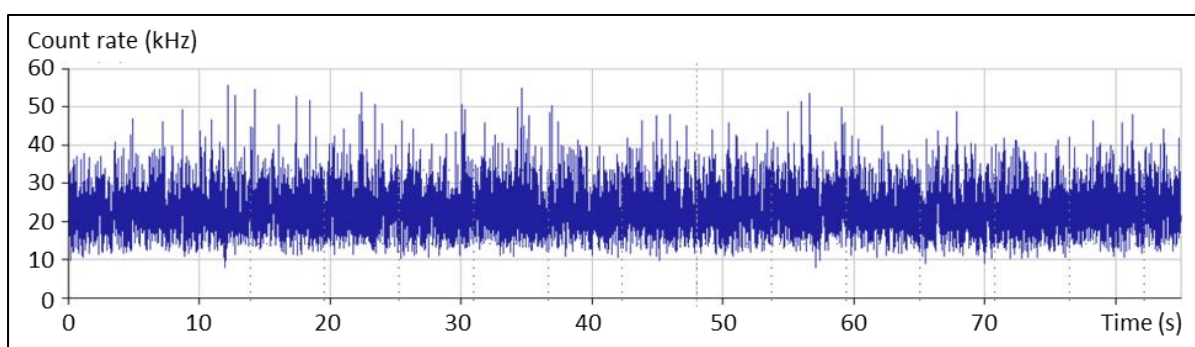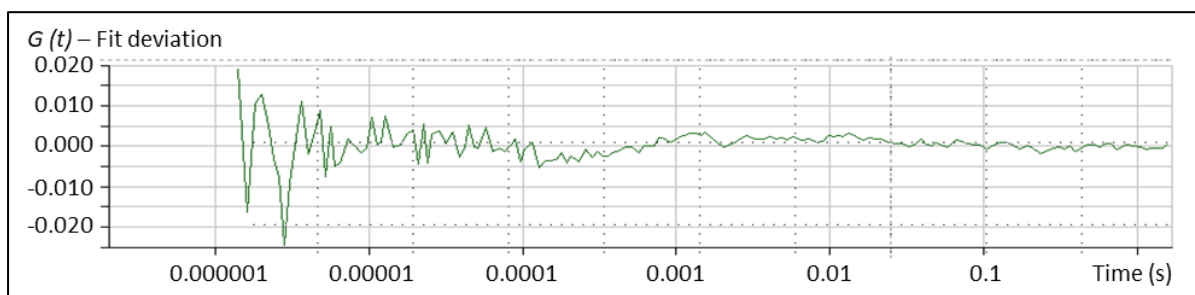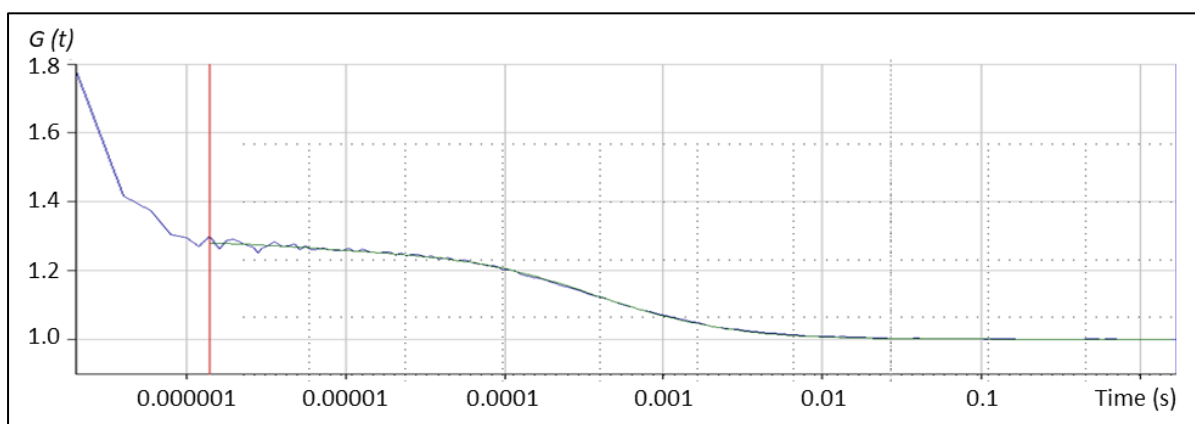
Channel	Count rate [kHz]	Counts per molecule [kHz]	Amplitude number particles	Component 1 diffusion time [µs]
GFP	22.8	5.944	2.536	373

Figure 3.16 Homogeneous and monodispersed solubilization of PfFNT-GFP. FCS signal fluctuations induced by PfFNT-GFP solubilized in 1% LMNG (upper panel), corresponding correlation curve fitted to a 1-component diffusion model with fit deviation (lower panel) (Jakobowska et al., 2021). The figure is reprinted from (Jakobowska et al., 2021).

Figure 3.17 shows an example of data obtained from the FCCS measurements of PfFNT-GFP solubilized in 1% LMNG. The fluorescence fluctuations were auto- and cross-correlated and a fitting formalism was employed accounting for one diffusing species for receptor-GFP and two diffusing species for ligand-DY647 (quickly diffusing, unbound fraction and the protein-bound fraction of drug molecules) (Antoine et al., 2016; Jakobowska et al., 2021). The diffusional autocorrelation time of free BH296-DY647 was determined in a reference measurement, in TBS-PIC buffer, to be 139 s.
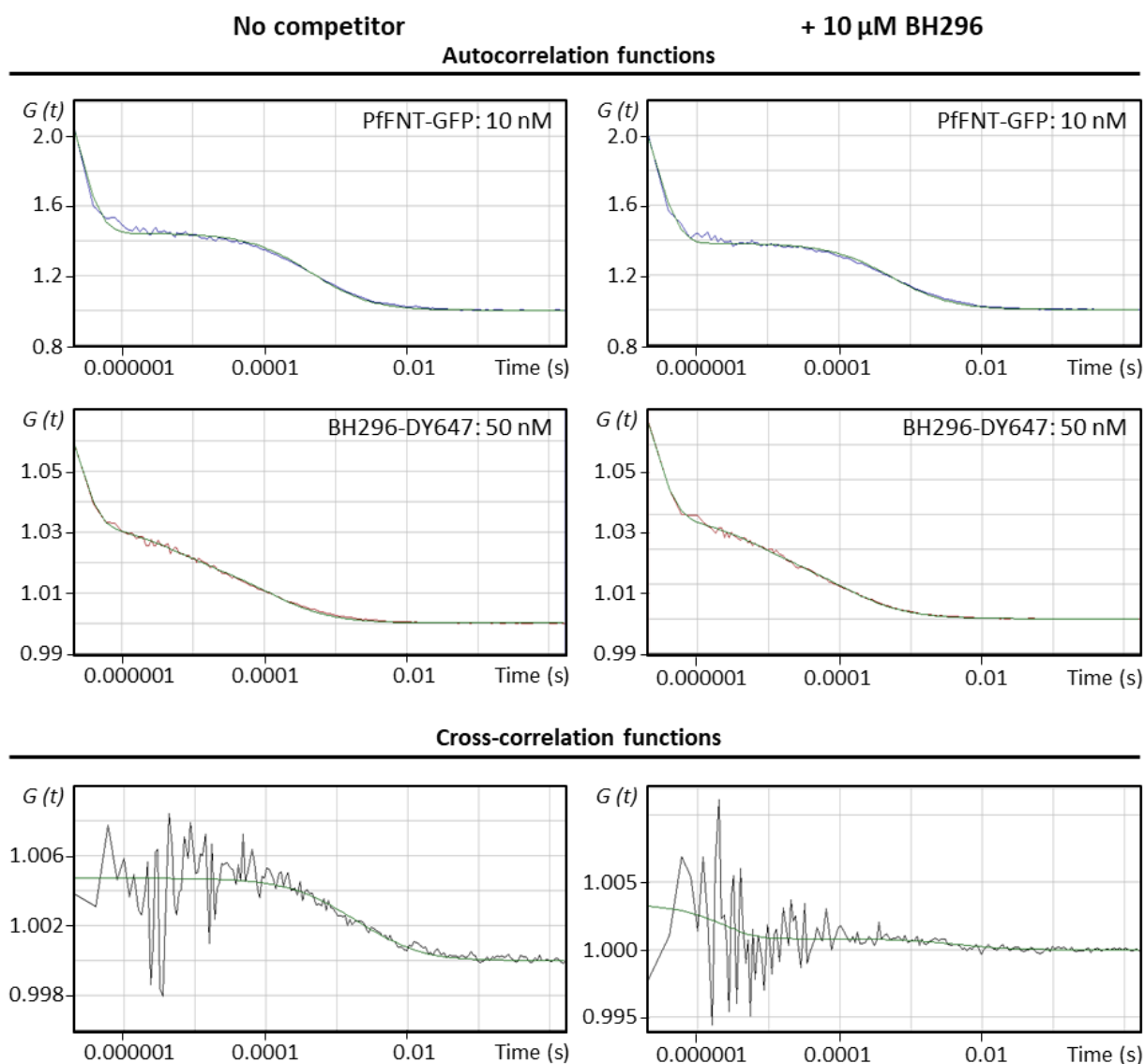
Figure 3.17 Autocorrelation and cross-correlation functions derived from the FCCS experiments with solubilized PfFNT. Autocorrelation functions of both, BH296-DY647 (red) and PfFNT-GFP (blue) as well as the cross-correlation functions (black) were acquired by FCCS.

Ligand binding assays were performed in the absence or presence of a competitor. Binding assay with 10 nM PfFNT-GFP and 50 nM BH296-DY647 (left panel). Binding assay with 10 nM PfFNT-GFP and 50 nM BH296-DY647 in presence of 10 µM unlabelled BH296 (right panel).

The calculated concentrations of the fluorescent probe, PfFNT-GFP fusion protein and receptor-ligand complex as well as diffusion time in the confocal volume corresponding to all populations are listed in Table 3.1. Using the labelled ligand and active receptor, the findings demonstrate that when BH296-DY647 binds to solubilized PfFNT-GFP, it (i) causes a noticeable shift in the diffusion time of BH296-DY647 due to the substantial difference in molecular weight between free and receptor-bound BH296-DY647, and (ii) is entirely blocked by an excessive amount of unlabelled BH296 (10 µM) (Antoine et al., 2016; Jakobowska et al., 2021).

Table 3.1 Concentrations and diffusion times of PfFNT-GFP and BH296-DY647 determined in the FCCS measurements.

Receptor	Fluoresc-ent probe	Compe-titor	L_T (nM)	Fluorescent probe				Receptor-GFP				
				free		bound		R_T (nM)	p (t_1)	t_1 (µs)	p (t_2)	t_2 (µs)
				p (t_1)	t_1 (µs)	p (t_2)	t_2 (µs)					
PfFNT-GFP	BH296-DY647	-	50	75 %	139	25 %	1200	10	100 %	373	-	-
		10 µM BH296		100 %	139	-	-		100 %	386	-	-

%t_1, population of bound ligand or receptor in percent; %t_2, population of free ligand or receptor in percent; t_1 or t_2, diffusion time in µs corresponding to bound or free population; L_T or R_T, concentration of ligand or receptor in nM

3.2.2 Saturation binding assays with solubilized PfFNT

The results described in this chapter have been published as (Jakobowska et al., 2021). After validating the specificity of ligands binding and optimizing the solubilization conditions, the inhibitor binding affinities for PfFNT wt and its G107S mutant were calculated. To obtain saturation binding curves and determine the dissociation constant (K_D) of the interactions, solubilized cell membranes containing PfFNT-GFP at a concentration of 10 nM were dispensed as 20 µl aliquots into the 384-well glass bottom plates and incubated with labelled inhibitor molecules, BH296-DY647 or BH267.meta-DY647. It must be ensured that both binding partners are present in sufficient amounts as freely accessible components so that the equilibrium can be established unhindered. For this reason, the concentration of the labelled ligands was first titrated against the lysate. The DY647 compounds were added to the first well containing solubilized PfFNT in large excess (200 nM) and then reduced by serial dilution from well to well. Thereby

labelled inhibitors concentration was titrated over a concentration range from 200 nM to 1 nM. After 1-hour incubation at ambient temperature, to allow the formation of drug-target complexes, the FCCS measurements were done on the Evotec Insight plate reader (Evotec Technologies, Hamburg) (Antoine et al., 2016). Excitation of laser lines was adjusted to 20 μW in both channels to ensure that bleaching is negligible and the excitation is in the dynamic range of both dyes. For each dilution, correlation functions were recorded over 8 seconds with 12 repetitions and particle numbers, molecular brightness and diffusion times of free and bound particles in both channels determined. Equilibrium binding studies were performed in biological triplicates. Figure 3.18 and 3.19 presents data obtained from the equilibrium saturation binding assays, and Table 3.2 summarizes the derived K_D values (Jakobowska et al., 2021).

Table 3.2 Determination of K_D values in equilibrium binding assays by FCCS. The table is reprinted from (Jakobowska et al., 2021).

Target	Fluorescent probe	K_D (nM)	Active receptor (%)
PfFNT wt-GFP	BH296-DY647	67 ± 6	68 ± 3
	BH267.meta-DY647	72 ± 1	100
PfFNT G107S-GFP	BH296-DY647	> 2000	n.d.
	BH267.meta-DY647	405 ± 1	100

BH296 and BH267.meta bound to PfFNT wild type with a similar affinity of 67 and 72 nM (Figure 3.18A), respectively. The saturation binding curves revealed similar affinities for BH267.meta and BH296; however, the actual concentration of complexes was notably different, with 6 and 3 nM for BH267.meta and BH296 respectively. The reason for the difference in complex concentration is that there is a substantially lower amount of binding competent PfFNT-GFP protein available for BH296. The result was unexpected given that the same sample of solubilized membranes was used for both tracer molecules. To investigate this further, the experiment was repeated using varying concentrations of solubilized PfFNT-GFP. Additionally, to ensure that tracer instability was not a factor, the batch employed for the saturation binding assays was repurified using reversed phase HPLC. However, even with quality-controlled tracers, the experiments produced the same outcomes. In conclusion, the affinities determined from the recorded saturation binding curves' slopes are similar, although only a fraction of about half of PfFNT-GFP seems to exhibit binding competence for the labelled form of BH296. In contrast,

BH267.meta-DY647 binds to 100% of the accessible target with a similar affinity (Figure 3.18A) (Jakobowska et al., 2021). This difference can be explained by conformational changes in PfFNT. Proteins are able to change their conformation, or shape, in response to different conditions, such as changes in pH, temperature, or the presence of other molecules (Bruce, 1989; Ha & Loh, 2012; O'Brien et al., 2012). These changes in conformation can either open or close the protein, leading to changes in binding sites and activity, like increased/decreased enzymatic activity, binding affinity, and molecular interaction regulation. It is presumed that BH267.meta, which takes up less space in the binding pocket, is likely to bind to PfFNT in both open and closed conformations, while bulkier BH296 cannot bind to closed conformation of PfFNT due to limited access to the binding site (Jakobowska et al., 2021).
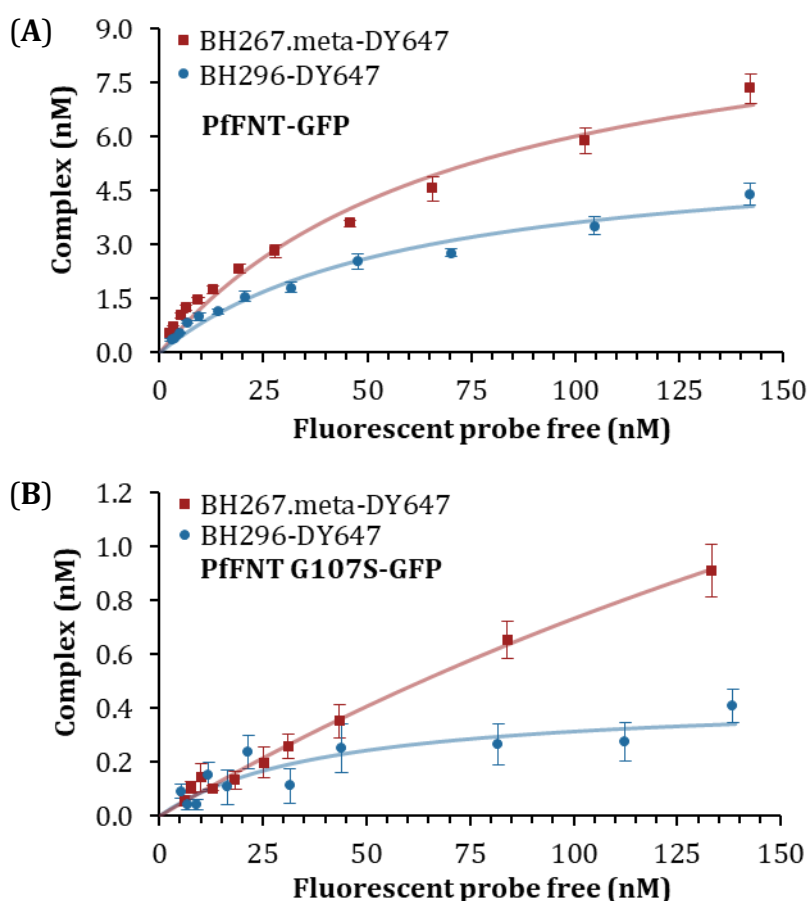
Figure 3.18 Equilibrium saturation binding assays of BH296-DY647 and BH267.meta-DY647 to PfFNT wt and PfFNT G107S. (**A**) BH296-DY647 and BH267.meta-DY647 bound with similar affinity to PfFNT (67 nM and 72 nM, respectively). However, binding to BH296-DY647 was saturated with only 50% of the target involved in interactions, whereas BH267.meta bound to 100% of the GFP-fusions of wild type PfFNT. (**B**) Saturation binding assays of BH296-DY647 to mutant PfFNT G107S-GFP indicated no affinity above background caused by fluorescence cross talk, but BH267.meta-DY647 bound with a K_D of 405 nM (Jakobowska et al., 2021). The figure is reprinted from (Jakobowska et al., 2021).

The binding of both tracers to the mutant PfFNT G107S was then measured using equilibrium saturation binding assays. The obtained data show weaker affinity by BH267.meta (K_D: 405 nM), whereas BH296 failed to bind within detection limits (Figure 3.18B, Table 3.2), thereby reconfirming the observations of confocal imaging (Jakobowska et al., 2021).
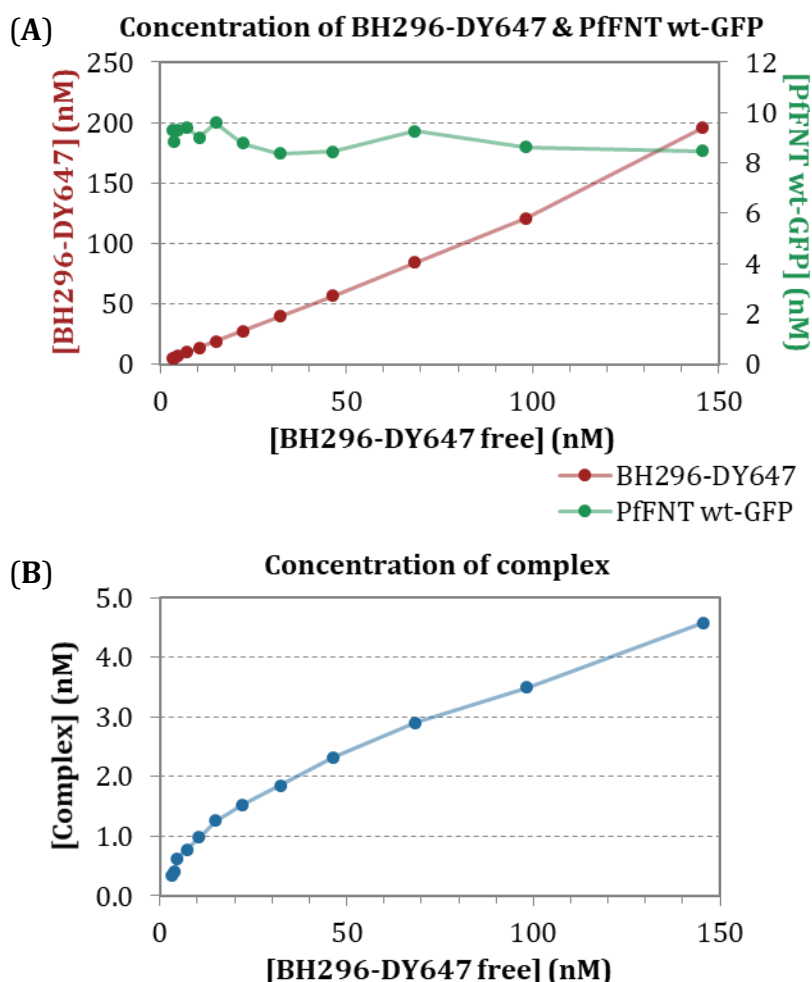

Figure 3.19 Changes in receptor and ligand concentrations (**A**) **and complex formation** (**B**) **during saturation binding assay exemplified by PfFNT wt-GFP and BH296-DY647**. Lysate comprising approximately 10 nM of solubilized PfFNT wt-GFP was incubated for 1 h with 200 nM to 1 nM BH296-DY647 (2:3 serial dilution).

3.2.3 Competition binding assays with solubilized PfFNT

The results described in this chapter have been published as (Jakobowska et al., 2021). To rule out any influence of both linker and fluorescent label on the measured affinity and to analyze the binding properties of unlabelled inhibitors BH296 and BH 276.meta, their inhibition constants (K_i) were determined in competition binding assays. For this, membrane preparations comprising 10 nM of PfFNT wild type were incubated with fluorescent probe BH296-DY647 at a concentration around its K_D value (70 nM) and

titrated with unlabelled compounds in a concentration range between 10 μM and 10 pM. Complex formation between PfFNT-GFP and BH296-DY647 without competitor corresponds to the values observed in saturation binding assays. Competition of the interaction between labelled binding partners resulted in a dose-dependent decline of cross-correlating particles (Figure 3.20) (Jakobowska et al., 2021).
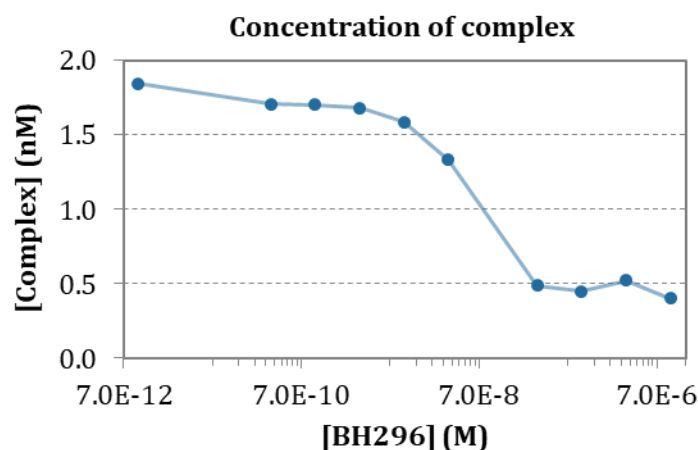

Figure 3.20 Changes in complex formation during competition binding assay exemplified by PfFNT wt-GFP and BH296-DY647 in presence of unlabelled BH296 applied at various concentrations. Lysate comprising approximately 10 nM of solubilized PfFNT wt-GFP was mixed with 70 nM BH296-DY647 and incubated for 1 h with a serial dilution of unlabelled BH296 in DMSO in a concentration range from 10 μM to 10 pM.

Plotting of the concentration of drug-target complexes against the concentration of competitor yielded an inhibition curve from which an IC_{50} value could be deduced. The competition curves for both inhibitors have comparable IC_{50} values, as shown in Figure 3.21A. The corresponding K_i values were then calculated by applying the Cheng-Prusoff equation (Antoine et al., 2016; Cheng & Prusoff, 1973; Jakobowska et al., 2021). The K_i values for both unlabelled inhibitors to PfFNT wt are shown in Table 3.3, indicating similar high affinity to its target. The minor change in affinity compared to saturation binding experiment data demonstrates that, despite its bulkiness, the fluorophore has no significant influence on the interaction with the target (Jakobowska et al., 2021).

Table 3.3 Determination of K_i values in equilibrium binding assays by FCCS. The table is reprinted from (Jakobowska et al., 2021).

Target	Fluorescent probe	K_i competitor (nM)	
		BH296	BH267.meta
PfFNT wt-GFP	BH296-DY647	48 ± 2	66 ± 6
	BH267.meta-DY647	47 ± 1	56 ± 3
PfFNT G107S-GFP	BH267.meta-DY647	> 10,000	417 ± 16

Next, both unlabelled compounds were tested in competition experiments with BH267.meta-DY647 as the probe. The same PfFNT-GFP membrane preparation as in the previous experiment was incubated with BH267.meta-DY647 at a concentration of 70 nM to facilitate complex formation. Competitors BH296 and BH267.meta were added to the interaction at concentrations ranging from 10 µM to 10 pM (using a dilution factor of 3.16). The mixture was then incubated at room temperature for an hour to reach equilibrium (Jakobowska et al., 2021).
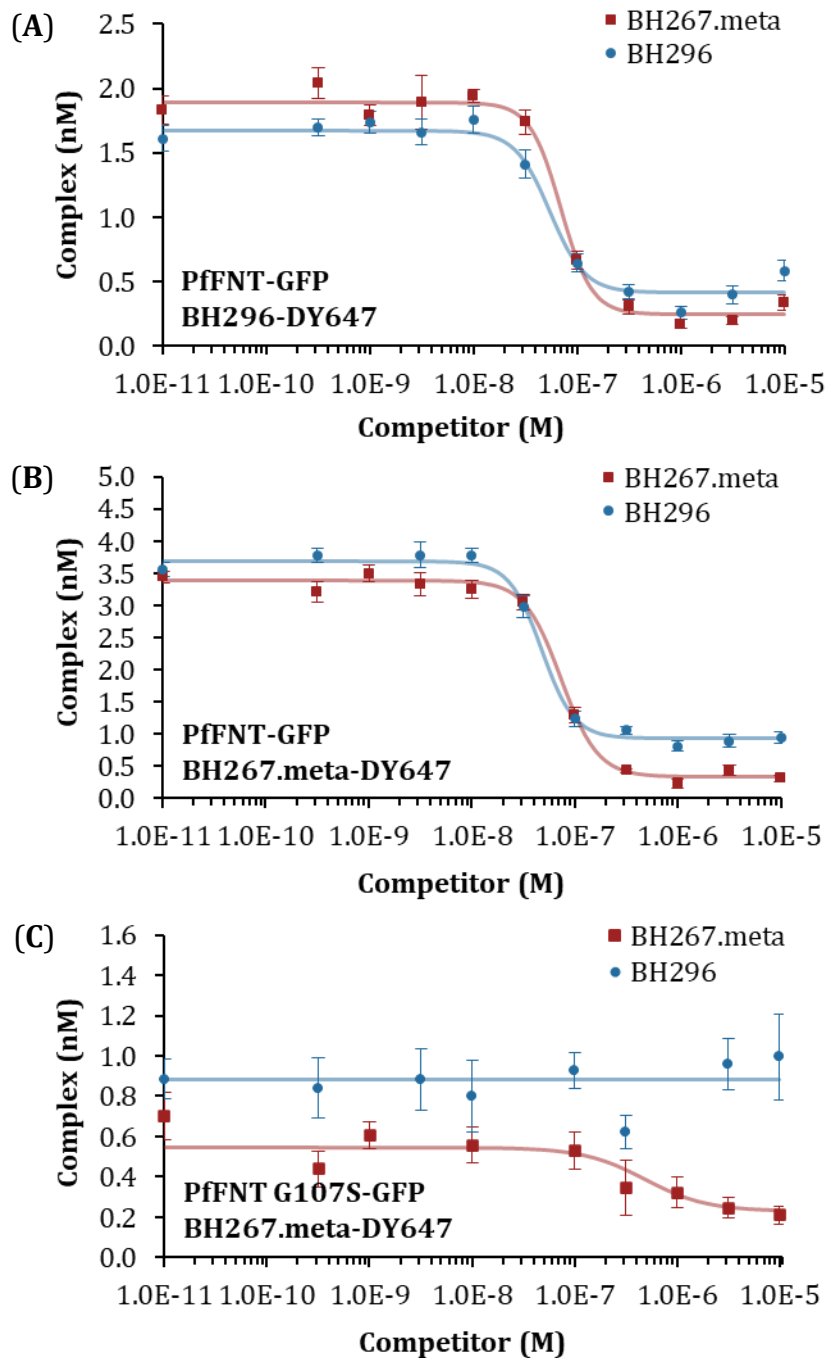
Figure 3.21 Affinity determination of BH296 and BH267.meta to PfFNT wt and PfFNT G107S. (A) Membrane preparations containing 10 nM of PfFNT-GFP were incubated with 70 nM

BH296-DY647, and obtained complexes were competed with unlabelled compounds BH296 and BH267.meta to assess their K_i values. In the absence of a competitor, 1.5 nM of complex was formed, and the tracer was entirely displaced by both compounds with a K_i of 48 and 66 nM, respectively. (**B**) By using BH267.meta-DY647 as a tracer, the two compounds displaced a total of 3 nM complexes, with K_i values of 47 and 56 nM. (**C**) Membrane preparations containing GFP-fusions of mutant PfFNT G107S were mixed with 70 nM of the labelled BH267.meta and competed with BH267.meta and BH296.Only BH267.meta displaced the tracer with a K_i of 417 nM, whereas BH296, even at concentrations of 10 µM, did not compete in the interaction (Jakobowska et al., 2021). The figure is reprinted from (Jakobowska et al., 2021).

With a K_i of 56 nM, BH267 meta replaced the labelled tracer, and despite a residual background signal, the tracer was entirely dissociated from the target. In contrast, while having a comparable measured K_i of 47 nM, BH296 was unable to completely replace the labelled BH267.meta molecule. Regardless of competitor concentration or incubation period, a significant amount of 20% of the complex remained intact. This finding is of interest because it reflects how BH296-DY647 behaved in saturation binding assays, where a subfraction of the target was unable to bind to the more space-occupying BH296 (Figure 3.21B, Table 3.3) (Jakobowska et al., 2021). The K_i values estimated for the interaction of BH296 and BH267.meta with mutant PfFNT G107S support the affinities shown for the direct interactions with labelled inhibitors. BH296 does not interfere with the binding of labelled BH267.meta to PfFNT G107S, but parental BH267.meta competes in this interaction with a K_i of 417 nM (Figure 3.21C, Table 3.3). Together, the findings on inhibitor affinity are consistent with earlier microscopic studies that showed high signal intensities for labelled BH296 and BH267.meta binding to PfFNT wild type, no binding of BH296 to PfFNT G107S, while BH267.meta-DY647 exhibited binding to PfFNT G107S (Jakobowska et al., 2021).

3.2.4 Binding kinetics of labelled BH296 and 267.meta to PfFNT by time-resolved FCCS measurements

The results described in this chapter have been published as (Jakobowska et al., 2021). To complete the biophysical interaction analysis, the rate constants of both labelled inhibitors to PfFNT wild type were determined. This is significant because inhibitors with the same affinity (K_D) but varying association and dissociation rates may demonstrate distinct biological activity profiles (Antoine et al., 2016). The time a compound spends on its target, also known as the drug-target residence time, is defined as the reciprocal value of the dissociation rate constant ($1/k_{off}$) and has been proven to be crucial for target selectivity and the duration of its inhibitory effect (Antoine et al., 2016; Copeland et al., 2006; Guo et al., 2014; Jakobowska et al., 2021; Lu & Tonge, 2010; Núñez et al., 2012).
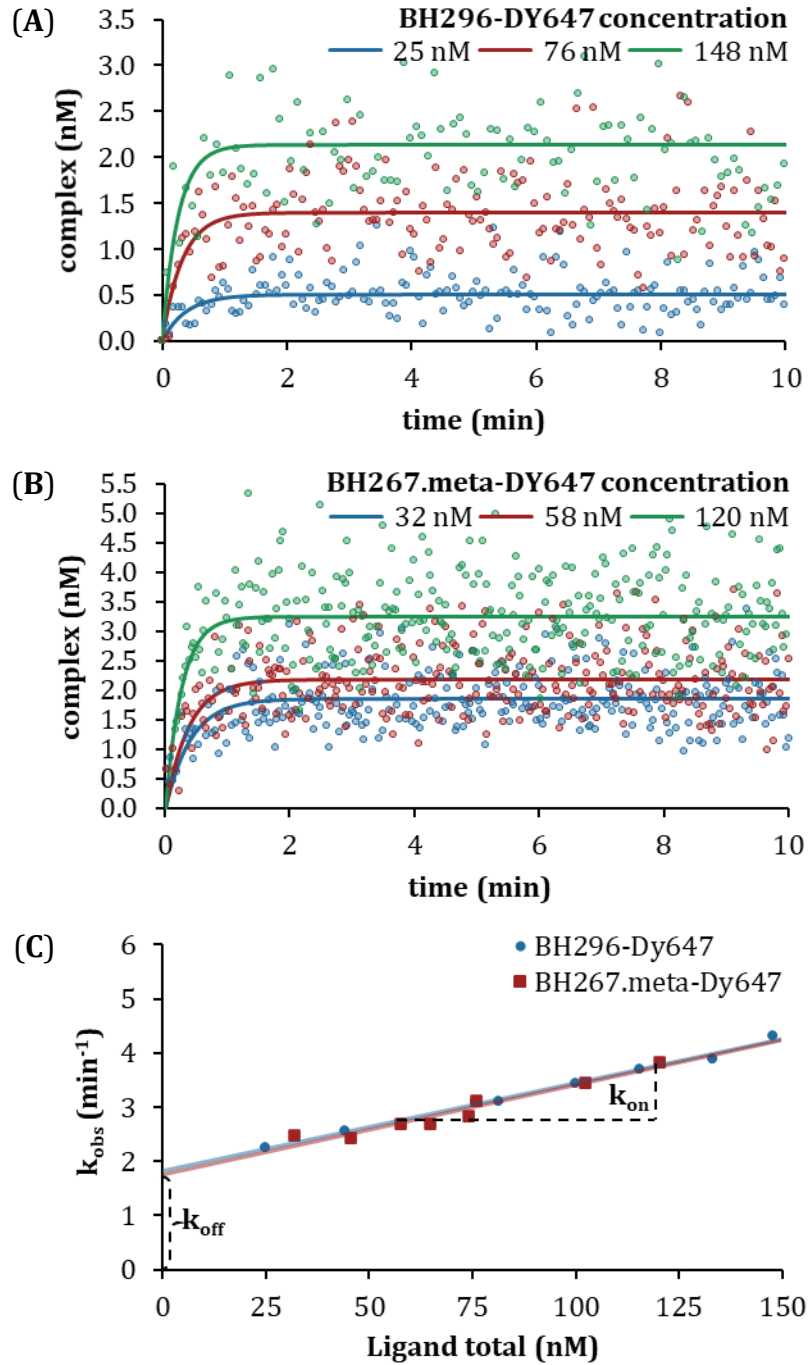
Figure 3.22 Kinetic studies of the fluorescent probes BH296-DY647 and BH267.meta-DY647 with PfFNT wt-GFP by FCCS. Representative time-resolved measurements of the interaction between 10 nM solubilized PfFNT-GFP and the three indicated concentrations of BH296-DY647 (**A**) or BH267.meta-DY647 (**B**) (Antoine et al., 2016). The data points represent the experimental values of complexes that were measured for a duration of 2-6 seconds (Antoine et al., 2016). The solid lines represent the best fitted curves according to the equation presented by (Antoine et al., 2016) and yielding reaction rates kobs of 2.3, 3.1, 4.3 min-1 for 25, 76 and 148 nM BH296-DY647, or 2.5, 2.7, 3.8 min-1 for 32, 58 and 120 nM BH267.meta-DY647. (**C**) The kobs-values were plotted versus the concentrations of the fluorescent probe. The most accurate linear regression is shown by the solid line, and the slope and y-intercept were used to estimate the kon and koff of the two fluorescent probes, respectively (Antoine et al., 2016; Jakobowska et al., 2021). kon and koff values of BH296-DY647 and BH267.meta-DY647 are summarized in Table 3.4 (Jakobowska et al., 2021). The figure (C) reprinted from (Jakobowska et al., 2021).

For this reason, the kinetics of the receptor-ligand interaction were characterized using the fluorescent inhibitors as probes. For assessing the kinetics of direct interactions between PfFNT and the labelled inhibitor molecules, the target at a concentration of approximately 10 nM was mixed with fluorescent probes (BH296-DY647 or BH267.meta-DY647) at concentrations that exceeded the concentration of the receptor by a factor of 10 (Antoine et al., 2016). This method guaranteed that the depletion of free ligands remained insignificant during the kinetic measurements (Antoine et al., 2016). Initially, time-resolved binding curves were obtained for ligand concentrations of 148, 133, 115, 100, 81, 76, 44, 25 nM (BH296) and 120, 102, 76, 74, 65, 58, 46, 32 nM (BH267.meta), respectively, to obtain different observed rate constants (k_{obs} values) (Figure 3.22). In view of the fast complex formation, the kinetics were monitored over the course of 10 min, during which the single measurements were taken for 2-6 s (Antoine et al., 2016). Examples of kinetic traces for the two fluorescent probes binding to PfFNT at different concentrations are displayed in Figures 3.22A and 3.22B (Jakobowska et al., 2021).

Table 3.4 k_{on} and k_{off} values determined in time-resolved FCCS-based binding assays. The table is reprinted from (Jakobowska et al., 2021).

Target	Fluorescent probe	k_{on} (nM^{-1} min^{-1})	k_{off} (min^{-1})	K_D (kinetics, nM)	K_D (equilibrium, nM)
PfFNT wt-GFP	BH296-DY647	0.0167 ± 0.0006	1.8659 ± 0.0339	113 ± 2	67 ± 6
	BH267.meta-DY647	0.0161 ± 0.0005	1.7839 ± 0.0250	112 ± 5	72 ± 1

Then k_{on} and k_{off} values were calculated by linear regression, with the slope providing the k_{on} value and the y-intercept the k_{off} value (Figure 3.22C) (Antoine et al., 2016), for more details see Chapter 2.2.7.3. Both inhibitors are characterized by a rapid association and bind and disassociate with equal rate constants (Table 3.4). Equilibrium is reached within less than 1 min at nanomolar inhibitor concentrations. To cross-validate, the accuracy of the kinetic calculations, K_D values acquired from saturation binding assays were compared with affinities deduced from the kinetic rate constants by dividing k_{off} by k_{on} (Antoine et al., 2016). The obtained K_D of 113 nM for BH296 corresponds with robust accuracy to the K_D previously determined by saturation binding 67 nM. The estimated affinities for BH267.meta are also in good agreement (112 and 72 nM, respectively; Table 3.4) (Jakobowska et al., 2021).

3.3   A comparison of biophysical affinity data and IC$_{50}$ values from functional assays

The results described in this chapter have been published as (Jakobowska et al., 2021). Using the GFP-fusion of PfFNT wt and the fluorescently labelled BH296 as the interaction pair, the FCCS approach was tested on a selection of 26 compounds that had been formerly validated in yeast functional lactate transport assays (Golldack et al., 2017). The HEK293 cell lysates were adjusted to a PfFNT-GFP concentration of 5 nM and combined with BH296-DY647 at a final concentration of 70 nM, corresponding approximately to the previously identified K_D-value of this interaction. Next, 30 µl of the mix was distributed into the wells of a glass-bottom 384 microtiter plate. Subsequently, a dilution series ranging from 10 µM to 10 pM of each test compound was added and incubated at RT for 1 h to allow the interactions to reach equilibrium. The wells were then analyzed by FCCS, K_i values were calculated and compared *via* a scatter plot to the IC$_{50}$ values derived from functional experiments in yeast (Figure 3.23, Table 3.5). Despite yielding slightly different absolute numbers, there was a significant correlation between the two independent assay types with respect to the compound ranking (Jakobowska et al., 2021).
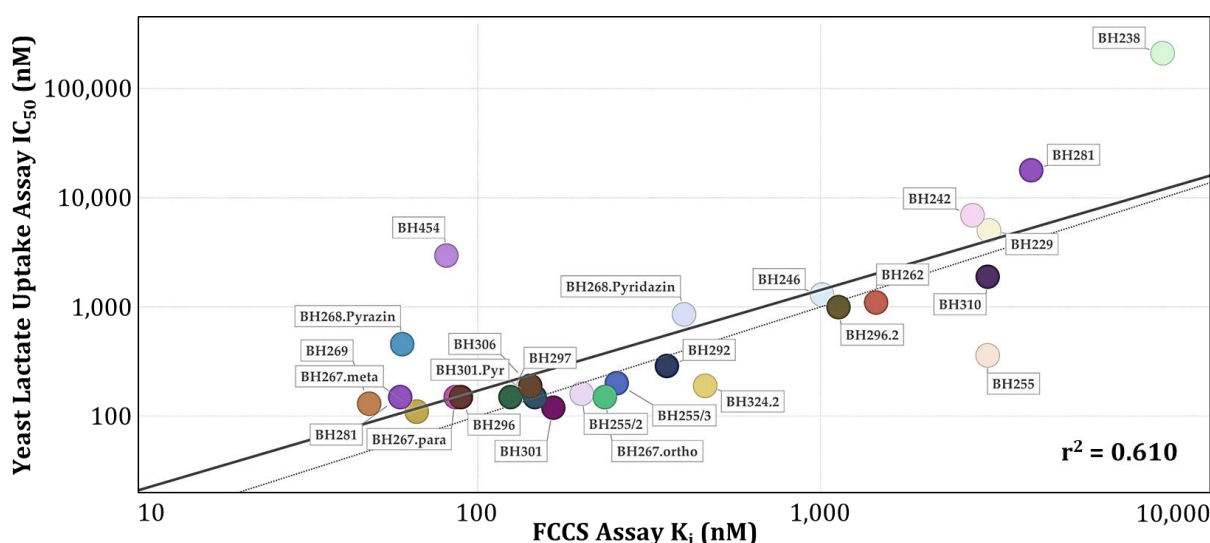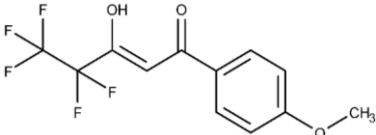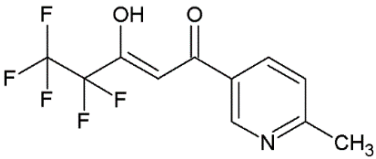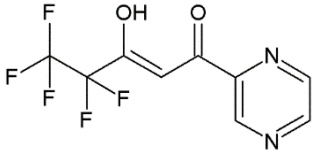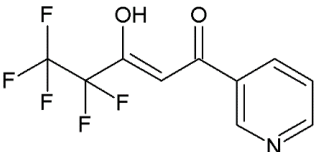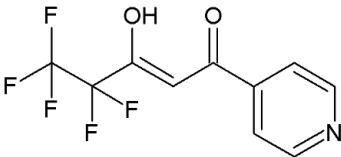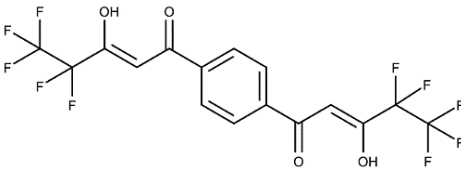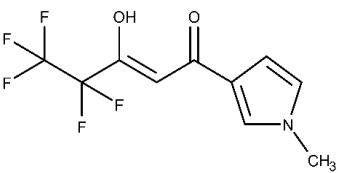

Figure 3.23 Scatter plot of FCCS-derived Ki values vs. IC50-values from the yeast lactate uptake assay. The activity of 26 compounds on the uptake of lactate in the yeast assay (y-axis) was plotted against the Ki values obtained from FCCS competition assays using the PfFNT-GFP and BH296-DY647 (x-axis). The diagonal is displayed as a thin dotted line, while the regression is shown as a thick black line, r2: 0.610 (Jakobowska et al., 2021). The figure is reprinted from (Jakobowska et al., 2021).

The only exception was observed with the compound BH454, which scored an affinity below 100 nM in the FCCS assay but showed limited effectiveness in blocking lactate transport in the yeast-based assay. This outcome could be attributed to the limited
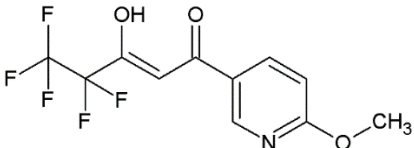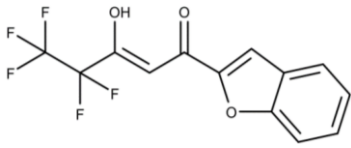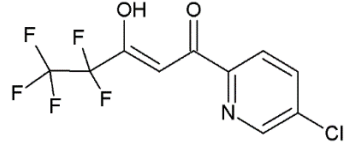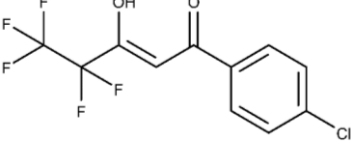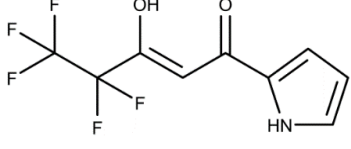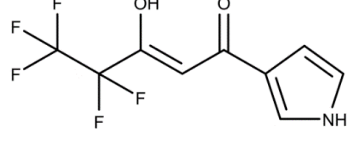
transmembrane diffusion of the comparatively large compound in the yeast system (Table 3.5, No. 6). The derived coefficient (r^2 = 0.6) confirms a correlation between the data obtained from the functional yeast assay and direct interaction measurements. However, the variability in the absolute IC_{50} and 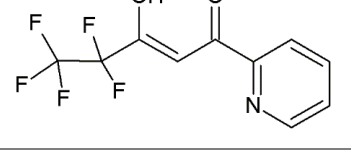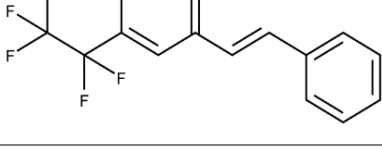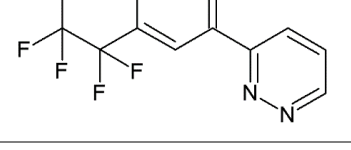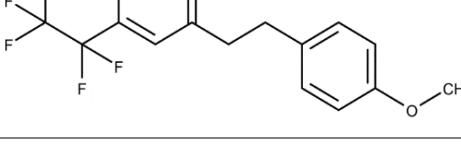K_i values suggests that the cellular assay format is less well-defined because it lacks information on the concentration of active PfFNT, and requires the inhibitor compounds to cross the plasma membrane either by diffusion or *via* transport proteins (Jakobowska et al., 2021).
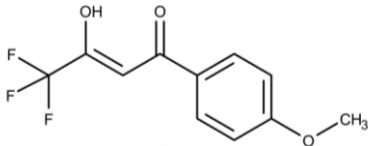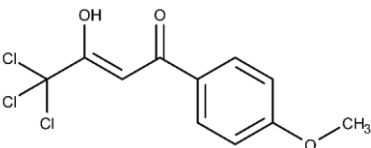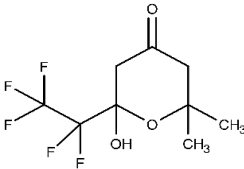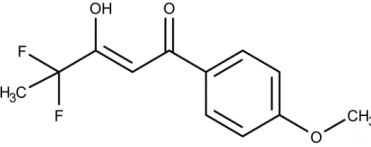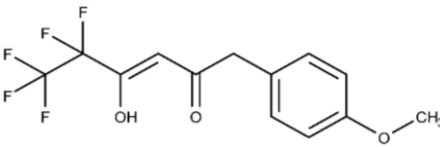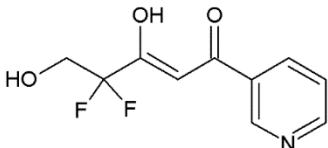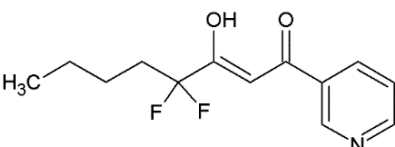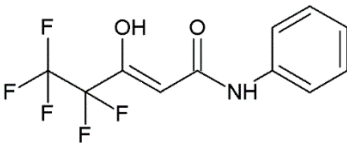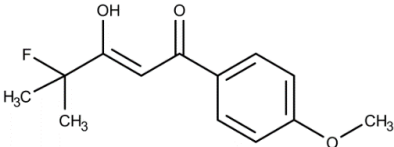
Table 3.5 Comparison of the FCCS-derived K_i values vs. IC_{50}-values from the yeast lactate uptake assay.

No.	Name	Structure	$K_{i\ FCCS}$ (nM)	$IC_{50\ yeast}$ (nM)
1	BH296		48 ± 2	140 ± 10
2	BH281.M		59 ± 18	150 ± 40
3	BH268.Pyrazin		60 ± 16	460 ± 30
4	BH267.meta		66 ± 6	110 ± 10
5	BH267.para		86 ± 20	150 ± 30
6	BH454		80.5 ± 28	3000 ± 100
7	BH269		123 ± 9	130 ± 10

8	BH297		124 ± 18	150 ± 30
9	BH306		142 ± 15	190 ± 10
10	BH301.Pyr		146 ± 19	150 ± 40
11	BH301		166 ± 11	120 ± 10
12	BH255/2		201 ± 17	160 ± 10
13	BH255/3		254 ± 14	200 ± 10
14	BH267.ortho		234 ± 47	150 ± 10
15	BH292		356 ± 79	290 ± 20
16	BH268.Pyridazin		399 ± 71	630 ± 30
17	BH324.2		461 ± 20	190 ± 20

18	BH246		1011 ± 47	1300 ± 200
19	BH296.2		1131 ± 9	1000 ± 100
20	BH262		1457 ± 179	1100 ± 100
21	BH242		2782 ± 69	7000 ± 600
22	BH310		3086 ± 55	1900 ± 300
23	BH229		3111 ± 64	5100 ± 400
24	BH255		3078 ± 97	360 ± 50
25	BH281.A		4131 ± 355	18000 ± 6000
26	BH238		no affinity	214000 ± 23000

3.4   FCCS as a screening tool

Once the reliability of FCCS measurements has been proven, the next step was to evaluate the FCCS approach to drug screening utilizing crude cell lysates as the target protein

source. The underlying idea of this method is based on the competition of candidate drugs to the fluorescent probe-target complexes and the exceptional ability of FCS to differentiate between free fluorescent probes and fluorescent probe-target complexes in solution (Ruan et al., 2015). In this study, a screening of the AnalytiCon NATx library (consisting of 2000 macrocycles displaying an unmatched wealth of structural diversity) was conducted with the goal of identifying novel scaffolds that have the potential to inhibit PfFNT.

3.4.1 Reducing single point data acquisition time

To process a large number of samples in a reasonable amount of time, high-throughput screening (HTS) systems must have short analysis times per sample due to economic constraints (Koltermann et al., 1998; Okun & Veerapandian, 1997; Vogel et al., 2002). Because the assay was intended to be applied to HTS, the effect of shorter acquisition times on the accuracy of fluorescence correlation analyses was investigated. For this, data were acquired with 8 different routines (12 x 8 s; 12 x 5 s; 12 x 3 s; 10 x 8 s; 10 x 5 s; 10 x 3 s; 8 x 5 s; 8 x 3 s) and compared the complex formation in the presence or absence of unlabelled competitor (Figure 3.24). The studies were performed in triplicates.
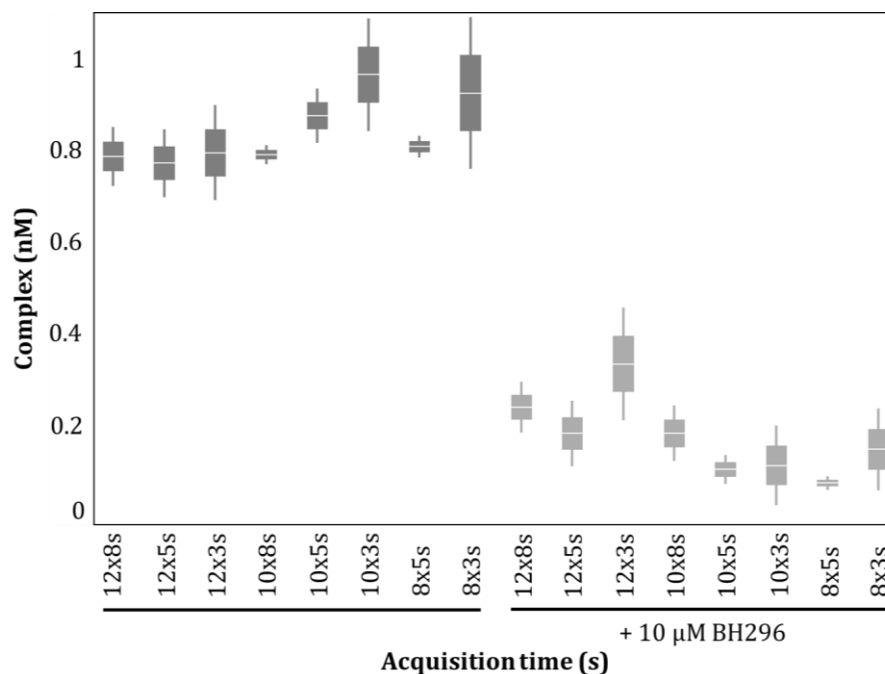
Figure 3.24 Reduction of measurement time to increase throughput for screening campaigns. Complex formation of 5 nM PfFNT wt-GFP and 70 nM BH296-DY647 in the presence or absence of 10 µM unlabelled BH296. Analysis durations ranging from 96 to 24 s were tested.

Cross-correlation curves derived over shorter times were noisier than curves obtained from data taken over longer times, but the typical diffusion times and particle counts

were comparable, indicating that both curves contain essentially the same information. The results clearly indicate that a single measurement of 8 x 3 s, although distributions of determined complex numbers are relatively broad, is sufficient to robustly differentiate between a positive and negative control. With these parameters, a 384-well plate comprising 338 samples can be analyzed within less than 2.5 hours and hence allows for HT Screening for PfFNT inhibitors.

3.4.2 Test plate analysis

To validate the screening set-up, a test plate, containing known inhibitors with varied activity for PfFNT wild type, was assessed prior to the actual screening. For this purpose, PfFNT inhibitors with known K_i values (BH296; BH281.M; BH269; BH296.2; BH267.meta; BH238) were randomly distributed on 384-well plate. As a negative control, 1% DMSO was used. The wells were then measured by FCCS, complex numbers were calculated and compared *via* a heat map (Figure 3.25).

Figure 3.25 Distribution of the inhibitors on the test plate and changes in the complex number as seen by the colour change. The wells with the lowest measured complex number are depicted in blue, while those with the highest complex number are shown in red.

The obtained results show a clear separation between positive and negative samples with an 8 x 3 s acquisition time. Moreover, the compound BH238, which was previously classified as not active, in this test also did not bind the PfFNT within the detection limits of the instrument used. The results were also robust towards the variation of incubation

times of the lysates before or after the addition of compounds, which is important for screening large numbers of samples.

3.4.3 FCCS screening of 2000 compounds

For single-point measurements, solubilized cell membranes containing PfFNT wt-GFP at a concentration of 5 nM were pre-mixed with 70 nM BH296-DY647 and distributed as 30 μl aliquots into 384-well plate cavities. Then, 0.3 μl of compounds and controls were transferred in an automated process to a measurement plate for the final 10 μM concentration within the assay. DMSO and BH296 were used as negative and positive controls, respectively. After mixing and 1 h incubation at room temperature, FCCS measurements were performed by monitoring each sample 8 times for 3 s. The results of screening a library containing 2000 compounds are depicted in Figure 3.26 and 3.27.
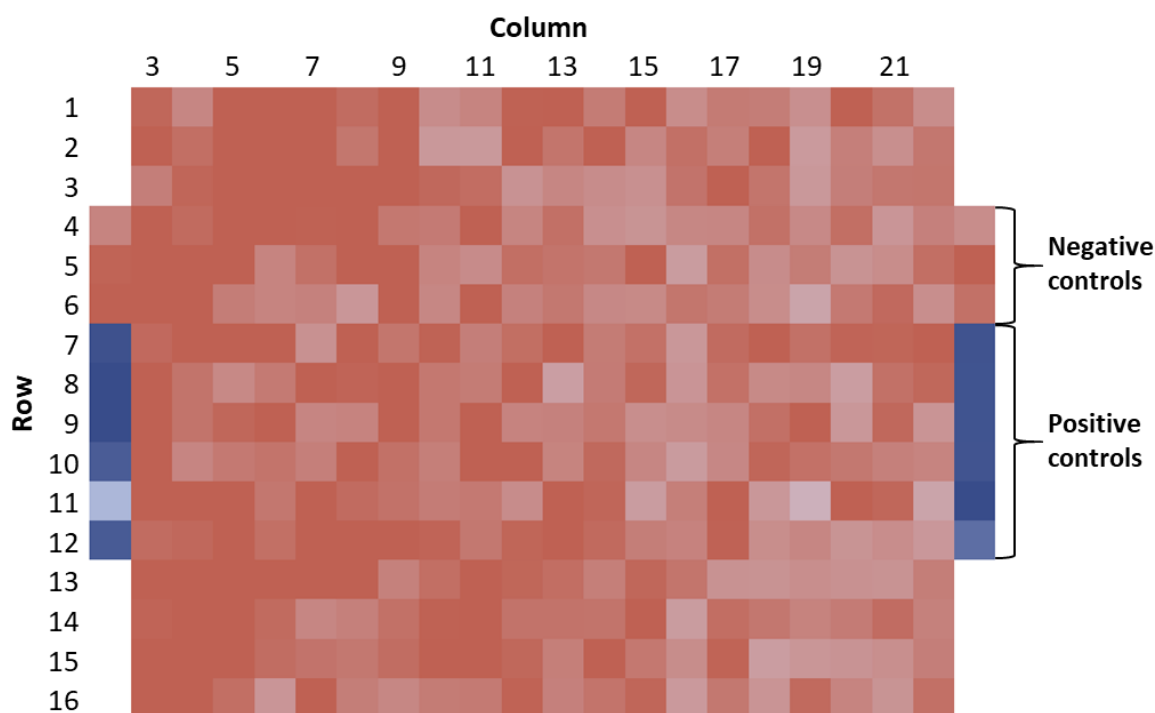
Figure 3.26 Representative heat map generated for one of the seven screening plates, reflecting changes in the complex number depending on the added inhibitor. The wells with the lowest measured complex number are depicted in blue, while those with the highest complex number are shown in red. Columns 2 and 23 contain three negative controls (DMSO) and six positive controls (BH296).

Inhibition by compounds was judged *via* the reduction of cross-correlation amplitude. As demonstrated earlier, if a compound has an inhibitory effect on PfFNT, the cross-correlation amplitude should decrease (Mikuni et al., 2015). In contrast, if the compound has no effect on PfFNT, the cross-correlation amplitude should remain high (Antoine et al., 2016; Jakobowska et al., 2021; Mikuni et al., 2015). Additionally, the use of filters

helped to improve the precision of screening by excluding irrelevant data, such as unexpected aggregation (Mikuni et al., 2015). Any increase in intensity exceeding 20% from the control (DMSO solution) average intensity resulted in exclusion from the study.
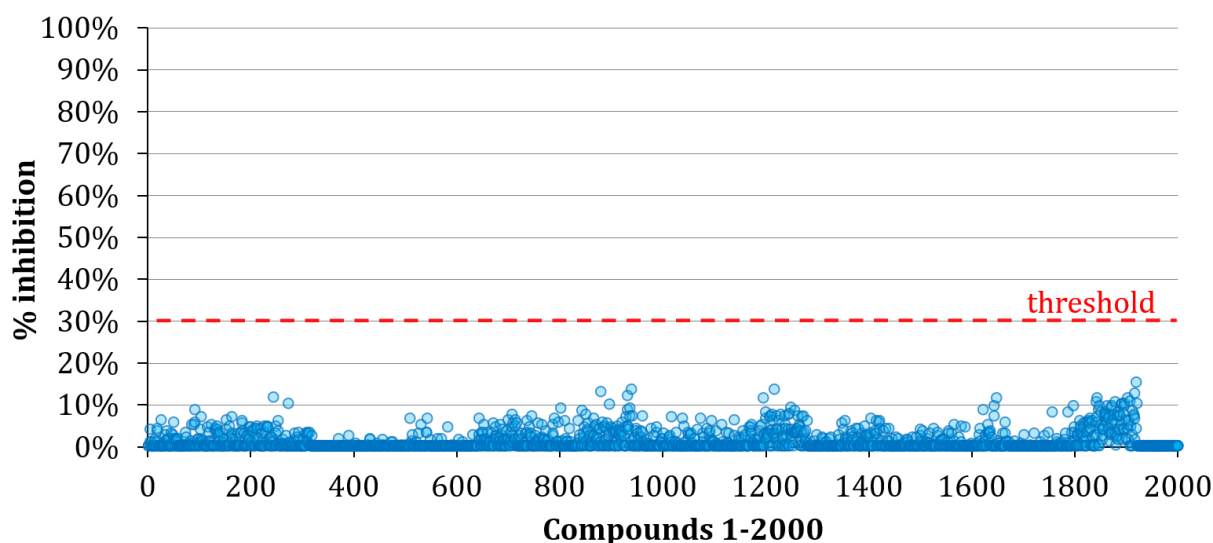
Figure 3.27 Screening results as percent inhibition of PfFNT wt-GFP BH296-DY647 interaction at 10 μM inhibitor concentration. A compound bank of 2000 inhibitors was screened at 10 μM to identify compounds that interfere with the binding of the receptor to the ligand. The threshold for positive candidates at 30% inhibition.

In the first round of FCCS screening, no candidate with an inhibitory effect greater than 30% was identified, therefore, none of the tested compounds was categorized as a "Hit". These results suggest that a very specific ligand is required to block the PfFNT channel and highlight an effective screening approach to identify compounds as no false-positive hits were found.

3.5 Alternative approaches for discovering novel PfFNT inhibitors

FCCS screening only allows the search for new inhibitors that displace the existing inhibitor, i.e., share the same binding pocket. In Chapters 3.1.3 and 3.1.5, it was shown that the PfFNT inhibitors, BH296 and BH267.meta, bind to the intracellular side of the transporter. Targeting intracellular proteins is often challenging because to reach the cytosol, molecules must first traverse the cell membrane (Yang & Hinner, 2015). Moreover, the parasite's cytoplasm is protected by three membranes, as seen in Figure 1.5, thus the drug has to pass through two additional membranes. Therefore, finding an inhibitor that binds to the channel's extracellular side is a more preferable choice. Other than the affinity-based screening, the upcoming assay was a functional screen – based on the inhibition of the function of the PfFNT transporter. The starting point of the study was the fact that an anti-hypertensive drug Syrosingopine is synthetically lethal with an anti-

diabetic drug Metformin and that both compounds interact synergistically to kill a wide range of cancer cell types while showing no activity against non-transformed cells (Benjamin et al., 2016; Benjamin et al., 2018; Medeiros, 2022). The energetic demands of cancer cells are high due to their accelerated growth and elevated metabolic needs (Benjamin et al., 2016; Benjamin et al., 2018; Khammanivong et al., 2020; Potter et al., 2016). To keep the energy-generating machinery running, the molecule NAD^+ (nicotinamide adenine dinucleotide), which is essential for converting nutrients into energy, must be continuously generated from NADH (Benjamin et al., 2016; Benjamin et al., 2018). Both, Metformin and Syrosingopine inhibit NAD^+ regeneration, however in two different ways (Benjamin et al., 2018). Many cancer cells switch their metabolism towards glycolysis, which means that they mainly generate energy by converting glucose to lactate (Potter et al., 2016). Tumour cells get rid of lactate by exporting it from the cell *via* specific transporters since a build-up causes a blockage of the glycolytic pathway (Benjamin et al., 2016; Benjamin et al., 2018; Khammanivong et al., 2020; Todenhöfer et al., 2018). Syrosingopine efficiently inhibits the two most important lactate transporters, MCT1 and MCT4 (Benjamin et al., 2016; Benjamin et al., 2018). Lactate dehydrogenase (LDH) inhibition due to increased intracellular lactate levels caused by Syrosingopine's blockage of lactate efflux decreases the NAD^+/NADH ratio, leading to loss of glycolytic adenosine 5′-triphosphate (ATP) production (Benjamin et al., 2018; Medeiros, 2022). Metformin blocks the second of the two cellular pathways for NAD^+ regeneration, mitochondrial respiration, leading to decreased ATP levels (Benjamin et al., 2016; Benjamin et al., 2018). The resulting activation of adenosine 5'-mono-phosphate-activated protein kinase (AMPK) inhibits the mammalian target of rapamycin complex 1 (mTORC1), a critical signaling hub for cell proliferation, translation, and metabolism (Chae et al., 2016; Medeiros, 2022; Oliveira et al., 2021; Owen et al., 2000; Pollak, 2012; Rena et al., 2017). The depletion of NAD^+, due to combined Metformin-Syrosingopine treatment, leads to cell death since the cancer cells are no longer able to produce sufficient energy (Benjamin et al., 2018; Saraei et al., 2019).

In light of the information presented above, the idea arose to functionally replace the MCT-transporters with *Plasmodium falciparum* formate-nitrite transporter, see Figure 3.28. The basic assumption was that the cells expressing PfFNT treated with Syrosingopine and Metformin would not die, as lactate would continue to be exported outside the cell *via* the PfFNT channel (Figure 3.28A). In contrast, in the presence of a

PfFNT-specific inhibitor, all lactate export pathways would again be blocked, resulting in blockage of the glycolytic pathway and subsequent cell death (Figure 3.28B). If the proposed theory is accurate, it might be successfully applied in the search for novel PfFNT inhibitors with a different binding site. To evaluate the reliability of this concept, two assays have been established; in HEK293 cells expressing PfFNT intracellular lactate accumulation and acidification were measured in the presence of Syrosingopine and the PfFNT inhibitor - BH296 (Chapter 3.5.1) and afterwards, it was examined how the cells respond to the combined Metformin/Syrosingopine treatment in the presence and absence of BH296 (Chapter 3.5.2).
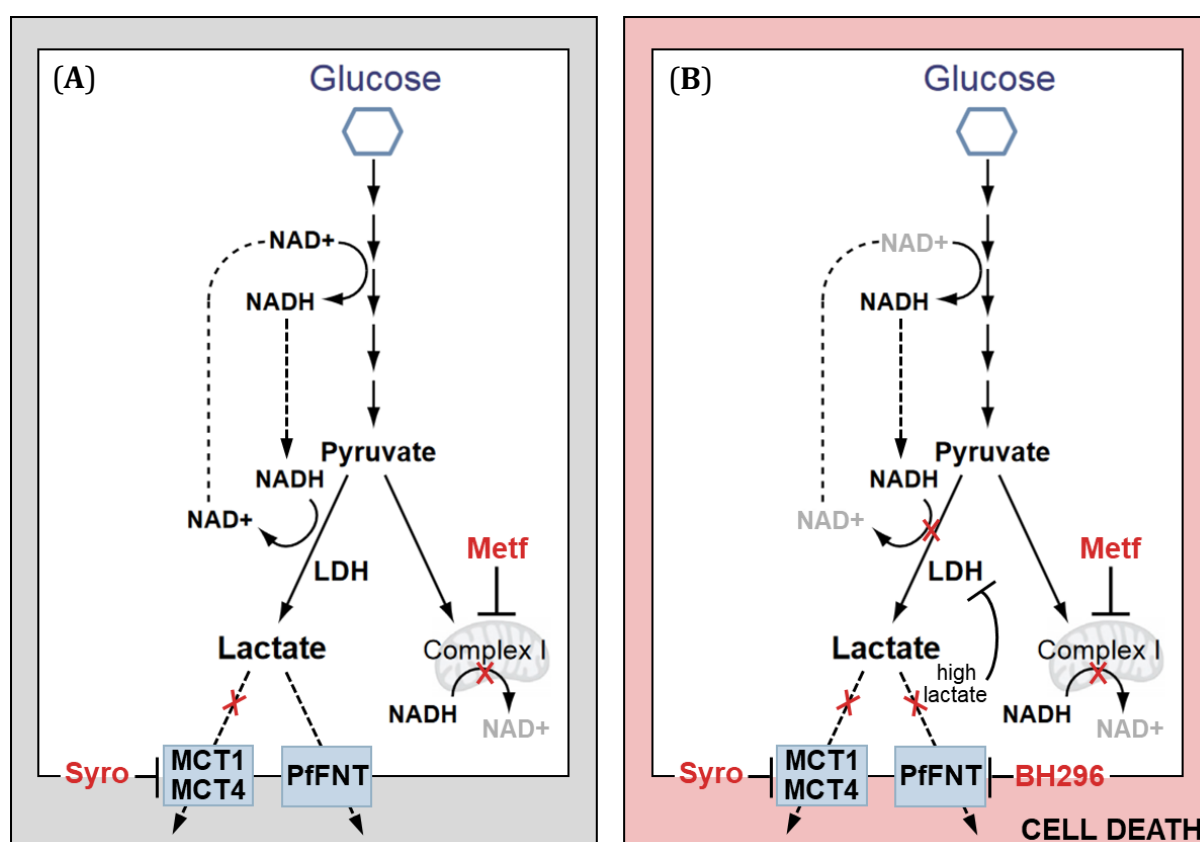
Figure 3.28 A diagram outlining the cellular screening concept (**A**) Combined Metformin (Met)/Syrosingopine (Syro) treatment does not induce cell death in PfFNT-expressing cells because lactate is transported outside the cell *via* the PfFNT channel. NAD+ required for glycolysis can still be regenerated. (**B**) Cell death is observed when PfFNT is blocked with a specific inhibitor, such as BH296, since the cell's ability to recycle NAD+ is then completely lost. The figure is adapted from (Benjamin et al., 2018).

3.5.1 Intracellular pH detection

Next, it was set out to reconfirm the activity of Syrosingopine and the pH dependent readout with a novel fluorogenic probe pHrodo™ Red AM Intracellular pH Indicator, according to the manufacturer's instructions, see Chapter 2.2.8 and Figure 3.29

(Benjamin et al., 2018). pHrodo quantifies cytosolic pH in the range of 9 to 4 with a pKa of ~6.5 (Benjamin et al., 2018). The dye is weakly fluorescent at neutral pH but increasingly fluorescent (560/585 nm Ex/Em) as the pH drops (Benjamin et al., 2018). Briefly, HEK293 cells and HEK293 cells expressing PfFNT were seeded at an initial density of 100,000 cells/ml, and Syrosingopine/BH296 were added at a concentration of 10 μM. The cells were then incubated with compounds for 3 hours at 37°C, washed with HBSS, HEPES 20 mM and labelled with pHrodo™ Red AM dye. After 30 minutes, the cells were washed again with HBSS, HEPES 20 mM and then the cell fluorescence was measured at 560/585 nm Ex/Em using LSM 510 ConfoCor 2.

Seed cells (96-well plate)

Drug treatment (3 h at 37°C)

Wash cells with HBSS, HEPES 20 mM

Add pHrodo™ Red AM to cells and incubate at 37°C for 30 min

<u>pH indication</u>
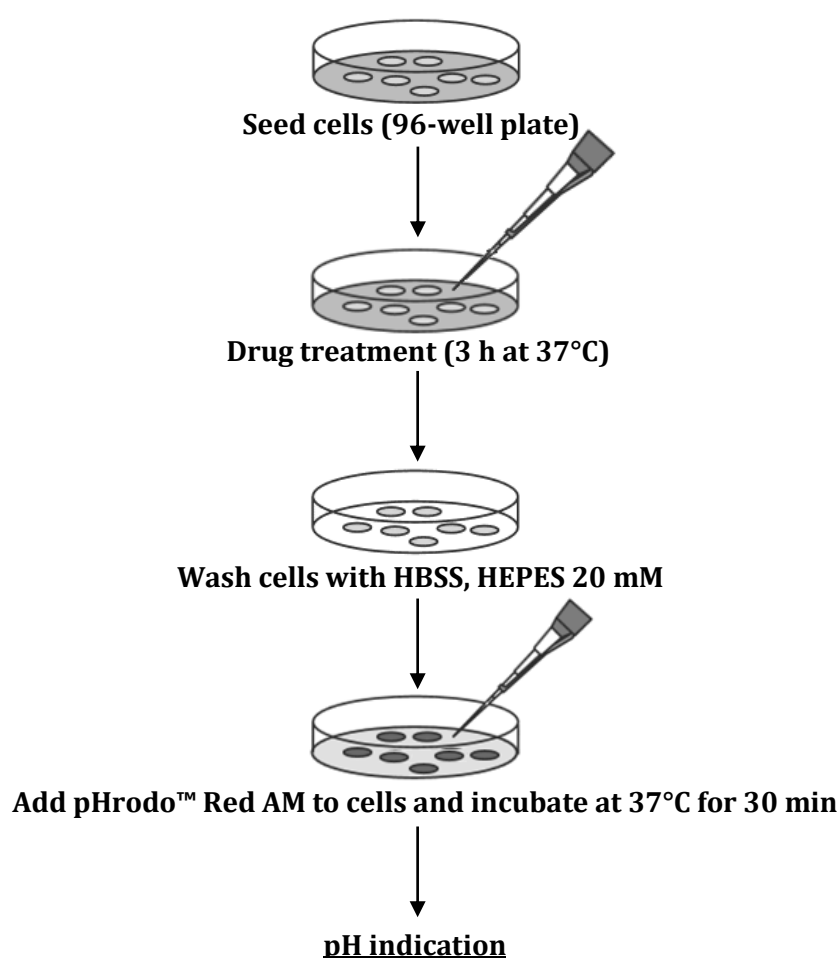
Figure 3.29 Workflow for intracellular pH detection.

Washing the cells, however, created difficulties as human embryonic kidney cells tend to come off the surface with a little agitation, even without trypsin. To enhance cell attachment, the plates on which the cells were seeded were coated with 5 μg/cm^2 collagen. Collagen, found in most tissues and organs, holds cells and tissues together and has been recognized as a useful matrix in cell culture (Hashimoto et al., 2019; Somaiah et

al., 2015). As expected, collagen improved cell adherence and growth and therefore collagen-coated plates were used for all further experiments where there was a risk of cells washout.

PfFNT wt   HEK293
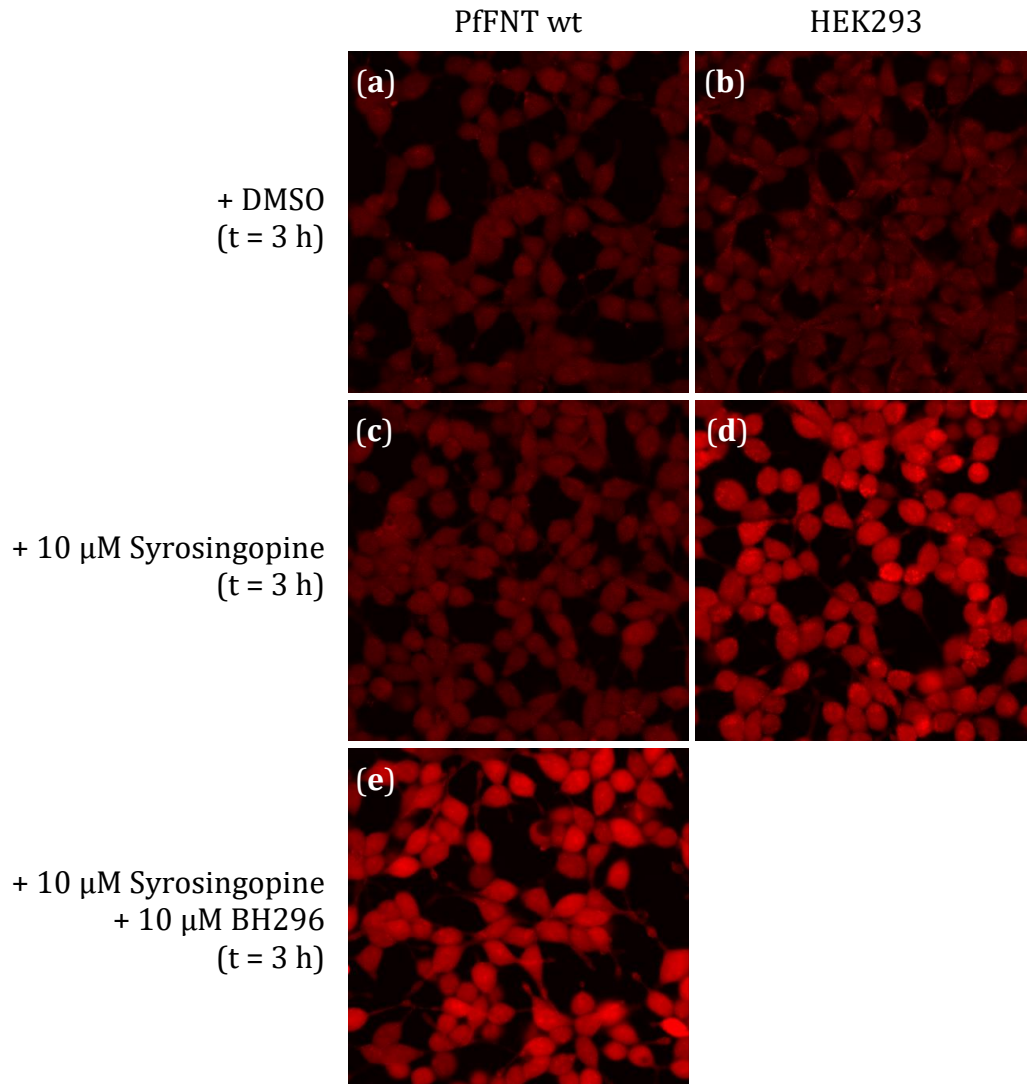
Figure 3.30 Intracellular pH in drug-treated (10 µM, 3 h) cells stained with pHrodo. Exposure of HEK293 cells to Syrosingopine led to a decrease in the intracellular pH (**D**), as can be seen by the increased intensity of the fluorescent dye in comparison with the DMSO negative control (**B**). Expression of PfFNT rescued acidification in HEK293 cells (**C**, **A**). Blockage of MCT1, MCT4 and PfFNT led to acidification of HEK293 cells expressing PfFNT (**E**).

Due to MCT1 and MCT4 inhibition, exposure to Syrosingopine induced a significant reduction in the intracellular pH in HEK293 cells (Figure 3.30D). This can be observed by the enhanced intensity of the fluorescent dye in comparison with the DMSO negative control (Figure 3.30B). In contrast, in HEK293 cells expressing PfFNT the inhibition of the monocarboxylate transporters did not significantly increase intracellular lactate levels, suggesting that the excess lactate produced by enhanced glycolysis is predominantly exported from the cell (Figure 3.30C and 3.30A) (Benjamin et al., 2018). Treatment with

the PfFNT-specific inhibitor, BH296, blocked lactate efflux and caused an increase in intracellular pH, thus validating the assay (Figure 3.30E). Furthermore, the above results demonstrated that PfFNT rescues the inhibition of MCTs, proving that the PfFNT expressed in human embryonic kidney cells is functional.
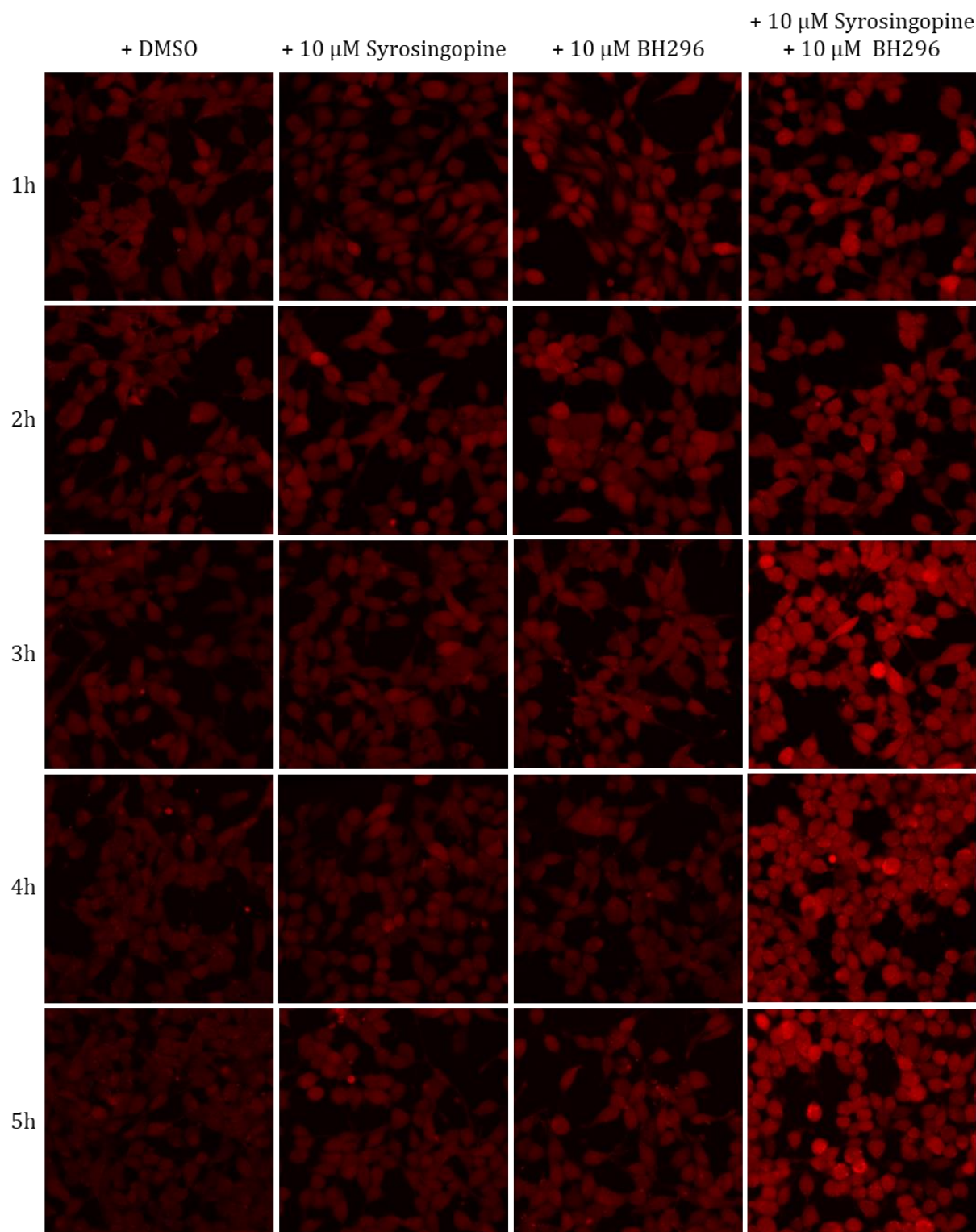
Figure 3.31 Intracellular lactate accumulation in HEK293 cells expressing PfFNT treated with indicated drugs, measured at different incubation times.

Next, the impact of the compounds' incubation time on intracellular acidification in cells expressing PfFNT was investigated. Intracellular acidification resulting from lactate buildup was detectable 3 hours after the addition of Syrosingopine and BH296 (Figure 3.31). Prolonged incubation (more than 3 hours) did not significantly alter the intensity of the fluorescent dye. Since Syrosingopine or BH296 treatment is only cytostatic, the accumulation of intracellular lactate does not result in cell death (Benjamin et al., 2018).

3.5.2   Synthetic lethality between Syrosingopine and Metformin

Since a live/dead readout is a simpler approach for screening, afterwards, cells were tested for responsiveness to the combination of Syrosingopine with Metformin.

0 h   **24 h**   **48 h**   **120 h**

HEK293 + DMSO

HEK293 + 10 µM Syrosingopine + 4 mM Metformin

PfFNT wt + 10 µM Syrosingopine + 4 mM Metformin
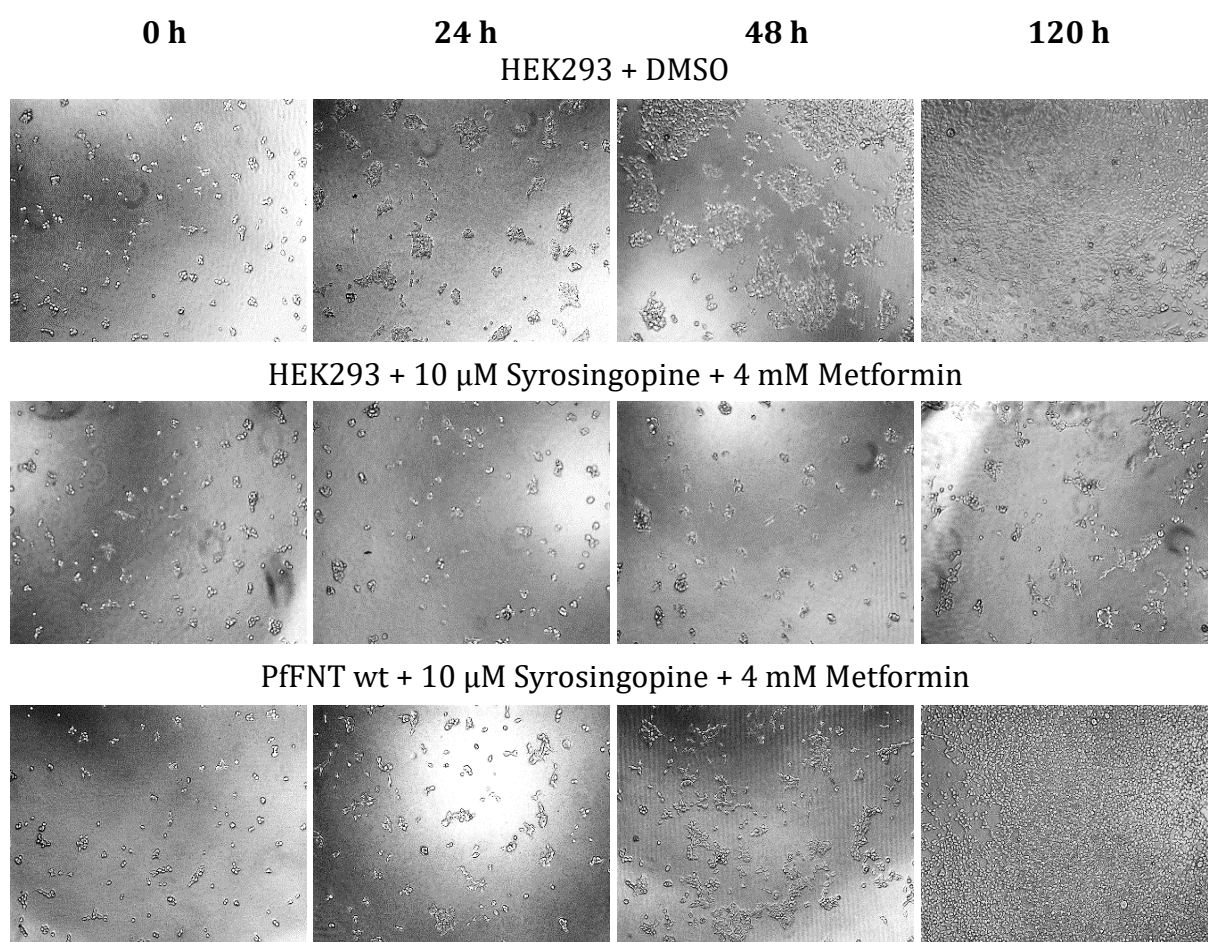
Figure 3.32 Micrographs of HEK293 cells and HEK293 cells expressing PfFNT treated with Syrosingopine (10 µM) and Metformin (4 mM). Normal cell growth (top panel). Inhibition of MCTs and inhibition of the Complex I of the mitochondrial respiratory chain is synthetically lethal (central panel) (Benjamin et al., 2016). Expression of PfFNT rescue cell kill (bottom panel).

For this reason, HEK293 cells and HEK293 cells expressing PfFNT were plated in 96-well microtiter plates at a density of 1000 cells/well. Subsequently, Syrosingopine and Metformin were added at a concentration of 10 µM and 4 mM, respectively. The

compounds were utilized at concentrations that had a negligible impact on cell growth. The cells were then incubated with the compounds for 5 days at 37°C, and images were taken after 0 h, 24 h, 48 h and 120 h using a Zeiss Axio Vert.A1 light microscope (10x magnification) to monitor cell survival.
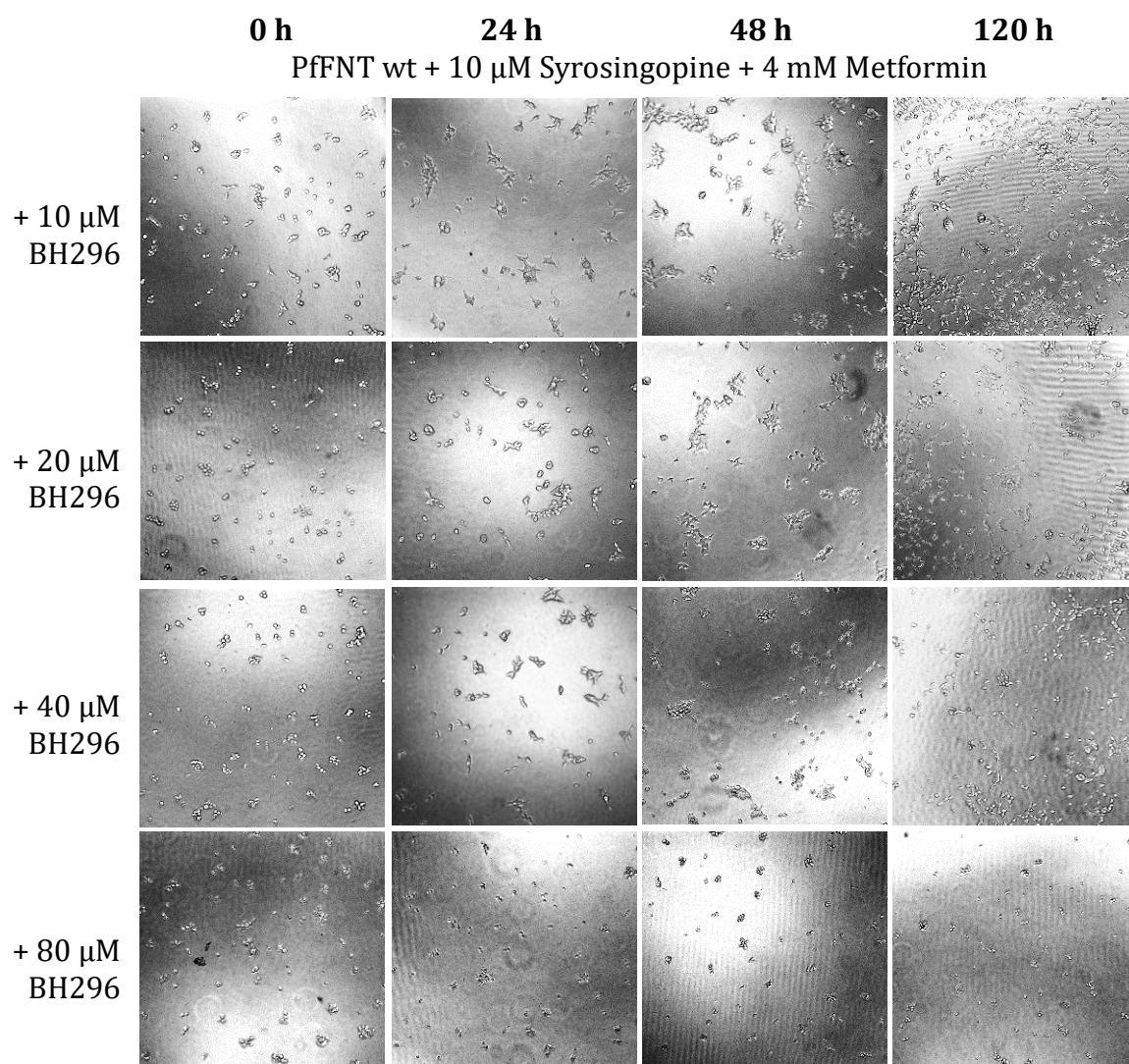
Figure 3.33 Block of PfFNT with BH296 will kill rescued cells in a dose-dependent manner. Micrographs of HEK293 cell expressing PfFNT treated with Syrosingopine (10 µM), Metformin (4 mM) and different concentrations of PfFNT inhibitor BH296 (10, 20, 40, 80 µM).

The Syrosingopine-Metformin combination, when administered in a low, sub-lethal concentration, was able to induce cell death in HEK293 cells, as illustrated in Figure 3.32. This finding supports the notion that the combined inhibition of monocarboxylate transporters (MCT1, MCT4) and the Complex I of the mitochondrial respiratory chain is an essential prerequisite for triggering cell death (Benjamin et al., 2016; Benjamin et al., 2018; Medeiros, 2022). The mode of cell death occurred *via* induction of apoptosis (Benjamin et al., 2016). In contrast, Syrosingopine had no effect on the growth or survival

of HEK293 cells expressing PfFNT even in the presence of Metformin, thereby confirming that generated lactate is exported out of the cell and NAD$^+$ required for glycolysis can still be regenerated (Benjamin et al., 2016). Moreover, it also reconfirms the ability of PfFNT to rescue the phenotype. The next step was to check whether blocking the PfFNT transporter would restore the elicited Syrosingopine-Metformin synthetic lethality. To identify the lowest effective concentration of PfFNT inhibitor needed for cell killing *in vitro*, HEK293 cells expressing PfFNT were treated with increasing concentrations of BH296 (10, 20, 40, 80 µM) in the presence of Metformin (4 mM) and Syrosingopine (10 µM). As depicted in Figure 3.33, titrating of BH296 resulted in a dose-dependent increase in cell killing. In order to verify whether the cell death was due to the blockade of PfFNT or perhaps to the toxicity of the compound resulting from excessive applied concentration, BH296 was also added to cells where PfFNT is not expressed. HEK293 cells proliferation was unaffected by 10 µM BH296, higher concentrations (20, 40 µM) of the compound inhibited cell growth, whereas a concentration of 80 µM was toxic and caused cell death, see Figure 3.34. Taken together, these findings indicate that BH296 at a concentration of 10 µM is not toxic to cells, blocks the PfFNT channel and restores Syrosingopine-Metformin synthetic lethality.

+ 10 µM BH296   **+ 20 µM BH296**   **+ 40 µM BH296**   **+ 80 µM BH296**

HEK293

HEK293 + 4 mM Metformin
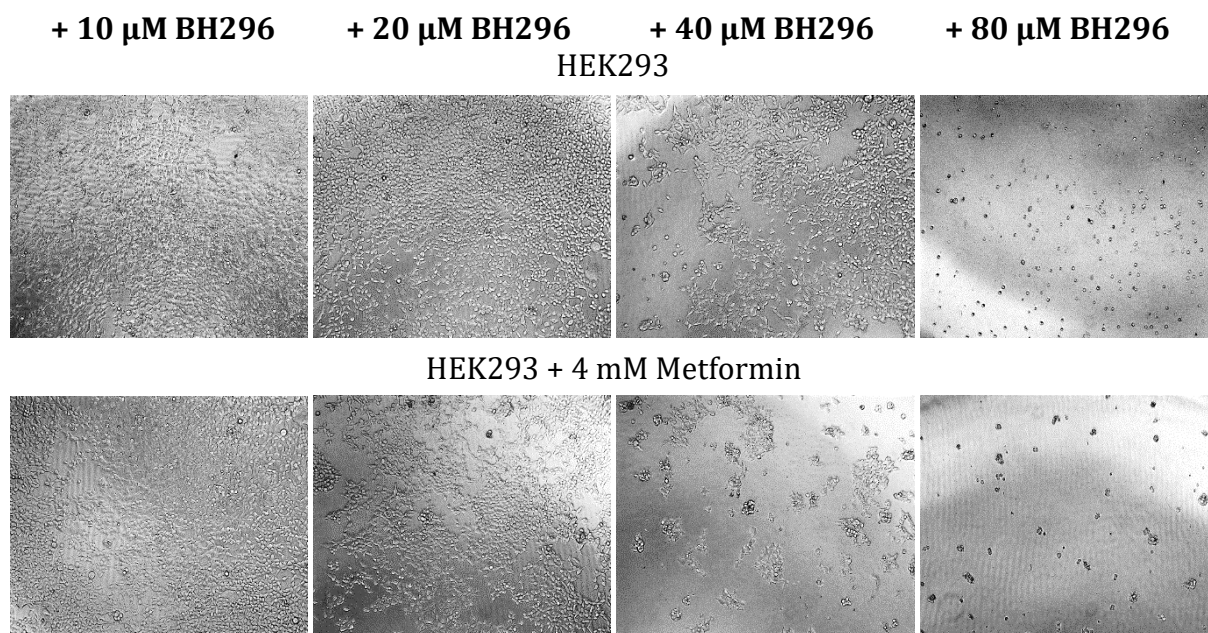
Figure 3.34 Cell killing effect of BH296. Proliferation of HEK293 cells titrated with BH296 in the presence/absence of 4 mM Metformin. Pictures of cells were taken after 120 h of treatment with indicated compounds.

To sum up, the above results suggest that it is possible to functionally replace MCTs with *Plasmodium falciparum* formate-nitrite transporter. In cells where PfFNT is expressed,

synthetic lethality between Syrosingopine and Metformin is lost, but blockade of PfFNT by the specific inhibitor, BH296, can restore the elicited lethality. Thus, the obtained results are in line with the assumptions made, nevertheless, the observed cell-killing effect is not as strong as expected and several cells are still able to survive treatment with Syrogingopine and Metformin (see Figure 3.32, HEK cells after 120 h of incubation). The explanation for this may be that Syrosingopine is around 60-fold more potent against MCT4 (half maximal inhibitory concentration IC_{50} ~40 nM) than MCT1 (IC_{50} ~2500 nM) (Benjamin et al., 2018). However, it is reported in the literature (Li et al., 2021) that the HEK293 cell line used in all experiments does not express the MCT4 transporter.
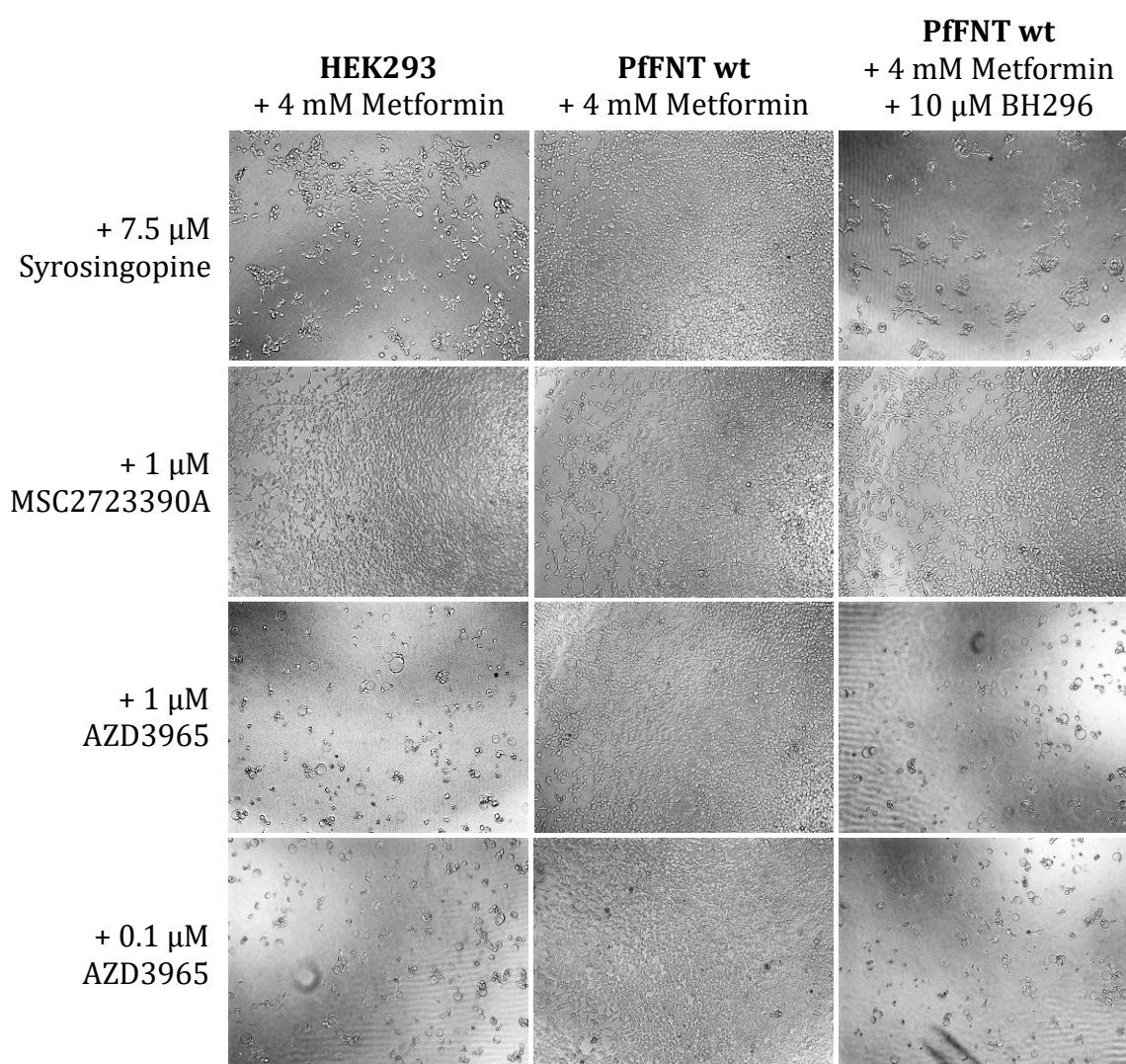
Figure 3.35 Test of other MCT-inhibitors. In order to improve the assay other known monocarboxylate transporter inhibitors have been tested; a MCT4-specific inhibitor MSC2723390A1 at a concentration of 1 μM and a MCT1-specific inhibitor AZD3965 at a concentration of 0.1 and 1 μM. The column on the left shows HEK293 cells in the presence of 4 mM Metformin, the column in the middle HEK293 cells expressing PfFNT also in the presence of 4 mM Metformin, while the column on the right shows HEK293 cells expressing PfFNT with Metformin (4 mM) and 10 μM of BH296 added.

To confirm this, two other inhibitors with potency only against one monocarboxylate transporter were used instead of Syrosingopine; a MCT1 specific inhibitor AZD3965 (IC_{50} ~1.6 nM) (Guan & Morris, 2020) and a MCT4 specific inhibitor MSC2723390A1 (IC_{50} ~77 nM) (Heinrich et al., 2021). As expected, the absence of the drug target prevented the MCT4-specific inhibitor MSC2723390A1 from affecting lactate efflux and lethality could not be induced with the addition of Metformin (Figure 3.35) (Benjamin et al., 2018). In contrast, treatment with small molecule inhibitor AZD3965 slowed lactate efflux, thus demonstrating that this compound inhibits MCT1 and that this transporter is expressed in the HEK293 cell line. The drawback of targeting MCT1 specifically is that its efficacy diminishes when MCT4 is present. This presents a considerable obstacle since hypoxia induces MCT4 expression in the majority of tumors (Benjamin et al., 2018; Polański et al., 2014). However, for the purposes of this experiment, where only HEK293 cells are used, the use of the AZD3965 inhibitor seems to be a great improvement. Therefore, AZD3965 at a concentration of 0.1 μM was used for all further tests.

3.5.3 Metformin synthetic lethal drug screen

Given the promising results obtained during the tests outlined in the previous paragraph, it was decided to create an assay that allows searching for new compounds that block the PfFNT transporter. The starting point was the observation that treatment of HEK293 cells expressing PfFNT with the MCTs inhibitor (Syrosingopine/AZD3965), the oxidative phosphorylation inhibitor (Metformin) and the specific PfFNT inhibitor (BH296) leads to their death. However, in the absence of BH296, cell death does not occur. This gave an idea of screening a drug library to identify compounds that, like BH296, block the transport of lactate out of the cell and cause cell death. For this purpose, HEK293 cells expressing PfFNT were plated at a density of 1000 cells/well in 96-well plates. Subsequently, AZD3965 and Metformin were added at a concentration of 0.1 μM and 4 mM, respectively. In order to exclude false-positive hits that cause cell death due to the compound's toxicity, replica plates were set up in parallel, containing HEK293 cells not expressing PfFNT, treated only with 4 mM Metformin. The plates were then challenged with 22,000 drugs (20,000 ChemDiv library + 2000 AnalytiCon NATx library tested earlier with FCCS) at a concentration of 30 μM. Cell death was assessed after 5 days of incubation with compounds by monitoring the colour change of the cell culture media. In a cell culture medium, phenol red acts as a visual pH indicator. Phenol red has an end point at pH 7.3–7.4, where it is red and a slight decrease in pH (7–7.1) turns it to yellow.
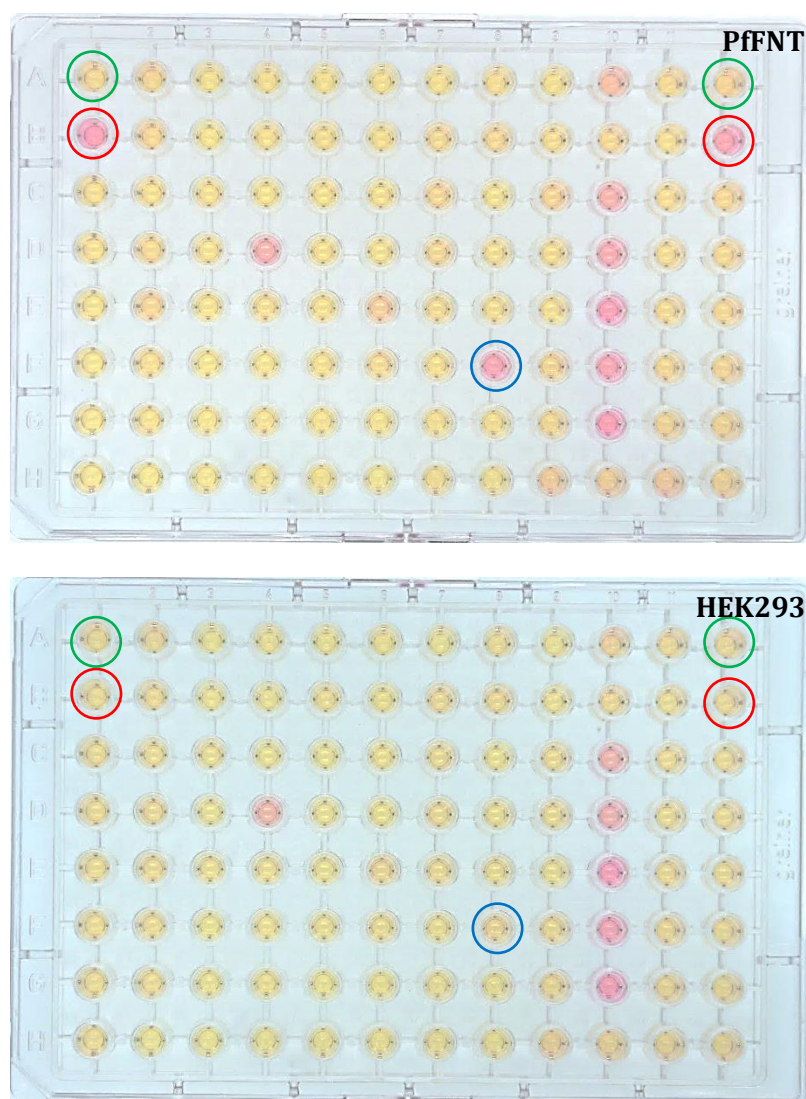
Figure 3.36 Colour change in cell culture media after 5 days of incubation with compounds. The upper panel shows a plate containing HEK293 cells expressing PfFNT treated with 4 mM Metformin, 0.1 μM AZD3965 and the test compounds at a concentration of 30 μM. The lower panel shows a plate of HEK293 cells treated with 4 mM Metformin and the test compounds at a concentration of 30 μM. Negative controls are marked in green, positive controls in red, while the identified hit is marked in blue.

During cell growth, the medium changes colour as pH is changed due to the metabolites released by the cells (Dubey et al., 2021; Morgan et al., 2019). In other words, if the growth of the cells is not inhibited in any way, then after a certain period of time the cell culture media colour will turn yellow. On the other hand, the media will stay red if cell proliferation is interrupted or cell death occurs. An example of a screening plate can be seen in Figure 3.36. In each plate, there is a negative control in positions A1 and A12 (marked green) and a positive control in positions B1 and B12 (marked red). As a positive control, the cells were treated with 10 μM BH296, whereas no drug was added to the negative control.

Figure 3.37 Hits obtained after screening of 22,000 drugs. Grey colour indicates compounds that caused a decrease in intracellular pH in the test with pHrodo.

Figure 3.36 also shows an example of a positive hit (highlighted in blue), where the media remained red in the plate where the HEK293 cells express PfFNT but have changed colour in the plate where the cells do not express PfFNT. In the third column from the right cytotoxic compounds may be observed that killed or strongly reduced proliferation in both, HEK293 cells expressing and not expressing PfFNT. Overall, after the screening of 22,000 drugs, 357 positive hits were obtained (hit rate 1.6%). All positive hits came from the ChemDiv library; no hits were extracted from the AnalytiCon NATx library.
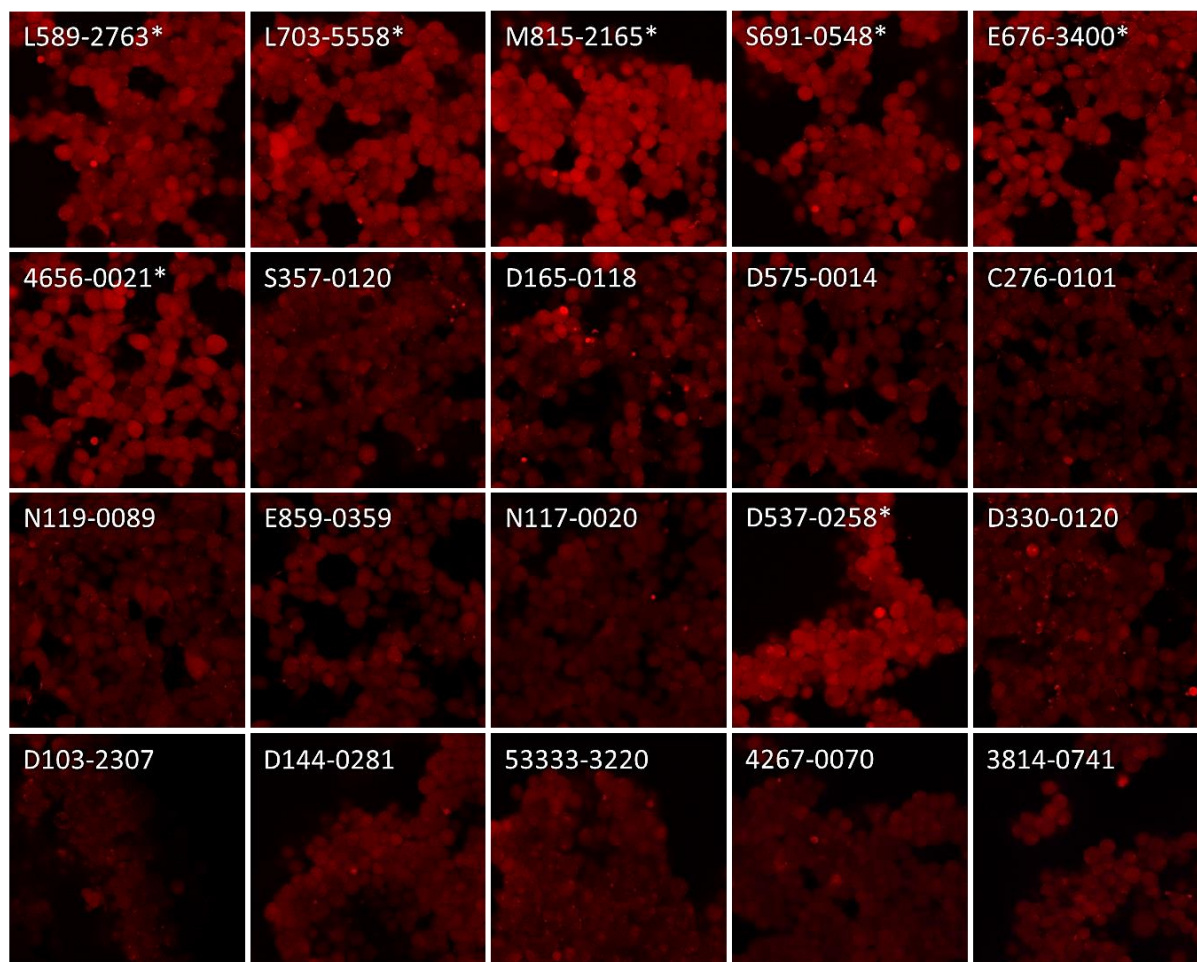
Figure 3.38 Intracellular lactate accumulation in HEK293 cells expressing PfFNT incubated for 3 hours with AZD3965 (0.1 μM) and screening hits (30 μM). 7 of the 20 compounds caused an increase in intracellular pH. These compounds have been marked with (*). The structural formulas of the drugs are shown in Figure 3.37.

The positive hits were reassembled on a single plate and tested once again at the same concentration (30 μM). Only 20 of the 357 hits could, however, be reconfirmed. In Figure 3.37, the structures of the compounds are shown. The false-positive results were most likely caused by technical issues. By looking at several wells under the microscope, it could be seen that the cells sometimes do not grow in the center, but only on the sides of

the well. This may be due to the fact that DMSO, in which the test compounds were dissolved, did not mix properly with the medium after being added by the pipetting robot. It is suspected that DMSO droplet, as it is heavier than DMEM, settles to the bottom of the well, preventing cell growth, and thus generating false-positive findings. This technical problem may have produced false-positive, but not false-negative results, which is why the obtained 20 hits are considered reliable. The compounds were then tested for lactate accumulation using the fluorogenic probe pHrodo™ Red AM (Figure 3.38), as described earlier in Chapters 2.2.8 and 3.5.1. Of the 20 hits previously identified, only 7 induced a significant reduction in intracellular pH, seen as an increase in fluorescent dye intensity (these compounds are highlighted in grey in Figure 3.37).

4 Discussion

4.1 Choosing the optimal expression system for PfFNT

To investigate the functionality, transport mechanism, and pharmacological properties of transmembrane transport proteins, an appropriate system that either endogenously expresses or allows heterologous expression of the target protein is required. The *Plasmodium falciparum* formate-nitrite transporter has been successfully expressed in a diverse range of systems, including *Xenopus laevis* oocytes (Hapuarachchi et al., 2017), Sf9 insect cells (Peng et al., 2021), human embryonic kidney 293 cells (Lyu et al., 2021), yeast, such as *Saccharomyces cerevisiae* (Wu et al., 2015) and *Pichia pastoris* (Hajek et al., 2019) or by employing cell-free protein synthesis (Holm-Bertelsen et al., 2016). Each protein expression system has its own unique advantages and disadvantages, e.g., ease of use, cost, and protein yield, as well as the ability to produce specific protein properties like post-translational modifications (Geisse et al., 1996; Kesidis et al., 2020; Khan, 2013). The choice of expression method is typically based on the specific requirements of the experiment or application.

In the Beitz lab, the yeast system, specifically the baker's yeast *Saccharomyces cerevisiae*, has mainly been used for PfFNT production (Bader & Beitz, 2020; Golldack et al., 2017; Walloch et al., 2021; Walloch et al., 2020; Wiechert & Beitz, 2017b; Wu et al., 2015). *S. cerevisiae* is a unicellular eukaryotic organism that offers several benefits as an expression system, including ease of handling, amenability to genetic modification, and rapid growth in inexpensive media (Baghban et al., 2019; Volkov, 2015). However, the yeast expression system is generally less efficient at folding complex mammalian proteins, which can lead to misfolding, aggregation, or degradation of the protein. In addition, the limited capability of yeast cells to perform post-translational modifications may affect the recombinant protein's activity and stability (Vieira Gomes et al., 2018).

Mammalian expression systems, such as Chinese hamster ovary (CHO) and human embryonic kidney 293 (HEK293) cells, can provide a more natural environment for expressing and studying PfFNT, since they are derived from the same species as the protein of interest. Furthermore, mammalian cells are capable of performing more complex post-translational modifications, which can be important for certain proteins to function properly (Geisse et al., 1996). In comparison to yeast cells, mammalian cells also

possess a more sophisticated folding machinery, which allows them to correctly fold complex proteins (Abaandou et al., 2021; Ooi et al., 2016; Thomas & Smart, 2005).

In this study, a fully functional pentameric PfFNT was validated in mammalian cells. The successful expression of PfFNT in HEK293 cells resulted in the integration of the proteins into the plasma membrane, which is consistent with previous research (Marchetti et al., 2015; Wu et al., 2015). Notably, the study also demonstrated that PfFNT, when expressed in human embryonic kidney cells, can effectively transport lactate, as evidenced by measurements of lactate accumulation and acidification using a pH-sensitive fluorogenic probe. The investigation showed that inhibiting the two main lactate transporters, MCT1 and MCT4, with the anti-hypertensive drug Syrosingopine, decreased intracellular pH in HEK293 cells, as observed by the enhanced intensity of the fluorescent dye compared to the DMSO negative control. However, the expression of PfFNT rescued the acidification, suggesting that the additional lactate generated by increased glycolysis was mostly exported out of the cell *via* PfFNT. Treatment with the PfFNT-specific inhibitor, BH296, blocked lactate efflux and caused an increase in intracellular pH, validating the assay. Finally, blocking all three transporters, MCT1, MCT4, and PfFNT, resulted in the acidification of HEK293 cells expressing PfFNT. These findings provide further support for the crucial role of PfFNT in the lactate transport and regulation of intracellular pH.

4.2 Investigating PfFNT-ligand interactions: techniques and challenges

The early phase of drug discovery involves exploring hits and leads for a target of interest and can be long, inefficient, and expensive. To reduce costs, reliable techniques are needed to investigate target-ligand interactions. These techniques can be divided into two categories: functional assays and ligand binding assays (Hulme & Trevethick, 2010; Nierode et al., 2016; Pollard, 2010). Functional assays show the effect of a ligand at a target binding site, but are subject to limitations and can be difficult to set up (Albert-Vega et al., 2018). Ligand binding assays directly record target-ligand binding and provide information about the affinity of a test compound for a target, but only reveal affinity and have lower throughput (Cai & Krusemark, 2022). To date, many methods using various detection techniques have been established.

4.2.1 Yeast-based uptake assay with ^{14}C radiolabelled substrates

The Beitz lab employed a yeast-based uptake assay with ^{14}C radiolabelled substrates to determine the IC_{50} values of the investigated compounds (Golldack et al., 2017; Walloch

et al., 2020; Wu et al., 2015). This method generally yielded reproducible results with small error ranges. The significant benefit of this system is the possibility to directly observe the effect of an inhibitor on the substrate conductivity of a transporter, allowing for precise conclusions to be drawn about structure-activity relationships (Golldack et al., 2017). However, the yeast lactate transport assay required inhibitor molecules to pass through the cell wall and cellular membrane to access and block the cytoplasmic target binding site, which led to slower apparent association kinetics (Jakobowska et al., 2021). As a result, the currently used yeast assay system was unsuitable for establishing the affinity and kinetic binding parameters of the inhibitor compounds to PfFNT (Jakobowska et al., 2021). In this work, these limitations were overcome, and fluorescence cross-correlation spectroscopy was used as a drug discovery tool to directly investigate the affinity and binding kinetics of small-molecule inhibitors to both wild type and mutant PfFNT.

4.2.2 FCCS-based assay

A thorough understanding of the molecular interactions between an inhibitor and its designated target is crucial at all phases of the drug research and development process (Antoine et al., 2016; Jakobowska et al., 2021). As mentioned before, functional cellular assays, such as the previously used yeast-based monitoring of PfFNT lactate transport (Golldack et al., 2017; Walloch et al., 2020; Wu et al., 2015), provide only limited information on a compound's binding strength to the target, as other factors such as solubility and membrane permeability also affect its activity (Jakobowska et al., 2021). FCCS, on the other hand, allows for an unbiased examination of the affinity and binding kinetics of the inhibitor to its target (Jakobowska et al., 2021). As such, biophysical measurements are important to guide compound optimization based on structure-activity relationships. The affinity of a drug to its target can only be accurately assessed with knowledge of the active target concentration, yet this information is usually absent in cell-based functional assays (Jakobowska et al., 2021). With FCCS, comprehensive information is obtained on the concentrations of the target and tracer, homogeneity of particle size or the existence of aggregates, diffusion time, and binding state, allowing for accurate characterization of the molecular interaction (Dittrich et al., 2001; Jakobowska et al., 2021; Lippincott-Schwartz et al., 2001; Medina & Schwille, 2002; Schwille, 2001). Additionally, precise determinations of rate constants can help in selecting compounds with a long residence time, which can improve the efficacy of lactate export inhibition.

Inhibitors with similar affinities but differing association and dissociation rates can exhibit distinct biological activity profiles (Antoine et al., 2016; Copeland et al., 2006; Guo et al., 2014; Jakobowska et al., 2021; Lu & Tonge, 2010; Núñez et al., 2012). The duration in which a drug molecule remains attached to its target, known as the drug-target residence time, has a significant impact on the drug's efficacy, selectivity, and duration of inhibitory effect. As a result, it is a critical aspect of drug design and optimization that is carefully considered during the development of new drugs. Ideally, a drug candidate should have a high k_{on} value and a low k_{off} value, indicating a high binding affinity and a slow dissociation rate, resulting in a prolonged drug action (Bairy & Wong, 2011; Copeland et al., 2006; Vauquelin, 2016).

In this study, the FCCS approach proved to be valid for kinetically characterizing the interaction of the PfFNT inhibitors with their target (K_i, k_{on}, k_{off}). The obtained biophysical affinity data generally correlated well with the IC_{50} values acquired from functional assays in yeast. However, the FCCS-derived values revealed a higher affinity than the IC_{50} values would suggest, most likely due to limited transmembrane diffusion (Jakobowska et al., 2021). The findings on inhibitor affinity indicated high signal intensities for labelled BH296 and BH267.meta binding to PfFNT wild type, no binding of BH296 to PfFNT G107S, while BH267.meta-DY647 exhibited binding to PfFNT G107S. Measurements of the kinetics showed that both inhibitors are characterized by rapid association and slow dissociation rates (Jakobowska et al., 2021). The obtained K_i values, which are in the nanomolar range, indicate strong binding. In drug discovery, K_i values in the low nanomolar to picomolar range are desirable as they suggest a strong interaction between the drug and target protein, and therefore high potency. However, other factors such as selectivity, pharmacokinetics, and toxicity also impact a drug candidate's overall success (Ghimire et al., 2022; Kairys et al., 2019; Wong et al., 2012).

4.2.3 Functional assay with Syrosingopine/AZD3965 and Metformin

The use of FCCS to identify new PfFNT inhibitors has some limitations that need to be considered. One of these limitations is that the technique can only detect compounds that bind to the same pocket as the existing inhibitor. This study has shown that current inhibitors of PfFNT, BH296 and BH267.meta, bind to the intracellular side of the transporter. However, this presents a challenge in terms of penetrating the parasite's protective membranes and reaching the target site of action within the cell.

The cell membrane is a complex structure that poses significant difficulties for drug molecules. It acts as a selectively permeable barrier that surrounds the cell, and its composition and structure make it challenging for drugs to penetrate (Yang & Hinner, 2015). The ability of drugs to pass through biological cell membranes is greatly influenced by their physicochemical properties (Meanwell, 2011; Qian et al., 2017; Yang & Hinner, 2015). Key factors to consider include the acid-base nature of the molecule, which affects its charge at a given pH, its lipophilicity, which determines its distribution between lipid and aqueous environments, and its solubility (Milanetti et al., 2016). Drugs that are more lipophilic are more likely to traverse the hydrophobic phospholipid bilayer efficiently. However, molecules that are excessively hydrophobic and insoluble in aqueous body fluids may have poor absorption (Frenkel et al., 2005). Therefore, it is crucial to strike an appropriate balance between the hydrophobic and hydrophilic characteristics of a molecule (Ghuman et al., 2005; Milanetti et al., 2016; Seelig, 2007; Waring, 2009). Moreover, the capacity of a drug molecule to cross the cell membrane is largely impacted by its size and shape. Smaller and less complex molecules have a higher propensity to penetrate the cell membrane (Alagga & Gupta, 2022; Matsson & Kihlberg, 2017; Yang & Hinner, 2015). In conclusion, designing drugs that can effectively bind to intracellular targets is a challenging task that requires careful optimization of drug structures and properties.

Compared to drugs that must traverse the cell membrane to reach their target, drugs that bind to the exterior of cells are typically more accessible (Yang & Hinner, 2015). These drugs can interact molecular targets on the surface of cells, allowing them to elicit their pharmacological effects. Since these drugs can interact with their targets more quickly, they may have a more rapid onset of action. Additionally, binding extracellularly may result in fewer unwanted side effects and off-target effects since these drugs are more specific to their target molecule (Frutiger et al., 2021). Moreover, these drugs can be more easily absorbed, distributed, and eliminated from the body, resulting in improved bioavailability and therapeutic efficacy (Alagga & Gupta, 2022; Doogue & Polasek, 2013).

To sum up, drugs that interact with cell surface targets offer several advantages over those that penetrate the cell membrane. As mentioned earlier, the FCCS method allows the identification of new PfFNT inhibitors, but only those that also bind to the inner side of the PfFNT transporter. Thus, finding inhibitors that can bind to the extracellular side

of the channel requires alternative approaches. One such approach is the development of a functional screen for PfFNT, which goes beyond traditional affinity-based screening and offers a new way to identify effective inhibitors.

In the present research, a new functional screening assay for PfFNT inhibitors was established. The theory behind the study was based on the observation that treatment of HEK293 cells expressing PfFNT with inhibitors of monocarboxylate transporters (Syrosingopine/AZD3965), an oxidative phosphorylation inhibitor (Metformin), and a specific PfFNT inhibitor (BH296) led to cell death by blocking the glycolytic pathway. Syrosingopine efficiently inhibits the two most important lactate transporters, MCT1 and MCT4. LDH inhibition due to increased intracellular lactate levels caused by Syrosingopine's blockage of lactate efflux decreases the NAD^+/NADH ratio, leading to the loss of glycolytic ATP production. Metformin inhibits the second of two cellular pathways for NAD^+ regeneration (mitochondrial respiration). Therefore, when used in conjunction with Syrosingopine, the cell's ability to recycle NAD^+ is completely lost (Benjamin et al., 2018). The depletion of NAD^+ leads to cell death since the cancer cells are no longer able to produce sufficient energy (Benjamin et al., 2018; Saraei et al., 2019). However, in the absence of BH296, cell death did not occur. This gave rise to the idea of screening a drug library to identify compounds that, like BH296, block the transport of lactate out of the cell and cause cell death.

4.3 Screening of compound libraries using newly established methods

As a result of this work, two different tools have been established that enable the search for novel inhibitors of PfFNT: an FCCS-based assay and a functional assay. Moreover, as part of this thesis, the first compound libraries were tested using new screening methods.

The short assay development time and the applicability of FCCS as a high-throughput tool facilitate the screening of a large number of compounds for their ability to interact with PfFNT wild type and therapeutically relevant mutants (Jakobowska et al., 2021). In this study, the AnalytiCon NATx library, consisting of 2000 diverse macrocycles, was screened using FCCS to identify novel scaffolds with the potential to inhibit PfFNT. A diverse library was chosen because it increases the chances of discovering rare and unique compounds with desired properties, such as high activity or specificity, among a large number of candidates and reduces the risk of false-positives and biases introduced by using a limited set of molecules. The screening process involved an acquisition time of 8 x 3 seconds,

which was selected to efficiently process a large number of samples while still maintaining accuracy and cost-effectiveness. If active compounds are identified, the next step would be to conduct structure-activity relationship (SAR) studies to understand their structural features and guide the design of more potent and selective compounds. However, the screening for inhibitors of PfFNT did not result in the identification of any promising compounds that effectively inhibit PfFNT. The lack of hits may be due to the challenging structure of PfFNT, rather than any limitations in the screening method, as the test plate showed no issues during the screening process. The *P. falciparum* formate-nitrite transporter exhibits a long, narrow transport path for the substrate, and it appears that only inhibitors with small substituents are capable of blocking PfFNT, whereas larger molecules are not effective. The AnalytiCon NATx library covers a broad range of physical chemistry and structural space, including structures that vary from peptides to macrolide-like molecules. Nevertheless, the limited diversity in the compound library utilized in this study may have restricted the identification of potential hits. It would have been advantageous to screen a more extensive collection of inhibitors with slimmer and more linear structures, but it was not feasible during the course of this thesis due to time and resource constraints.

It is also important to keep in mind that sometimes screening can lead to inaccurate results. In FCCS, false-positives may arise from the non-specific binding of fluorescent molecules, resulting in an apparent correlation between the fluorescence signals of the two labelled molecules. Additionally, false-positives can result from background fluorescence caused by impurities or sample autofluorescence (Kohl & Schwille, 2005; Schwille et al., 1999). False-negative results in FCCS can occur when the concentration of the labelled molecules is too low, which can cause a low signal-to-noise ratio and prevent the detection of actual interactions between molecules (Mittag et al., 2018; Yu et al., 2021). Other factors that could lead to false-negatives include photobleaching, non-homogeneous samples, and instrumental artefacts, such as fluctuations in laser power or detector noise (Eckert et al., 2020; Yu et al., 2021).

Next, a drug library of 22,000 compounds (20,000 ChemDiv library + 2000 AnalytiCon NATx library tested earlier with FCCS) was screened for their ability to induce cell death. The screening process was designed to exclude false-positive results due to the toxicity of the compounds. To achieve this, parallel plates were set up containing HEK293 cells

not expressing PfFNT, and these cells were treated only with the oxidative phosphorylation inhibitor Metformin. This allowed the identification of compounds that induce cell death specifically in HEK293 cells expressing PfFNT. The screening resulted in 357 positive hits (hit rate 1.6%), of which 20 were reconfirmed after a secondary screening, where the hits were reassembled on a single plate and tested at the same concentration (30 µM). The 20 positive hits were then tested for lactate accumulation using a fluorogenic probe, and only 7 of them induced a significant reduction in intracellular pH, seen as an increase in fluorescent dye intensity. All of the positive hits came from the ChemDiv library, while no hits were extracted from the AnalytiCon NATx library, which is in line with the FCCS screening outcomes. It is important to note that the false-positive results in the initial screening were likely due to technical issues related to the mixing of the test compounds with the cell culture medium. This was evident from observing several wells under the microscope, which showed that cells sometimes do not grow in the center of the well but only on the sides. This phenomenon is believed to be caused by the DMSO used to dissolve the test compounds, which did not mix properly with the medium after being added by the pipetting robot. The DMSO droplet, being heavier than the DMEM, is suspected to have settled to the bottom of the well, preventing cell growth and thus generating false-positive results. In conclusion, the present study successfully developed an assay for discovering new compounds that block the PfFNT transporter. The assay resulted in the identification of 20 potential hits, 7 of which induced a significant reduction in intracellular pH. However, it is necessary to further investigate the discovered inhibitors and to test the compounds at lower concentrations, e.g., 10 µM. The chemical structures of the hits are different from BH296 or BH267.meta and the discovered compounds would probably not fit in the current PfFNT inhibitor binding model. It should also be investigated why only 7 compounds out of 20 caused a drop in pH and the test method should be optimized to avoid false-positive results in the future. Initial attempts were made to cross-validate the hits, but additional measurements are required. Nonetheless, this task was beyond the scope of this thesis.

In the established functional assay, as mentioned earlier, the main reason for the occurrence of false results may have been incorrect handling of the experiments, specifically incomplete mixing of DMSO with the cell culture media. This procedure should be improved for further experiments, perhaps by using a plate shaker for a few minutes after adding compounds. Incorrect results could also be due to inappropriate

treatment of the cells and cell death caused by reasons other than the action of the inhibitor. Additionally, some compounds can block the tetracycline promoter by interfering with the binding of tetracycline to the tetracycline repressor protein (Chopra & Roberts, 2001; Das et al., 2016). In such cases, PfFNT was not expressed, which could also lead to false-positive results.

This study has demonstrated the challenges of developing inhibitors for PfFNT and emphasized the importance of monitoring for false results. Both false-positive and false-negative results can occur during measurements, which can significantly impact the accuracy and reliability of the data obtained. That is why it is always essential to validate any experimental results through appropriate controls and complementary methods. Now that all the necessary tools are established, it is only a matter of creating more screens with compound libraries covering different chemistry spaces to identify the ideal PfFNT inhibitor.

4.4 Outlook

Malaria continues to be a major public health concern worldwide, and ongoing research is necessary to discover new drugs, vaccines, and control techniques to reduce the disease burden. Since all available antimalarial drugs are increasingly threatened by resistance in the parasites, the development of compounds addressing novel targets is essential. Furthermore, the current drugs can have side effects, and long-term use may adversely affect patients' health, underscoring the need for safer, more effective, and affordable alternatives. The urgent need for new antimalarial drugs is further reinforced by the spread of malaria to new regions worldwide, including places previously considered malaria-free, such as Europe. While malaria is commonly associated with tropical regions, countries surrounding the Mediterranean Sea, including Italy, Greece, and Spain, have reported cases of the disease. This trend is expected to continue, largely due to climate change, which has enabled malaria-carrying mosquitoes to expand their range as temperatures rise (Caminade et al., 2014; Carlson et al., 2023; Fischer et al., 2020). The increasing mobility of people across the world has also facilitated the transmission of malaria to previously unaffected areas (Wesolowski et al., 2012).

Lactate transport inhibitors are a valid novel class of antimalarials with a unique mechanism of action (Nerlich et al., 2021). Overall, targeting PfFNT represents a promising approach to combat malaria, with several potential advantages over currently

available antimalarial drugs, including a novel target, improved specificity, and a lower likelihood of developing drug resistance. However, further research is needed to fully understand the mechanism of action of PfFNT inhibitors and to develop safe and effective drugs based on this target. The new screening methods established in this dissertation can greatly assist in this task.

5 Literature

Abaandou, L., Quan, D., & Shiloach, J. (2021). Affecting HEK293 cell growth and production performance by modifying the expression of specific genes. *Cells*, *10*, 1667.

Achan, J., Talisuna, A. O., Erhart, A., Yeka, A., Tibenderana, J. K., Baliraine, F. N., Rosenthal, P. J., & D'Alessandro, U. (2011). Quinine, an old anti-malarial drug in a modern world: role in the treatment of malaria. *Malar. J.*, *10*, 144.

Adjalley, S. H., Johnston, G. L., Li, T., Eastman, R. T., Ekland, E. H., Eappen, A. G., Richman, A., Sim, B. K. L., Lee, M. C. S., Hoffman, S. L., & Fidock, D. A. (2011). Quantitative assessment of *Plasmodium falciparum* sexual development reveals potent transmission-blocking activity by methylene blue. *PNAS*, *108*, 1214-1223.

Agilent Technologies. (2004). Tips and tricks of HPLC system troubleshooting. Retrieved March 10, 2022, from https://www.agilent.com/cs/library/training/public/Presentation_Topic%202_%20TIPS%20and%20Tricks%20HPLC%20Troublesh-ooting.pdf.

Alagga, A. A., & Gupta, V. (2022). Drug absorption. *StatPearls*. Retrieved August 23, 2022, from https://www.ncbi.nlm.nih.gov/books/NBK557405/.

Albert-Vega, C., Tawfik, D. M., Trouillet-Assant, S., Vachot, L., Mallet, F., & Textoris, J. (2018). Immune functional assays, from custom to standardized tests for precision medicine. *Front. Immunol.*, *9*, 2367.

Ali, M. Z. (2012). Malaria. Retrieved May 13, 2022, from https://www.researchgate.net/publication/279200967_Malaria.

Alonso, P. L., & O'Brien, K. L. (2022). A malaria vaccine for Africa - an important step in a century-long quest. *N. Engl. J. Med.*, *386*, 1005-1007.

Ansbro, M. R. (2020). An investigation of the mechanisms of piperaquine resistance in *Plasmodium falciparum* malaria. *Dissertation*. University of Cambridge. Online available at: https://doi.org/10.17863/CAM.50480.

Antoine, T., Ott, D., Ebell, K., Hansen, K., Henry, L., Becker, F., & Hannus, S. (2016). Homogeneous time-resolved G protein-coupled receptor-ligand binding assay based on fluorescence cross-correlation spectroscopy. *Anal. Biochem.*, *502*, 24-35.

Antony, H., & Parija, S. (2016). Antimalarial drug resistance: an overview. *Trop. Parasitol.*, *6*, 30-41.

Ariey, F., Witkowski, B., Amaratunga, C., Beghain, J., Langlois, A. C., Khim, N., Kim, S., Duru, V., Bouchier, C., Ma, L., Lim, P., Leang, R., Duong, S., Sreng, S., Suon, S., Chuor, C. M., Bout, D. M., Ménard, S., Rogers, W. O., . . . Ménard, D. (2014). A molecular marker of artemisinin-resistant *Plasmodium falciparum* malaria. *Nature*, *505*, 50-55.

Arrow, K. J., Panosian, C., & Gelband, H. (2004). Saving lives, buying time: economics of malaria drugs in an age of resistance. *NAP*, *1*, 384.

Ashley, E. A., & White, N. J. (2014). The duration of *Plasmodium falciparum* infections. *Malar. J.*, *13*, 500.

Literature

Atkovska, K., & Hub, J. S. (2017). Energetics and mechanism of anion permeation across formate-nitrite transporters. *Sci. Rep.*, *7*, 12027.

Bacia, K., Kim, S. A., & Schwille, P. (2006). Fluorescence cross-correlation spectroscopy in living cells. *Nat. Methods*, *3*, 83-89.

Bacia, K., Petrášek, Z., & Schwille, P. (2012). Correcting for spectral cross-talk in dual-color fluorescence cross-correlation spectroscopy. *ChemPhysChem*, *13*, 1221-1231.

Bacia, K., & Schwille, P. (2007). Practical guidelines for dual-color fluorescence cross-correlation spectroscopy. *Nat. Protoc.*, *2*, 2842-2856.

Bader, A., & Beitz, E. (2020). Transmembrane facilitation of lactate/H^+ instead of lactic acid is not a question of semantics but of cell viability. *Membranes*, *10*, 236.

Baghban, R., Farajnia, S., Rajabibazl, M., Ghasemi, Y., Mafi, A., Hoseinpoor, R., Rahbarnia, L., & Aria, M. (2019). Yeast expression systems: overview and recent advances. *Mol. Biotechnol.*, *61*, 365-384.

Bairy, S., & Wong, C. F. (2011). Influence of kinetics of drug binding on EGFR signaling: a comparative study of three EGFR signaling pathway models. *Proteins: Struct. Funct. Genet.*, *79*, 2491-2504.

Bartoloni, A., & Zammarchi, L. (2012). Clinical aspects of uncomplicated and severe malaria. *Mediterr. J. Hematol. Infect. Dis.*, *4*, 2012-2026.

Beard, J. (2006). DDT and human health. *Sci. Total. Environ.*, *355*, 78-89.

Benjamin, D., Colombi, M., Hindupur, S. K., Betz, C., Lane, H. A., El-Shemerly, M. Y., Lu, M., Quagliata, L., Terracciano, L., Moes, S., Sharpe, T., Wodnar-Filipowicz, A., Moroni, C., & Hall, M. N. (2016). Syrosingopine sensitizes cancer cells to killing by metformin. *Sci. Adv.*, *2*, 160.

Benjamin, D., Robay, D., Hindupur, S. K., Pohlmann, J., Colombi, M., El-Shemerly, M. Y., Maira, S.-M., Moroni, C., Lane, H. A., & Hall, M. N. (2018). Dual inhibition of the lactate transporters MCT1 and MCT4 is synthetic lethal with metformin due to NAD^+ depletion in cancer cells. *Cell Rep.*, *25*, 3047-3058.

Berry-Cabán, C. S. (2011). DDT and silent spring: fifty years after. *JMVH*, *19*, 4.

Binka, F., & Akweongo, P. (2006). Prevention of malaria using ITNs: potential for achieving the millennium development goals. *Curr. Mol. Med.*, *6*, 261-267.

Birnbaum, J. (2017). A novel genetic system for the functional analysis of essential proteins of the human malaria parasite *Plasmodium falciparum*. *Dissertation*. University of Hamburg. Online available at: https://ediss.sub.uni-hamburg.de/handle/ediss/7500.

Blancke-Soares, A. (2016). Identification of trafficking determinants in novel PNEPs of the human malaria parasite *Plasmodium falciparum*. *Dissertation*. University of Hamburg. Online available at: https://ediss.sub.uni-hamburg.de/handle/ediss/6780.

Blasco, B., Leroy, D., & Fidock, D. A. (2017). Antimalarial drug resistance: linking *Plasmodium falciparum* parasite biology to the clinic. *Nat. Med.*, *23*, 917-928.

Bloland, P. B., & Williams, H. A. (2002). Malaria control during mass population movements and natural disasters. *NAP*, *1*, 181.

Bray, R. S., & Garnham, P. C. (1982). The life-cycle of primate malaria parasites. *Br. Med. Bull.*, *38*, 117-122.

Brazier, A. J., Avril, M., Bernabeu, M., Benjamin, M., & Smith, J. D. (2017). Pathogenicity determinants of the human malaria parasite *Plasmodium falciparum* have ancient origins. *mSphere*, *2*, 348.

Bruce-Chwatt, L. J. (1985). Essential malariology. *CRC Press*, *4*, 352.

Bruce, A. (1989). Molecular biology of the cell. *ASCB*, *34*, 1342.

BSPH. (n.d.). Life cycle of the malaria parasite. *Photograph*. Retrieved June 11, 2022, from http://ocw.jhsph.edu.

Buffet, P. A., Safeukui, I., Deplaine, G., Brousse, V., Prendki, V., Thellier, M., Turner, G. D., & Mercereau-Puijalon, O. (2011). The pathogenesis of *Plasmodium falciparum* malaria in humans: insights from splenic physiology. *Blood*, *117*, 381-392.

Butler, A. R., Khan, S., & Ferguson, E. (2010). A brief history of malaria chemotherapy. *J. R. Coll. Physicians Edinb.*, *40*, 172-177.

Cai, B., & Krusemark, C. J. (2022). Multiplexed small-molecule-ligand binding assays by affinity labeling and DNA sequence analysis. *Angew. Chem. Int. Ed. Engl.*, *61*, 202.

Caminade, C., Kovats, S., Rocklov, J., Tompkins, A. M., Morse, A. P., Colón-González, F. J., Stenlund, H., Martens, P., & Lloyd, S. J. (2014). Impact of climate change on global malaria distribution. *PNAS*, *111*, 3286-3291.

Capanna, E. (2006). Grassi versus Ross: who solved the riddle of malaria? *Int. Microbiol.*, *9*, 69-74.

Carlson, C. J., Bannon, E., Mendenhall, E., Newfield, T., & Bansal, S. (2023). Rapid range shifts in African *Anopheles* mosquitoes over the last century. *Biol. Lett.*, *19*, 202.

CDC. (2015). Malaria - about malaria disease. Retrieved August 28, 2022, from https://www.cdc.gov/malaria/about/disease.html.

Chae, Y. K., Arya, A., Malecek, M.-K., Shin, D. S., Carneiro, B., Chandra, S., Kaplan, J., Kalyan, A., Altman, J. K., Platanias, L., & Giles, F. (2016). Repurposing metformin for cancer treatment: current clinical studies. *Oncotarget*, *7*, 40767–40780.

Chen, H., Farkas, E. R., & Webb, W. W. (2008). *In vivo* applications of fluorescence correlation spectroscopy. *Methods Cell. Biol.*, *89*, 3-35.

Cheng, Y., & Prusoff, W. H. (1973). Relationship between the inhibition constant (K_1) and the concentration of inhibitor which causes 50 per cent inhibition (I_{50}) of an enzymatic reaction. *Biochem. Pharmacol.*, *22*, 3099-3108.

Chong, Z. X., Yeap, S. K., & Ho, W. Y. (2021). Transfection types, methods and strategies: a technical review. *PeerJ*, *9*, 1165.

Chopra, I., & Roberts, M. (2001). Tetracycline antibiotics: mode of action, applications, molecular biology, and epidemiology of bacterial resistance. *Microbiol. Mol. Biol. Rev.*, *65*, 232-260.

Coatney, G. R. (1963). Pitfalls in a discovery: the chronicle of chloroquine. *Am. J. Trop. Med.*, *12*, 121-128.

Coluzzi, M. (1999). The clay feet of the malaria giant and its African roots: hypotheses and inferences about origin, spread and control of *Plasmodium falciparum*. *Parassitologia*, *41*, 277-283.

Copeland, R. A., Pompliano, D. L., & Meek, T. D. (2006). Drug-target residence time and its implications for lead optimization. *Nat. Rev. Drug. Discov.*, *5*, 730-739.

Costa, F. T., Avril, M., Nogueira, P. A., & Gysin, J. (2006). Cytoadhesion of *Plasmodium falciparum*-infected erythrocytes and the infected placenta: a two-way pathway. *Braz. J. Med. Biol. Res.*, *39*, 1525-1536.

Cowman, A. F., & Crabb, B. S. (2006). Invasion of red blood cells by malaria parasites. *Cell*, *124*, 755-766.

Cox, F. (2010). History of the discovery of the malaria parasites and their vectors. *Parasit. Vectors*, *3*, 5.

Cranmer, S. L., Conant, A. R., Gutteridge, W. E., & Halestrap, A. P. (1995). Characterization of the enhanced transport of L- and D-lactate into human red blood cells infected with *Plasmodium falciparum* suggests the presence of a novel saturable lactate proton cotransporter. *J. Biol. Chem.*, *270*, 45-52.

Crompton, P. D., Pierce, S. K., & Miller, L. H. (2010). Advances and challenges in malaria vaccine development. *J. Clin. Invest.*, *120*, 4168-4178.

Cui, L., & Su, X. Z. (2009). Discovery, mechanisms of action and combination therapy of artemisinin. *Expert. Rev. Anti. Infect. Ther.*, *7*, 999-1013.

Czyzewski, B. K., & Wang, D. N. (2012). Identification and characterization of a bacterial hydrosulphide ion channel. *Nature*, *483*, 494-497.

Dankwa, S., Lim, C., Bei, A. K., Jiang, R. H. Y., Abshire, J. R., Patel, S. D., Goldberg, J. M., Moreno, Y., Kono, M., Niles, J. C., & Duraisingh, M. T. (2016). Ancient human sialic acid variant restricts an emerging zoonotic malaria parasite. *Nat. Commun.*, *7*, 11187.

Das, A. T., Tenenbaum, L., & Berkhout, B. (2016). Tet-on systems for doxycycline-inducible gene expression. *Curr. Gene. Ther.*, *16*, 156-167.

de Vries, P. J., & Dien, T. K. (1996). Clinical pharmacology and therapeutic potential of artemisinin and its derivatives in the treatment of malaria. *Drugs*, *52*, 818-836.

Delves, M., Plouffe, D., Scheurer, C., Meister, S., Wittlin, S., Winzeler, E. A., Sinden, R. E., & Leroy, D. (2012). The activities of current antimalarial drugs on the life cycle stages of *Plasmodium*: a comparative study with human and rodent parasites. *PLoS Med.*, *9*, 1001.

Desai, S. A., Krogstad, D. J., & McCleskey, E. W. (1993). A nutrient-permeable channel on the intraerythrocytic malaria parasite. *Nature*, *362*, 643-646.

Dhangadamajhi, G., Kar, S. K., & Ranjit, M. (2010). The survival strategies of malaria parasite in the red blood cell and host cell polymorphisms. *Malar. Res. Treat.*, *2010*, 973.

Dittrich, P., Malvezzi-Campeggi, F., Jahnz, M., & Schwille, P. (2001). Accessing molecular dynamics in cells by fluorescence correlation spectroscopy. *Biol. Chem.*, *382*, 491-494.

Doogue, M. P., & Polasek, T. M. (2013). The ABCD of clinical pharmacokinetics. *Ther. Adv. Drug. Saf.*, *4*, 5-7.

Dubey, A., Lakshminarayana, L., Sadananda, D., Gouthami, K., Elfansu, Singh, A., Singh, A., & Singh, A. (2021). Inferences of carbon dioxide in present-day cell culture systems: an unacknowledged problem and perspectives. *Austin J. Pharmacol. Ther.*, *1*, 1033.

Duraisingh, M. T., & Cowman, A. F. (2005). Contribution of the pfmdr1 gene to antimalarial drug-resistance. *Acta. Trop.*, *94*, 181-190.

Durand, R., Jafari, S., Vauzelle, J., Delabre, J. F., Jesic, Z., & Le Bras, J. (2001). Analysis of pfcrt point mutations and chloroquine susceptibility in isolates of *Plasmodium falciparum*. *Mol. Biochem. Parasitol.*, *114*, 95-102.

Eastman, R. T., & Fidock, D. A. (2009). Artemisinin-based combination therapies: a vital tool in efforts to eliminate malaria. *Nat. Rev. Microbiol.*, *7*, 864-874.

Eckert, A. F., Gao, P., Wesslowski, J., Wang, X., Rath, J., Nienhaus, K., Davidson, G., & Nienhaus, G. U. (2020). Measuring ligand-cell surface receptor affinities with axial line-scanning fluorescence correlation spectroscopy. *eLife*, *9*, 5286.

Eckhoff, P. A., Wenger, E. A., Godfray, H. C. J., & Burt, A. (2017). Impact of mosquito gene drive on malaria elimination in a computational model with explicit spatial and temporal dynamics. *PNAS*, *114*, 255-264.

Eckstein-Ludwig, U., Webb, R. J., van Goethem, I. D. A., East, J. M., Lee, A. G., Kimura, M., O'Neill, P. M., Bray, P. G., Ward, S. A., & Krishna, S. (2003). Artemisinins target the SERCA of *Plasmodium falciparum*. *Nature*, *424*, 957-961.

Eigen, M., & Rigler, R. (1994). Sorting single molecules: application to diagnostics and evolutionary biotechnology. *PNAS*, *91*, 5740-5747.

Elliott, J. L., Saliba, K. J., & Kirk, K. (2001). Transport of lactate and pyruvate in the intraerythrocytic malaria parasite, *Plasmodium falciparum*. *Biochem. J.*, *355*, 733-739.

Elson, E. L., & Magde, D. (1974). Fluorescence correlation spectroscopy. I. Conceptual basis and theory. *Biopolymers*, *13*, 1-27.

Enayati, A., & Hemingway, J. (2010). Malaria management: past, present, and future. *Annu. Rev. Entomol.*, *55*, 569-591.

Fairhurst, R. M., & Wellems, T. E. (2010). Principles and practice of infectious diseases. *Churchill Livingstone*, *7*, 3437–3462.

Fidock, D. A., Nomura, T., Talley, A. K., Cooper, R. A., Dzekunov, S. M., Ferdig, M. T., Ursos, L. M., Sidhu, A. B., Naudé, B., Deitsch, K. W., Su, X. Z., Wootton, J. C., Roepe, P. D., & Wellems, T. E. (2000). Mutations in the *P. falciparum* digestive vacuole transmembrane protein PfCRT and evidence for their role in chloroquine resistance. *Mol. Cell.*, *6*, 861-871.

Literature

Fischer, L., Gültekin, N., Kaelin, M. B., Fehr, J., & Schlagenhauf, P. (2020). Rising temperature and its impact on receptivity to malaria transmission in Europe: a systematic review. *Travel Med. Infect. Dis.*, *36*, 101815.

Földes-Papp, Z. (2005). How the molecule number is correctly quantified in two-color fluorescence cross-correlation spectroscopy: corrections for cross-talk and quenching in experiments. *Curr. Pharm. Biotechnol.*, *6*, 437-444.

Foley, M., & Tilley, L. (1998). Quinoline antimalarials: mechanisms of action and resistance and prospects for new agents. *Pharmacol. Ther.*, *79*, 55-87.

Frenkel, Y. V., Clark, A. D., Jr., Das, K., Wang, Y. H., Lewi, P. J., Janssen, P. A., & Arnold, E. (2005). Concentration and pH dependent aggregation of hydrophobic drug molecules and relevance to oral bioavailability. *J. Med. Chem.*, *48*, 1974-1983.

Frey, S. G., Chelo, D., Kinkela, M. N., Djoukoue, F., Tietche, F., Hatz, C., & Weber, P. (2010). Artesunate-mefloquine combination therapy in acute *Plasmodium falciparum* malaria in young children: a field study regarding neurological and neuropsychiatric safety. *Malar. J.*, *9*, 291.

Frutiger, A., Tanno, A., Hwu, S., Tiefenauer, R. F., Vörös, J., & Nakatsuka, N. (2021). Nonspecific binding - fundamental concepts and consequences for biosensing applications. *Chem. Rev.*, *121*, 8095-8160.

Fry, M., & Pudney, M. (1992). Site of action of the antimalarial hydroxynaphthoquinone, 2-[trans-4-(4'-chlorophenyl) cyclohexyl]-3- hydroxy-1,4-naphthoquinone. *Biochem. Pharmacol.*, *43*, 1545-1553.

Fujioka, H., & Aikawa, M. (2002). Structure and life cycle. *Chem. Immunol.*, *80*, 1-26.

Fus-Kujawa, A., Prus, P., Bajdak-Rusinek, K., Teper, P., Gawron, K., Kowalczuk, A., & Sieron, A. L. (2021). An overview of methods and tools for transfection of eukaryotic cells *in vitro*. *Front. Bioeng. Biotechnol.*, *9*, 2021.

Gantz, V. M., Jasinskiene, N., Tatarenkova, O., Fazekas, A., Macias, V. M., Bier, E., & James, A. A. (2015). Highly efficient Cas9-mediated gene drive for population modification of the malaria vector mosquito *Anopheles stephensi*. *PNAS*, *112*, 6736-6743.

Geisse, S., Gram, H., Kleuser, B., & Kocher, H. P. (1996). Eukaryotic expression systems: a comparison. *Protein Expr. Purif.*, *8*, 271-282.

Ghimire, A., Tayara, H., Xuan, Z., & Chong, K. T. (2022). CSatDTA: prediction of drug-target binding affinity using convolution model with self-attention. *Int. J. Mol. Sci.*, *23*, 15.

Ghuman, J., Zunszain, P. A., Petitpas, I., Bhattacharya, A. A., Otagiri, M., & Curry, S. (2005). Structural basis of the drug-binding specificity of human serum albumin. *J. Mol. Biol.*, *353*, 38-52.

Glauner, H., Ruttekolk, I. R., Hansen, K., Steemers, B., Chung, Y.-D., Becker, F., Hannus, S., & Brock, R. (2010). Simultaneous detection of intracellular target and off-target binding of small molecule cancer drugs at nanomolar concentrations. *Br. J. Pharmacol.*, *160*, 958-970.

Golldack, A., Henke, B., Bergmann, B., Wiechert, M., Erler, H., Blancke Soares, A., Spielmann, T., & Beitz, E. (2017). Substrate-analogous inhibitors exert

antimalarial action by targeting the *Plasmodium* lactate transporter PfFNT at nanomolar scale. *PLoS Pathog.*, *13*, e1006172.

Greenwood, B. M., Fidock, D. A., Kyle, D. E., Kappe, S. H., Alonso, P. L., Collins, F. H., & Duffy, P. E. (2008). Malaria: progress, perils, and prospects for eradication. *J. Clin. Invest.*, *118*, 1266-1276.

Gregson, A., & Plowe, C. V. (2005). Mechanisms of resistance of malaria parasites to antifolates. *Pharmacol. Rev.*, *57*, 117-145.

Grisshammer, R. (2009). Purification of recombinant G-protein-coupled receptors. *Meth. Enzymol.*, *463*, 631-645.

Guan, X., & Morris, M. E. (2020). *In vitro* and *in vivo* efficacy of AZD3965 and alpha-cyano-4-hydroxycinnamic acid in the murine 4T1 breast tumor model. *AAPS J.*, *22*, 84.

Guo, D., Hillger, J. M., AP, I. J., & Heitman, L. H. (2014). Drug-target residence time - a case for G protein-coupled receptors. *Med. Res. Rev.*, *34*, 856-892.

Gupta, A., Sankaran, J., & Wohland, T. (2019). Fluorescence correlation spectroscopy: the technique and its applications in soft matter. *Phys. Sci. Rev.*, *4*, 4.

Ha, J. H., & Loh, S. N. (2012). Protein conformational switches: from nature to design. *Chemistry*, *18*, 7984-7999.

Hajek, P., Bader, A., Helmstetter, F., Henke, B., Arnold, P., & Beitz, E. (2019). Cell-free and yeast-based production of the malarial lactate transporter, PfFNT, delivers comparable yield and protein quality. *Front. pharmacol.*, *10*, 375.

Hammond, A., Galizi, R., Kyrou, K., Simoni, A., Siniscalchi, C., Katsanos, D., Gribble, M., Baker, D., Marois, E., Russell, S., Burt, A., Windbichler, N., Crisanti, A., & Nolan, T. (2016). A CRISPR-Cas9 gene drive system targeting female reproduction in the malaria mosquito vector *Anopheles gambiae. Nat. Biotechnol.*, *34*, 78-83.

Hanssen, E., Goldie, K. N., & Tilley, L. (2010). Ultrastructure of the asexual blood stages of *Plasmodium falciparum. Methods Cell Biol.* , *96*, 93-116.

Hapuarachchi, S. V., Cobbold, S. A., Shafik, S. H., Dennis, A. S. M., McConville, M. J., Martin, R. E., Kirk, K., & Lehane, A. M. (2017). The malaria parasite's lactate transporter PfFNT is the target of antiplasmodial compounds identified in whole cell phenotypic screens. *PLoS Pathog.*, *13*, e1006180.

Hashimoto, K., Yamashita, K., Enoyoshi, K., Dahan, X., Takeuchi, T., Kori, H., & Gotoh, M. (2019). The effects of coating culture dishes with collagen on fibroblast cell shape and swirling pattern formation. *J. Biol. Phys.*, *46*, 351-369.

Heinrich, T., Sala-Hojman, A., Ferretti, R., Petersson, C., Minguzzi, S., Gondela, A., Ramaswamy, S., Bartosik, A., Czauderna, F., Crowley, L., Wahra, P., Schilke, H., Böpple, P., Dudek, Ł., Leś, M., Niedziejko, P., Olech, K., Pawlik, H., Włoszczak, Ł., . . . Herhaus, C. (2021). Discovery of 5-{2-[5-chloro-2-(5-ethoxyquinoline-8-sulfo-namido)phenyl]ethynyl}-4-methoxypyridine-2-carboxylic acid, a highly selective *in vivo* useable chemical probe to dissect MCT4 biology. *J. Med. Chem.*, *64*, 11904.

Helmstetter, F., Arnold, P., Höger, B., Petersen, L. M., & Beitz, E. (2019). Formate-nitrite transporters carrying nonprotonatable amide amino acids instead of a central histidine maintain pH-dependent transport. *J. Biol. Chem.*, *294*, 623-631.

Hoare, S. R. J. (2004). Analyzing kinetic binding data. Retrieved November 15, 2022, from https://www.ncbi.nlm.nih.gov/books/NBK53196/.

Holm-Bertelsen, J., Bock, S., Helmstetter, F., & Beitz, E. (2016). High-level cell-free production of the malarial lactate transporter PfFNT as a basis for crystallization trials and directional transport studies. *Protein Expr. Purif.*, *126*, 109-114.

Homewood, C. A., Warhurst, D. C., Peters, W., & Baggaley, V. C. (1972). Lysosomes, pH and the anti-malarial action of chloroquine. *Nature*, *235*, 50-52.

Howes, R. E., Battle, K. E., Mendis, K. N., Smith, D. L., Cibulskis, R. E., Baird, J. K., & Hay, S. I. (2016). Global epidemiology of *Plasmodium vivax*. *Am. J. Trop. Med. Hyg.*, *95*, 15-34.

Hulme, E. C., & Trevethick, M. A. (2010). Ligand binding assays at equilibrium: validation and interpretation. *Br. J. Pharmacol.*, *161*, 1219-1237.

Hyde, J. E. (2007). Drug-resistant malaria - an insight. *FEBS J.*, *274*, 4688-4698.

Jakobowska, I., Becker, F., Minguzzi, S., Hansen, K., Henke, B., Epalle, N. H., Beitz, E., & Hannus, S. (2021). Fluorescence cross-correlation spectroscopy yields true affinity and binding kinetics of *Plasmodium* lactate transport inhibitors. *Pharmaceuticals*, *14*, 757.

Jamieson, A., & Toovey, S. (2008). Malaria: a traveller's guide. *J. Travel Med.*, *15*, 387.

Joët, T., Eckstein-Ludwig, U., Morin, C., & Krishna, S. (2003). Validation of the hexose transporter of *Plasmodium falciparum* as a novel drug target. *PNAS*, *100*, 7476-7479.

Jonscher, E. G. W. (2018). Identification of proteins involved in host cell cytosol uptake in the human Malaria parasite *Plasmodium falciparum*. *Dissertation*. University of Hamburg. Online available at: https://ediss.sub.uni-hamburg.de/handle/ediss/8573.

Kabasenche, W. P., & Skinner, M. K. (2014). DDT, epigenetic harm, and transgenerational environmental justice. *Environ. Health*, *13*, 62.

Kairys, V., Baranauskiene, L., Kazlauskiene, M., Matulis, D., & Kazlauskas, E. (2019). Binding affinity in drug design: experimental and computational techniques. *Expert Opin. Drug Discov.*, *14*, 755-768.

Kanaani, J., & Ginsburg, H. (1992). Effects of cinnamic acid derivatives on *in vitro* growth of *Plasmodium falciparum* and on the permeability of the membrane of malaria-infected erythrocytes. *Antimicrob. Agents Chemother.*, *36*, 1102-1108.

Kasahara, M., & Hinkle, P. C. (1977). Reconstitution and purification of the D-glucose transporter from human erythrocytes. *J. Biol. Chem.*, *252*, 7384-7390.

Kesidis, A., Depping, P., Lodé, A., Vaitsopoulou, A., Bill, R. M., Goddard, A. D., & Rothnie, A. J. (2020). Expression of eukaryotic membrane proteins in eukaryotic and prokaryotic hosts. *Methods*, *180*, 3-18.

Khammanivong, A., Saha, J., Spartz, A. K., Sorenson, B. S., Bush, A. G., Korpela, D. M., Gopalakrishnan, R., Jonnalagadda, S., Mereddy, V. R., O'Brien, T. D., Drewes, L. R., & Dickerson, E. B. (2020). A novel MCT1 and MCT4 dual inhibitor reduces

mitochondrial metabolism and inhibits tumour growth of feline oral squamous cell carcinoma. *Vet. Comp. Oncol.*, *18*, 324-341.

Khan, K. H. (2013). Gene expression in mammalian cells and its applications. *Adv. Pharm. Bull.*, *3*, 257-263.

Khosh-Naucke, M. (2018). Identification of novel parasitophorous vacuole proteins in *P. falciparum* parasites using BioID. *Dissertation*. University of Hamburg. Online available at: https://ediss.sub.uni-hamburg.de/handle/ediss/8576.

Kim, S. A., Heinze, K. G., & Schwille, P. (2007). Fluorescence correlation spectroscopy in living cells. *Nat. Methods*, *4*, 963-973.

Kim, T. K., & Eberwine, J. H. (2010). Mammalian cell transfection: the present and the future. *Anal. Bioanal. Chem.*, *397*, 3173-3178.

Kohl, T., & Schwille, P. (2005). Fluorescence correlation spectroscopy with autofluorescent proteins. *Adv. Biochem. Eng. Biotechnol.*, *95*, 107-142.

Koley, D., & Bard, A. J. (2010). Triton X-100 concentration effects on membrane permeability of a single HeLa cell by scanning electrochemical microscopy (SECM). *PNAS*, *107*, 16783-16787.

Koltermann, A., Kettling, U., Bieschke, J., Winkler, T., & Eigen, M. (1998). Rapid assay processing by integration of dual-color fluorescence cross-correlation spectroscopy: high throughput screening for enzyme activity. *PNAS*, *95*, 1421-1426.

Krettli, A. U., & Miller, L. H. (2001). Malaria: a sporozoite runs through it. *Curr. Biol.*, *11*, 409-412.

Kuhn, Y., Rohrbach, P., & Lanzer, M. (2007). Quantitative pH measurements in *Plasmodium falciparum*-infected erythrocytes using pHluorin. *Cell. Microbiol.*, *9*, 1004-1013.

Lakowicz, J. (1999). Principles of fluorescence spectroscopy. *Springer*, *1*, 1-698.

Laurens, M. B. (2020). RTS,S/AS01 vaccine (Mosquirix™): an overview. *Hum. Vaccines Immunother.*, *16*, 480-489.

Laveran, A. (1881). Un nouveau parasite trouvé dans le sang des malades atteints de fièvre palustre: origine parasitaire des accidents de l'impaludisme. *J.-B. Baillière*, *1*, 1-104.

Lee, W., Lee, Y.-I., Lee, J., Davis, L. M., Deininger, P., & Soper, S. A. (2010). Cross-talk-free dual-color fluorescence cross-correlation spectroscopy for the study of enzyme activity. *Anal. Chem.*, *82*, 1401-1410.

Lehane, M. J. (1991). The biology of blood-sucking in insects. *Springer*, *1*, 1-288.

Lewis, L. K., Robson, M. H., Vecherkina, Y., Ji, C., & Beall, G. W. (2010). Interference with spectrophotometric analysis of nucleic acids and proteins by leaching of chemicals from plastic tubes. *BioTechniques*, *48*, 297-302.

Li, X., Zhou, X., Liu, Y., Fan, J., Huo, H., Yao, J., Wang, L., & Ma, N. (2021). Overexpression of monocarboxylate transporter 4 promotes the migration and invasion of non-carcinogenic L929 fibroblast cells. *Oncol. Lett.*, *21*, 44.

Lin, S. H., & Guidotti, G. (2009). Purification of membrane proteins. *Meth. Enzymol.*, *463*, 619-629.

Lippincott-Schwartz, J., Snapp, E., & Kenworthy, A. (2001). Studying protein dynamics in living cells. *Nat. Rev. Mol. Cell Biol.*, *2*, 444-456.

Lu, H., & Tonge, P. J. (2010). Drug-target residence time: critical information for lead optimization. *Curr. Opin. Chem. Biol.*, *14*, 467-474.

Lü, W., Du, J., Schwarzer, N. J., Wacker, T., Andrade, S. L., & Einsle, O. (2013). The formate/nitrite transporter family of anion channels. *J. Biol. Chem.*, *394*, 715-727.

Lü, W., Du, J., Wacker, T., Gerbig-Smentek, E., Andrade, S. L., & Einsle, O. (2011). pH-dependent gating in a FocA formate channel. *Science*, *332*, 352-354.

Lyu, M., Su, C. C., Kazura, J. W., & Yu, E. W. (2021). Structural basis of transport and inhibition of the *Plasmodium falciparum* transporter PfFNT. *EMBO Rep.*, *22*, e51628.

Mace, K. E., Arguin, P. M., Lucchi, N. W., & Tan, K. R. (2016). Malaria surveillance - United States, 2016. *MMWR Surveill. Summ.*, *68*, 1-35.

MacRae, J. I., Dixon, M. W. A., Dearnley, M. K., Chua, H. H., Chambers, J. M., Kenny, S., Bottova, I., Tilley, L., & McConville, M. J. (2013). Mitochondrial metabolism of sexual and asexual blood stages of the malaria parasite *Plasmodium falciparum*. *BMC Biol.*, *11*, 67.

Magde, D., Elson, E., & Webb, W. W. (1972). Thermodynamic fluctuations in a reacting system - measurement by fluorescence correlation spectroscopy. *Phys. Rev. Lett.*, *29*, 705-708.

Makoah, N., & Pradel, G. (2013). Antimalarial drugs resistance in *Plasmodium falciparum* and the current strategies to overcome them. *Formatex*, *1*, 269-282.

Mala, M., Mollah, M. M. I., & Hassan, K. (2016). Interaction between parasite and vector for malaria disease transmission - a review on malaria. *Progress. agric.*, *27*, 168.

Marchetti, R. V., Lehane, A. M., Shafik, S. H., Winterberg, M., Martin, R. E., & Kirk, K. (2015). A lactate and formate transporter in the intraerythrocytic malaria parasite, *Plasmodium falciparum*. *Nat. Commun.*, *6*, 6721.

Martinez-Moro, M., Di Silvio, D., & Moya, S. E. (2019). Fluorescence correlation spectroscopy as a tool for the study of the intracellular dynamics and biological fate of protein corona. *Biophys. Chem.*, *253*, 106218.

Matsson, P., & Kihlberg, J. (2017). How big is too big for cell permeability? *J. Med. Chem.*, *60*, 1662-1664.

Mbengue, A., Bhattacharjee, S., Pandharkar, T., Liu, H., Estiu, G., Stahelin, R. V., Rizk, S. S., Njimoh, D. L., Ryan, Y., Chotivanich, K., Nguon, C., Ghorbal, M., Lopez-Rubio, J.-J., Pfrender, M., Emrich, S., Mohandas, N., Dondorp, A. M., Wiest, O., & Haldar, K. (2015). A molecular mechanism of artemisinin resistance in *Plasmodium falciparum* malaria. *Nature*, *520*, 683-687.

McKee, R. W., Ormsbee, R. A., Anfinsen, C. B., Geiman, Q. M., & Ball, E. G. (1946). Studies on malarial parasites: VI. The chemistry and metabolism of normal and parasitized (*P. knowlesi*) monkey blood. *J. Exp. Med.*, *84*, 569-582.

Meanwell, N. A. (2011). Improving drug candidates by design: a focus on physicochemical properties as a means of improving compound disposition and safety. *Chem. Res. Toxicol.*, *24*, 1420-1456.

Medeiros, S. V. (2022). Investigating metformin & syrosingopine's synthetic lethality in PC3 & THP-1 cancer cell lines. *Dissertation*. University of Plymouth. Online available at: https://pearl.plymouth.ac.uk/handle/10026.1/19460.

Medina, M. A., & Schwille, P. (2002). Fluorescence correlation spectroscopy for the detection and study of single molecules in biology. *BioEssays*, *24*, 758-764.

Mehta, M., Sonawat, H. M., & Sharma, S. (2005). Malaria parasite-infected erythrocytes inhibit glucose utilization in uninfected red cells. *FEBS Lett.*, *579*, 6151-6158.

Meister, S., Plouffe, D. M., Kuhen, K. L., Bonamy, G. M. C., Wu, T., Barnes, S. W., Bopp, S. E., Borboa, R., Bright, A. T., Che, J., Cohen, S., Dharia, N. V., Gagaring, K., Gettayacamin, M., Gordon, P., Groessl, T., Kato, N., Lee, M. C. S., McNamara, C. W., . . . Winzeler, E. A. (2011). Imaging of *Plasmodium* liver stages to drive next-generation antimalarial drug discovery. *Science*, *334*, 1372-1377.

Mendes, A. M., Schlegelmilch, T., Cohuet, A., Awono-Ambene, P., De Iorio, M., Fontenille, D., Morlais, I., Christophides, G. K., Kafatos, F. C., & Vlachou, D. (2008). Conserved mosquito/parasite interactions affect development of *Plasmodium falciparum* in Africa. *PLoS Pathog.*, *4*, e1000069.

Mesén-Ramírez, P. (2016). Characterization of the protein export steps at the parasite-host cell interface of the human malaria parasite *Plasmodium falciparum*. *Dissertation*. University of Hamburg. Online available at: https://ediss.sub.uni-hamburg.de/handle/ediss/6793.

Meshnick, S. R. (2002). Artemisinin: mechanisms of action, resistance and toxicity. *Parasitol. Int.*, *32*, 1655-1660.

Meyer, C. G., Marks, F., & May, J. (2004). Editorial: gin tonic revisited. *Trop. Med. Int. Health.*, *9*, 1239-1240.

Mikuni, S., Kodama, K., Sasaki, A., Kohira, N., Maki, H., Munetomo, M., Maenaka, K., & Kinjo, M. (2015). Screening for FtsZ dimerization inhibitors using fluorescence cross-correlation spectroscopy and surface resonance plasmon analysis. *PLOS ONE*, *10*, e0130933.

Milanetti, E., Raimondo, D., & Tramontano, A. (2016). Prediction of the permeability of neutral drugs inferred from their solvation properties. *J. Bioinform.*, *32*, 1163-1169.

Miller, K. (2022). Malaria vaccines could be game-changers. *Discover*, *43*, 63-64.

Miller, L. H., Ackerman, H. C., Su, X. Z., & Wellems, T. E. (2013). Malaria biology and disease pathogenesis: insights for new treatments. *Nat. Med.*, *19*, 156-167.

Miller, L. H., Baruch, D. I., Marsh, K., & Doumbo, O. K. (2002). The pathogenic basis of malaria. *Nature*, *415*, 673-679.

Mittag, J. J., Rädler, J. O., & McManus, J. J. (2018). Peptide self-assembly measured using fluorescence correlation spectroscopy. *Methods mol. biol.*, *1777*, 159-171.

Morgan, A., Babu, D., Reiz, B., Whittal, R., Suh, L. Y. K., & Siraki, A. G. (2019). Caution for the routine use of phenol red - it is more than just a pH indicator. *Chem. Biol. Interact.*, *310*, 108739.

Muetze, J., Ohrt, T., & Schwille, P. (2011). Fluorescence correlation spectroscopy *in vivo*. *Laser Photonics Rev.*, *5*, 52-67.

Na-Bangchang, K., & Karbwang, J. (2019). Pharmacology of antimalarial drugs, current anti-malarials. *Springer*, *1*, 1-82.

Nadeem, A. Y., Shehzad, A., Islam, S. U., Al-Suhaimi, E. A., & Lee, Y. S. (2022). Mosquirix™ RTS, S/AS01 vaccine development, immunogenicity, and efficacy. *Vaccines*, *10*, 5.

Naranjo-Prado, I. C. (2020). Quest for factors involved in the extraction of transmembrane proteins from the PPM to the PVM and the effect of jamming PTEX on PfEMP1 export in *Plasmodium falciparum*. *Dissertation*. University of Hamburg. Online available at: https://ediss.sub.uni-hamburg.de/handle/ediss/8423.

Nerlich, C., Epalle, N. H., Seick, P., & Beitz, E. (2021). Discovery and development of inhibitors of the *Plasmodial* FNT-type lactate transporter as novel antimalarials. *Pharmaceuticals*, *14*, 1191.

Nierode, G., Kwon, P. S., Dordick, J. S., & Kwon, S. J. (2016). Cell-based assay design for high-content screening of drug candidates. *Microb. Biotechnol.*, *26*, 213-225.

Núñez, S., Venhorst, J., & Kruse, C. G. (2012). Target-drug interactions: first principles and their application to drug discovery. *Drug Discov. Today*, *17*, 10-22.

Nzila, A. (2006). The past, present and future of antifolates in the treatment of *Plasmodium falciparum* infection. *J. Antimicrob. Chemother.*, *57*, 1043-1054.

O'Brien, E. P., Brooks, B. R., & Thirumalai, D. (2012). Effects of pH on proteins: predictions for ensemble and single-molecule pulling experiments. *J. Am. Chem. Soc.*, *134*, 979-987.

Oakley, M. S., Gerald, N., McCutchan, T. F., Aravind, L., & Kumar, S. (2011). Clinical and molecular aspects of malaria fever. *Trends Parasitol.*, *27*, 442-449.

Okun, I., & Veerapandian, P. (1997). New methods to mimic nature in high-throughput screening. *Nat. Biotechnol.*, *15*, 287-288.

Oliveira, G. L., Coelho, A. R., Marques, R., & Oliveira, P. J. (2021). Cancer cell metabolism: rewiring the mitochondrial hub. *Biochim. Biophys. Acta. Mol. Basis. Dis.*, *1867*, 166016.

Ooi, A., Wong, A., Esau, L., Lemtiri-Chlieh, F., & Gehring, C. (2016). A guide to transient expression of membrane proteins in HEK-293 cells for functional characterization. *Front. Physiol.*, *7*, 300.

Ortiz, D., Guiguemde, W. A., Johnson, A., Elya, C., Anderson, J., Clark, J., Connelly, M., Yang, L., Min, J., Sato, Y., Guy, R. K., & Landfear, S. M. (2015). Identification of selective inhibitors of the *Plasmodium falciparum* hexose transporter PfHT by screening focused libraries of anti-malarial compounds. *PLOS ONE*, *10*, e0123598.

Ouattara, A., & Laurens, M. B. (2015). Vaccines against malaria. *Clin. Infect. Dis.*, *60*, 930-936.

Owen, M. R., Doran, E., & Halestrap, A. P. (2000). Evidence that metformin exerts its anti-diabetic effects through inhibition of complex 1 of the mitochondrial respiratory chain. *J. Biochem.*, *348*, 607-614.

Palmer, E., & Freeman, T. (2004). Investigation into the use of C- and N-terminal GFP fusion proteins for subcellular localization studies using reverse transfection microarrays. *Comp. Funct. Genomics*, *5*, 342-353.

Peng, X., Wang, N., Zhu, A., Xu, H., Li, J., Zhou, Y., Wang, C., Xiao, Q., Guo, L., Liu, F., Jia, Z.-j., Duan, H., Hu, J., Yuan, W., Geng, J., Yan, C., Jiang, X., & Deng, D. (2021). Structural characterization of the *Plasmodium falciparum* lactate transporter PfFNT alone and in complex with antimalarial compound MMV007839 reveals its inhibition mechanism. *PLoS Biol.*, *19*, e3001386.

Pennisi, E. (2015). Science and society. Gene drive turns mosquitoes into malaria fighters. *Science*, *350*, 1014.

Phillips, M. A., Burrows, J. N., Manyando, C., van Huijsduijnen, R. H., Van Voorhis, W. C., & Wells, T. N. C. (2017). Malaria. *Nat. Rev. Dis. Primers*, *3*, 17050.

Pina, A. S., Lowe, C. R., & Roque, A. C. (2014). Challenges and opportunities in the purification of recombinant tagged proteins. *Biotechnol. Adv.*, *32*, 366-381.

Piore, A. (2022). A milestone in the fight against the malaria: the WHO's decision to approve the first malaria vaccine will change the way we fight the deadly disease-and possibly many other killer parasites. *MIT technol. rev.*, *125*, 54.

Plebanski, M., & Hill, A. V. (2000). The immunology of malaria infection. *Curr. Opin. Immunol.*, *12*, 437-441.

Polański, R., Hodgkinson, C. L., Fusi, A., Nonaka, D., Priest, L., Kelly, P., Trapani, F., Bishop, P. W., White, A., Critchlow, S. E., Smith, P. D., Blackhall, F., Dive, C., & Morrow, C. J. (2014). Activity of the monocarboxylate transporter 1 inhibitor AZD3965 in small cell lung cancer. *Clin. Cancer Res.*, *20*, 926-937.

Pollak, M. N. (2012). Investigating metformin for cancer prevention and treatment: the end of the beginning. *Cancer Discov.*, *2*, 778-790.

Pollard, T. D. (2010). A guide to simple and informative binding assays. *Mol. Biol. Cell.*, *21*, 4061-4067.

Poole, R. C., & Halestrap, A. P. (1994). N-terminal protein sequence analysis of the rabbit erythrocyte lactate transporter suggests identity with the cloned monocarboxylate transport protein MCT1. *Biochem. J.*, *303*, 755-759.

Potter, M., Newport, E., & Morten, K. J. (2016). The Warburg effect: 80 years on. *Biochem. Soc. Trans.*, *44*, 1499-1505.

Price, R. N., Tjitra, E., Guerra, C. A., Yeung, S., White, N. J., & Anstey, N. M. (2007). *Vivax* malaria: neglected and not benign. *Am. J. Trop. Med. Hyg.*, *77*, 79-87.

Pygall, S. R., Whetstone, J., Timmins, P., & Melia, C. D. (2007). Pharmaceutical applications of confocal laser scanning microscopy: the physical characterisation of pharmaceutical systems. *Adv. Drug Deliv. Rev.*, *59*, 1434-1452.

Qian, Z., Dougherty, P. G., & Pei, D. (2017). Targeting intracellular protein-protein interactions with cell-permeable cyclic peptides. *Curr. Opin. Chem. Biol.*, *38*, 80-86.

Rahimi, B. A., Thakkinstian, A., White, N. J., Sirivichayakul, C., Dondorp, A. M., & Chokejindachai, W. (2014). Severe *vivax* malaria: a systematic review and meta-analysis of clinical studies since 1900. *Malar. J.*, *13*, 481.

Rambow, J. (2015). Characterization of PfFNT – a lactate transporter in *Plasmodium falciparum*. *Dissertation*. Kiel University. Online available at: https://macau.uni-kiel.de/receive/diss_mods_00016527

Rarbach, M., Kettling, U., Koltermann, A., & Eigen, M. (2001). Dual-color fluorescence cross-correlation spectroscopy for monitoring the kinetics of enzyme-catalyzed reactions. *Methods*, *24*, 104-116.

Rath, A., Glibowicka, M., Nadeau, V. G., Chen, G., & Deber, C. M. (2009). Detergent binding explains anomalous SDS-PAGE migration of membrane proteins. *PNAS*, *106*, 1760-1765.

Rena, G., Hardie, D. G., & Pearson, E. R. (2017). The mechanisms of action of metformin. *Diabetologia*, *60*, 1577-1585.

Ries, J., Petrášek, Z., García-Sáez, A. J., & Schwille, P. (2010). A comprehensive framework for fluorescence cross-correlation spectroscopy. *New J. Phys.*, *12*, 113009.

Ries, J., & Schwille, P. (2012). Fluorescence correlation spectroscopy. *BioEssays*, *34*, 361-368.

Rigler, R., Mets, Ü., Widengren, J., & Kask, P. (1993). Fluorescence correlation spectroscopy with high count rate and low background: analysis of translational diffusion. *Eur. Biophys. J.*, *22*, 169-175.

Rosenthal, P. J. (2005). Proteases and hemoglobin degradation. *Mol. Appr. Malar.*, *1*, 311-326.

Ross, R. (1898). The role of the mosquito in the evolution of the malarial parasite. *Lancet*, *152*, 488-490.

Rottmann, M., McNamara, C., Yeung, B. K., Lee, M. C., Zou, B., Russell, B., Seitz, P., Plouffe, D. M., Dharia, N. V., Tan, J., Cohen, S. B., Spencer, K. R., González-Páez, G. E., Lakshminarayana, S. B., Goh, A., Suwanarusk, R., Jegla, T., Schmitt, E. K., Beck, H. P., . . . Diagana, T. T. (2010). Spiroindolones, a potent compound class for the treatment of malaria. *Science*, *329*, 1175-1180.

Ruan, L., Su, D., Shao, C., Wang, J., Dong, C., Huang, X., & Ren, J. (2015). A sensitive and microscale method for drug screening combining affinity probes and single molecule fluorescence correlation spectroscopy. *Analyst*, *140*, 1207-1214.

Sachs, J., & Malaney, P. (2002). The economic and social burden of malaria. *Nature*, *415*, 680-685.

Saraei, P., Asadi, I., Kakar, M. A., & Moradi-Kor, N. (2019). The beneficial effects of metformin on cancer prevention and therapy: a comprehensive review of recent advances. *Cancer Manag. Res.*, *11*, 3295-3313.

Literature

Schlitzer, M. (2007). Malaria chemotherapeutics part I: history of antimalarial drug development, currently used therapeutics, and drugs in clinical development. *ChemMedChem*, *2*, 944-986.

Schmidt, J. D. R., & Beitz, E. (2022). Mutational widening of constrictions in a formate-nitrite/H⁺ transporter enables aquaporin-like water permeability and proton conductance. *J. Biol. Chem.*, *298*, 101513.

Schroeder, M. (2016). A comparison of *Anopheles* (left) and the *Aedes aegypti* (right) mosquitoes. *Photograph*. Mauritius Images. Retrieved August 25, 2022, from https: // www.mauritius-images.com /en /asset /ME - PI - 8807755_mauritius_ images_bildnummer_09276671_a-comparison-of-anopheles- % 2528 left %2529- and-the-aedes-aegypti-%-2528right%2529-mosquitoes-the-anopheles-mosquito -transmits - malaria - it - bites - in - a - tail-up - position - the - aedes - aegypti- transmits - dengue - fever - yellow - fever - zika - and - other - diseases - it - bites - in-a-tail-down-position.

Schwille, P. (2001). Fluorescence correlation spectroscopy and its potential for intracellular applications. *Cell Biochem. Biophys.* , *34*, 383-408.

Schwille, P., Haupts, U., Maiti, S., & Webb, W. W. (1999). Molecular dynamics in living cells observed by fluorescence correlation spectroscopy with one- and two-photon excitation. *Biophys. J.*, *77*, 2251-2265.

Schwille, P., & Haustein, E. (2001). Fluorescence correlation spectroscopy - an introduction to its concepts and applications. *Spectroscopy*, *94*, 22.

Schwille, P., Meyer-Almes, F. J., & Rigler, R. (1997). Dual-color fluorescence cross-correlation spectroscopy for multicomponent diffusional analysis in solution. *Biophys. J.*, *72*, 1878-1886.

Scriven, E., & Murugan, R. (2005). Pyridine and pyridine derivatives. *Wiley*, *20*, 1-33.

Seelig, A. (2007). The role of size and charge for blood-brain barrier permeation of drugs and fatty acids. *J. Mol. Neurosci.*, *33*, 32-41.

Sharma, A., & Khanduri, U. (2009). How benign is benign tertian malaria? *J. Vector Borne Dis.*, *46*, 141-144.

Shortt, H. E., & Garnham, P. C. C. (1948). Pre-erythrocytic stage in mammalian malaria parasites. *Nature*, *161*, 126-126.

Siddiqui, F. A., Boonhok, R., Cabrera, M., Mbenda, H. G. N., Wang, M., Min, H., Liang, X., Qin, J., Zhu, X., Miao, J., Cao, Y., & Cui, L. (2020). Role of *Plasmodium falciparum* Kelch 13 protein mutations in *P. falciparum* populations from northeastern myanmar in mediating artemisinin resistance. *mBio*, *11*, 1119-1134.

Sidhu, A. B., Verdier-Pinard, D., & Fidock, D. A. (2002). Chloroquine resistance in *Plasmodium falciparum* malaria parasites conferred by pfcrt mutations. *Science*, *298*, 210-213.

Singh, B., & Daneshvar, C. (2013). Human infections and detection of *Plasmodium knowlesi*. *Clin. Microbiol. Rev.*, *26*, 165-184.

Sinka, M. E., Bangs, M. J., Manguin, S., Chareonviriyaphap, T., Patil, A. P., Temperley, W. H., Gething, P. W., Elyazar, I. R. F., Kabaria, C. W., Harbach, R. E., & Hay, S. I. (2011). The dominant *Anopheles* vectors of human malaria in the Asia-Pacific region: occurrence data, distribution maps and bionomic précis. *Parasit. Vectors*, *4*, 89.

Skinner, T. S., Manning, L. S., Johnston, W. A., & Davis, T. M. (1996). *In vitro* stage-specific sensitivity of *Plasmodium falciparum* to quinine and artemisinin drugs. *Int. J. Parasitol.*, *26*, 519-525.

Slater, A. F. (1993). Chloroquine: mechanism of drug action and resistance in *Plasmodium falciparum*. *Pharmacol. Ther.*, *57*, 203-235.

Smit, F. J. (2014). Synthesis and *in vitro* antimalarial activity of novel chalcone derivatives. *Dissertation*. North-West University. Online available at: http://hdl.handle.net/10394/12262.

Smith, J. D., Rowe, J. A., Higgins, M. K., & Lavstsen, T. (2013). Malaria's deadly grip: cytoadhesion of *Plasmodium falciparum*-infected erythrocytes. *Cell Microbiol.*, *15*, 1976-1983.

Snow, R. W., Guerra, C. A., Noor, A. M., Myint, H. Y., & Hay, S. I. (2005). The global distribution of clinical episodes of *Plasmodium falciparum* malaria. *Nature*, *434*, 214-217.

Somaiah, C., Kumar, A., Mawrie, D., Sharma, A., Patil, S. D., Bhattacharyya, J., Swaminathan, R., & Jaganathan, B. G. (2015). Collagen promotes higher adhesion, survival and proliferation of mesenchymal stem cells. *PLOS ONE*, *10*, e0145068.

Southwick, P. L., Ernst, L. A., Tauriello, E. W., Parker, S. R., Mujumdar, R. B., Mujumdar, S. R., Clever, H. A., & Waggoner, A. S. (1990). Cyanine dye labeling reagents - carboxymethylindocyanine succinimidyl esters. *Cytometry*, *11*, 418-430.

Spangenberg, T., Burrows, J. N., Kowalczyk, P., McDonald, S., Wells, T. N. C., & Willis, P. (2013). The open access malaria box: a drug discovery catalyst for neglected diseases. *PLOS ONE*, *8*, e62906.

Spielmann, T., Montagna, G. N., Hecht, L., & Matuschewski, K. (2012). Molecular make-up of the *Plasmodium* parasitophorous vacuolar membrane. *Int. J. Med. Microbiol.*, *302*, 179-186.

Straimer, J., Gnädig, N. F., Witkowski, B., Amaratunga, C., Duru, V., Ramadani, A. P., Dacheux, M., Khim, N., Zhang, L., Lam, S., Gregory, P. D., Urnov, F. D., Mercereau-Puijalon, O., Benoit-Vical, F., Fairhurst, R. M., Ménard, D., & Fidock, D. A. (2015). Drug resistance. K13-propeller mutations confer artemisinin resistance in *Plasmodium falciparum* clinical isolates. *Science*, *347*, 428-431.

Sutherland, C. (2007). A challenge for the development of malaria vaccines: polymorphic target antigens. *PLoS Med.*, *4*, e116.

Thomas, P., & Smart, T. G. (2005). HEK293 cell line: a vehicle for the expression of recombinant proteins. *J. Pharmacol. Toxicol. Methods*, *51*, 187-200.

Thompson, N. L., Lieto, A. M., & Allen, N. W. (2002). Recent advances in fluorescence correlation spectroscopy. *Curr. Opin. Struct. Biol.*, *12*, 634-641.

Tilley, L., Straimer, J., Gnädig, N. F., Ralph, S. A., & Fidock, D. A. (2016). Artemisinin action and resistance in *Plasmodium falciparum. Trends Parasitol.*, *32*, 682-696.

Tiwari, M., Mikuni, S., Muto, H., & Kinjo, M. (2013). Determination of dissociation constant of the NFκB p50/p65 heterodimer using fluorescence cross-correlation spectroscopy in the living cell. *Biochem. Biophys. Res. Commun.*, *436*, 430-435.

Todenhöfer, T., Seiler, R., Stewart, C., Moskalev, I., Gao, J., Ladhar, S., Kamyabi, A., al Nakouzi, N., Hayashi, T., Choi, S., Wang, Y., Frees, S., Daugaard, M., Oo, H., Fisel, P., Schwab, M., Schaeffeler, E., Douglas, J., Hennenlotter, J., & Black, P. (2018). Selective inhibition of the lactate transporter MCT4 reduces growth of invasive bladder cancer. *Mol. Cancer Ther.*, *17*, 2018.

Trape, J. F. (2001). The public health impact of chloroquine resistance in Africa. *Am. J. Trop. Med. Hyg.*, *64*, 12-17.

Tse, E. G., Korsik, M., & Todd, M. H. (2019). The past, present and future of anti-malarial medicines. *Malar. J.*, *18*, 93.

Tu, Y. (2011). The discovery of artemisinin (qinghaosu) and gifts from Chinese medicine. *Nat. Med.*, *17*, 1217-1220.

Turusov, V., Rakitsky, V., & Tomatis, L. (2002). Dichlorodiphenyltrichloroethane (DDT): ubiquity, persistence, and risks. *Environ. Health Perspect.*, *110*, 125-128.

Ullrich, A. K. (2016). Characterisation of trafficking signals shared by different types of exported proteins in the human malaria parasite *Plasmodium falciparum*. *Dissertation*. University of Hamburg. Online available at: https://ediss.sub.uni-hamburg.de/handle/ediss/6796.

Vaid, A., Ranjan, R., Smythe, W. A., Hoppe, H. C., & Sharma, P. (2010). PfPI3K, a phosphatidylinositol-3 kinase from *Plasmodium falciparum*, is exported to the host erythrocyte and is involved in hemoglobin trafficking. *Blood*, *115*, 2500-2507.

Vauquelin, G. (2016). Effects of target binding kinetics on *in vivo* drug efficacy: k_{off}, k_{on} and rebinding. *Br. J. Pharmacol.*, *173*, 2319-2334.

Vieira Gomes, A. M., Souza Carmo, T., Silva Carvalho, L., Mendonça Bahia, F., & Parachin, N. S. (2018). Comparison of yeasts as hosts for recombinant protein production. *Microorganisms*, *6*, 38.

Vogel, H. G., Vogel, W. H., Schölkens, B. A., Sandow, J., Müller, G., & Vogel, W. F. (2002). Introduction strategies in drug discovery and evaluation. *Springer*, *1*, 1-20.

Volkov, V. (2015). Quantitative description of ion transport via plasma membrane of yeast and small cells. *Front. Plant Sci.*, *6*, 425.

Waight, A. B., Love, J., & Wang, D. N. (2010). Structure and mechanism of a pentameric formate channel. *Nat. Struct. Mol. Biol.*, *17*, 31-37.

Walloch, P., Hansen, C., Priegann, T., Schade, D., & Beitz, E. (2021). Pentafluoro-3-hydroxy-pent-2-en-1-ones potently inhibit FNT-type lactate transporters from all five human-pathogenic *Plasmodium* species. *ChemMedChem*, *16*, 1283-1289.

Walloch, P., Henke, B., Häuer, S., Bergmann, B., Spielmann, T., & Beitz, E. (2020). Introduction of scaffold nitrogen atoms renders inhibitors of the malarial L-lactate

transporter, PfFNT, effective against the Gly107Ser resistance mutation. *J. Med. Chem.*, *63*, 9731-9741.

Wang, H., Lin, Y., Nienhaus, K., & Nienhaus, G. U. (2018). The protein corona on nanoparticles as viewed from a nanoparticle-sizing perspective. *Wiley Interdiscip. Rev. Nanomed. Nanobiotechnol.*, *10*, e1500.

Wang, J., Zhang, C.-J., Chia, W. N., Loh, C. C. Y., Li, Z., Lee, Y. M., He, Y., Yuan, L.-X., Lim, T. K., Liu, M., Liew, C. X., Lee, Y. Q., Zhang, J., Lu, N., Lim, C. T., Hua, Z.-C., Liu, B., Shen, H.-M., Tan, K. S. W., & Lin, Q. (2015). Haem-activated promiscuous targeting of artemisinin in *Plasmodium falciparum. Nat. Commun.*, *6*, 10111.

Wang, Y., Huang, Y., Wang, J., Cheng, C., Huang, W., Lu, P., Xu, Y. N., Wang, P., Yan, N., & Shi, Y. (2009). Structure of the formate transporter FocA reveals a pentameric aquaporin-like channel. *Nature*, *462*, 467-472.

Waring, M. J. (2009). Defining optimum lipophilicity and molecular weight ranges for drug candidates-molecular weight dependent lower logD limits based on permeability. *Bioorg. Med. Chem. Lett.*, *19*, 2844-2851.

Warrell, D. A., & Gilles, H. M. (2002). Essential Malariology *CRC Press*, *4*, 1-352.

Weidemann, T., Wachsmuth, M., Tewes, M., Rippe, K., & Langowski, J. (2002). Analysis of ligand binding by two-colour fluorescence cross-correlation spectroscopy. *Single Mol.*, *3*, 49-61.

Weisshart, K., Jüngel, V., & Briddon, S. J. (2004). The LSM 510 META - ConfoCor 2 system: an integrated imaging and spectroscopic platform for single-molecule detection. *Curr. Pharm. Biotechnol.*, *5*, 135-154.

Wellems, T. E., & Plowe, C. V. (2001). Chloroquine-resistant malaria. *J. Infect. Dis.*, *184*, 770-776.

Wells, T. N., Hooft van Huijsduijnen, R., & Van Voorhis, W. C. (2015). Malaria medicines: a glass half full? *Nat. Rev. Drug Discov.*, *14*, 424-442.

Wesolowski, A., Eagle, N., Tatem, A. J., Smith, D. L., Noor, A. M., Snow, R. W., & Buckee, C. O. (2012). Quantifying the impact of human mobility on malaria. *Science*, *338*, 267-270.

White, N. J. (2004). Antimalarial drug resistance. *J. Clin. Invest.*, *113*, 1084-1092.

White, N. J. (2008). Qinghaosu (artemisinin): the price of success. *Science*, *320*, 330-334.

WHO. (2021). World malaria report 2021. World Health Organization. Retrieved September 15, 2022, from https://www.who.int/teams/global-malaria-programme/reports/world-malaria-report-2021.

Wiechert, M., & Beitz, E. (2017a). Formate-nitrite transporters: monoacids ride the dielectric slide. *Channels*, *11*, 365-367.

Wiechert, M., & Beitz, E. (2017b). Mechanism of formate-nitrite transporters by dielectric shift of substrate acidity. *EMBO J.*, *36*, 949-958.

Wilcke, L. (2018). Identification and characterization of invasion-related proteins of the malaria parasite *Plasmodium falciparum*. *Dissertation*. University of Hamburg. Online available at: https://ediss.sub.uni-hamburg.de/handle/ediss/7756.

Wong, C. C., Cheng, K. W., & Rigas, B. (2012). Preclinical predictors of anticancer drug efficacy: critical assessment with emphasis on whether nanomolar potency should be required of candidate agents. *J. Pharmacol. Exp. Ther.*, *341*, 572-578.

Woodrow, C. J., Penny, J. I., & Krishna, S. (1999). Intraerythrocytic *Plasmodium falciparum* expresses a high affinity facilitative hexose transporter. *J. Biol. Chem.*, *274*, 7272-7277.

Wu, B., Rambow, J., Bock, S., Holm-Bertelsen, J., Wiechert, M., Soares, A. B., Spielmann, T., & Beitz, E. (2015). Identity of a *Plasmodium* lactate/H^+ symporter structurally unrelated to human transporters. *Nat. Commun.*, *6*, 6284.

Wykes, M. N. (2013). Why haven't we made an efficacious vaccine for malaria? *EMBO Rep.*, *14*, 661.

Yang, N., & Hinner, M. (2015). Getting across the cell membrane: an overview for small molecules, peptides, and proteins. *Methods mol. biol.*, *1266*, 29-53.

Yayon, A., Cabantchik, Z. I., & Ginsburg, H. (1984). Identification of the acidic compartment of *Plasmodium falciparum*-infected human erythrocytes as the target of the antimalarial drug chloroquine. *EMBO J.*, *3*, 2695-2700.

Yu, L., Lei, Y., Ma, Y., Liu, M., Zheng, J., Dan, D., & Gao, P. (2021). A comprehensive review of fluorescence correlation spectroscopy. *Front. Phys.*, *9*, 6444.

Acknowledgements

First and foremost, I would like to thank my academic supervisor, Prof. Dr. Eric Beitz, for giving me the opportunity to work on this exciting project and for providing unwavering assistance throughout my PhD journey.

I would also like to extend my special thanks to my industrial supervisors, Dr. Stefan Hannus and Dr. Frank Becker (Intana Bioscience, München), for their continuous encouragement, valuable feedback, and guidance. Their insights have been crucial in helping me to overcome the challenges of my research project and to achieve my research goals.

Furthermore, I would like to thank my colleagues, Dr. Stefano Minguzzi, Kerrin Hansen, Maria Koch, and Dr. Martina Grandl, for their camaraderie and for sharing their expertise with me, which has been of immense help in my research work.

Additionally, I am grateful to Dr. Michael Hannus, Dr. Michaela Beitzinger, Jonas Bertram, and Lisa Marinkovic for their assistance with various experiments and analyses.

Moreover, I would also like to give special thanks to Nathan Epalle for many helpful discussions.

I gratefully acknowledge the members of the PROTON Consortium and the financial support received from the European Union's Horizon 2020 research and innovation program under the Marie Skłodowska-Curie grant agreement No. 860592.

Last but not least, I would like to express my deep and sincere gratitude to my parents, Beata and Waldemar, and to my boyfriend, Jonas, for their unfailing support while I was working on this thesis.

Eidesstattliche Erklärung

Diese Arbeit ist unter Einhaltung der Regeln der guten wissenschaftlichen Praxis der Deutschen Forschungsgemeinschaft entstanden. Ich versichere, dass ich die vorliegende Dissertation selbstständig und, abgesehen von der Beratung durch den Betreuer, nur mit den hier angegebenen Quellen und Hilfsmitteln verfasst habe. Ich versichere auch, dass mir noch kein akademischer Grad entzogen wurde. Diese Arbeit wurde noch in keinem anderen Prüfungsverfahren vorgelegt. Teile dieser Arbeit wurden bereits veröffentlicht in:

Jakobowska, I., Becker, F., Minguzzi, S., Hansen, K., Henke, B., Epalle, N. H., Beitz, E., & Hannus, S. (2021). Fluorescence Cross-Correlation Spectroscopy Yields True Affinity and Binding Kinetics of *Plasmodium* Lactate Transport Inhibitors. *Pharmaceuticals (Basel, Switzerland)*, *14*(8), 757. https://doi.org/10.3390/ph14080757

Iga Jakóbowska

Kiel, April 2023